DEVELOPMENT OF A MULTIMODAL FRAMEWORK FOR CARDIAC COMPUTED TOMOGRAPHY GATING

A Dissertation
Presented to
The Academic Faculty

By

Jingting Yao

In Partial Fulfillment
of the Requirements for the Degree
Doctor of Philosophy in the
School of Electrical and Computer Engineering

Georgia Institute of Technology

December 2018

DEVELOPMENT OF A MULTIMODAL FRAMEWORK FOR CARDIAC COMPUTED TOMOGRAPHY GATING

Approved by:

Dr. Pamela T. Bhatti, Advisor
School of Electrical and Computer Engineering
Georgia Institute of Technology

Dr. Srini Tridandapani, Co-Advisor
School of Electrical and Computer Engineering
Georgia Institute of Technology

Dr. James H. McClellan
School of Electrical and Computer Engineering
Georgia Institute of Technology

Dr. Xiangyang Tang
Department of Radiology and Imaging Sciences, School of Medicine
Emory University

Dr. David V. Anderson
School of Electrical and Computer Engineering
Georgia Institute of Technology

Dr. William F. Auffermann
Department of Radiology, School of Medicine
University of Utah

Date Approved: August 27, 2018

Dedicated to all those who helped make my life brilliant.

ACKNOWLEDGEMENTS

This work could not have been conducted at this level without the combined efforts of Dr. Pamela Bhatti, Dr. Srini Tridandapani and Dr. Carson Wick. I am most indebted to Dr. Pamela Bhatti, my research advisor, who provided me with this great research opportunity; and who continues to support my career goals. Special thanks as well to Dr. Srini Tridandapani, for his professional guidance and generous encouragement along the way. Dr. Carson Wick has been my teacher and mentor both in research and life. He provided extensive professional and personal guidance; and taught me much about both scientific research and life in general. In addition, I owe a debt of gratitude to Dr. Mary Ann Weitnauer for her early encouragement and her kind reference to Dr. Bhatti when I was looking for a research opportunity three years ago. I would also like to appreciate each of the radiologic technologists at the Winship Cancer Institute with whom I have had the pleasure to work.

Since I started working on my proposal, my reading committee has been very supportive and helpful. I am grateful for the guidance from Dr. McClellan, my reading committee chair, who has been very patient and professional in helping me with research problems. Another reading committee member of mine, Dr. Tang, has been very encouraging to me. Whenever I met Dr. Tang, he asked me about my research progress and showed his interest that greatly inspired me. The other two final defense committee members, Dr. Auffermann and Dr. Anderson are very kind to me, too. I have had the opportunity to co-author with Dr. Auffermann on one of the publications, to which Dr. Auffermann contributed valuable ideas and essential efforts. When I requested Dr. Anderson to serve on my final defense committee, he showed his enthusiasm about my research and gladly approved immediately.

There have been many friends who have walked alongside me during this journey. They are my strong support, and I am so honored to have developed life-long relationships with them. In my heart is the memory of the care and help from all my dear friends, without whom it would not have been such a brilliant journey for me. The list of them is long, but

I am sincerely grateful to every one of them.

Last but not least, no one has been more important to me in the pursuit of this research than the members of my family, especially my mother and father. It is their unconditional love and support that brings me to where I am today. Therefore, my deepest gratitude goes to my dearest parents.

Graduate school has been such a unique and absolutely brilliant journey of my life that I am thankful to everything and everyone, including myself.

TABLE OF CONTENTS

LIST OF TABLES

LIST OF FIGURES

SUMMARY

Cardiovascular disease (CVD), also known as heart disease, is the leading cause of death globally. About eight million Americans are now suffering from CVD with 2,400 dying each day [1]. The gold standard for evaluating CVD, catheter coronary angiography, is invasive and expensive [2]. An alternative technique, computed tomography angiography (CTA), is less invasive, relatively inexpensive and faster [3, 4]. However, this emerging diagnostic tool suffers from limited temporal resolution resulting in cardiac motion artifacts. To minimize the effect of cardiac motion, cardiac CTA data acquisition requires triggering when cardiac motion is minimal within the cardiac cycle, known as the cardiac quiescence.

The overarching goal of this work is to improve the diagnostic quality and reduce the radiation dose of cardiac CTA imaging by developing novel gating strategies that optimize prospective gating. Prospective gating is a scan acquisition type of cardiac CTA that results in less radiation dose[1] but requires triggering during the cardiac quiescence. Since the inception of cardiac CTA, quiescence prediction has relied almost exclusively on the real-time electrocardiography (ECG) signal [6, 7]. However, while providing important information as to the electrical activity of cardiac motion, ECG-triggered gating fails to inherently capture the mechanical movement of the heart and thus is suboptimal. Seismocardiography (SCG) is a non-invasive strategy that measures the acceleration of chest wall caused by cardiac motion. Therefore, SCG can be a potential supplement to ECG for cardiac quiescence detection and prediction [8].

This work presents a multimodal gating framework that fuses quiescence predictions derived from ECG and SCG. Cardiac quiescence derived from the B-mode echocardiography signal was used as the baseline for comparing the performance of SCG and ECG. Using a heart-sound-based waveform matching approach, the SCG-based quiescence pre-

[1] A high level of radiation exposure of 12 mSv using retrospective gating can possibly be reduced to only about 4 mSv by prospective gating. Note that a 10 mSv CTA exam may relate to an increasing possibility of fatal cancer of approximately 1 in 2,000 cases [5].

diction demonstrated improved accuracy for cardiac gating. To fuse ECG and SCG predictions, an artificial neural network (ANN) was employed with cardiac features selected from the ECG and SCG on a beat-by-beat basis. The fusion-based prediction yielded more accurate and robust quiescence prediction compared with the traditional ECG-only-based prediction. The diagnostic quality of reconstructed CTA images at predicted timings was interpreted by a radiologist and the assessment indicated improvement with the inclusion of SCG signals. Furthermore, a proof-of-concept prototype that implements the multimodal framework in a near real-time manner via integration of existing hardware and software was developed. Testing of this prototype using both the pre-recorded and real-time data demonstrated the feasibility of the real-time multimodal framework.

It is expected that the next generation of cardiac imaging machines, including CTA and magnetic resonance imaging (MRI), can be triggered more accurately in real-time by using a multimodal framework rather than ECG alone.

CHAPTER 1
INTRODUCTION

Cardiovascular disease (CVD), also known as heart disease, refers to conditions involving narrowed or blocked blood vessels that can result in a heart attack [9]. According to the World Health Organization, CVD is the leading cause of death globally. In 2015, approximately 17.7 million people died from CVD, comprising 31% of global death [10].

Currently, catheter coronary angiography (CCA) is the gold standard for assessing coronary blood vessels to evaluate and manage CVD [11]. However, CCA is invasive in that it requires an insertion of a catheter from the upper thigh which is then threaded through the aorta into the heart. The intraarterial injection of contrast agent enables visualization of the arterial blockage via x-ray imaging. An illustration of CCA is shown in Figure 1.1 (A). CCA may lead to non-negligible complications such as bleeding, stroke and heart attack [12], and is relatively expensive [13] with a mean hospital charge of $\$37,000$. Furthermore, while CCA visualizes the coronary arterial lumen, CCA does not directly provide information about vessel wall abnormalities [11].

As an alternative, computed tomography angiography (CTA) [14] is a less invasive, less expensive and faster technology than CCA [3, 4]. CTA utilizes x-rays in combination with computerized analysis for imaging. CTA sends beams of x-rays from several different angles of a rotating device through the area of interest in the patient's body. The obtained slices of projection images are then assembled by a computer to reconstruct into a three-dimensional volume for diagnoses. An illustration of CTA is shown in Figure 1.1 (B).

The value of cardiac CTA is in ruling out people at low to intermediate risk of CVD. It has been shown in many studies that cardiac CTA has very high negative predictive value[1]

[1]Negative predictive value is the probability that subjects with a negative screening test truly do not have the disease. Positive predictive value is the probability that subjects with a positive screening test truly have the disease.

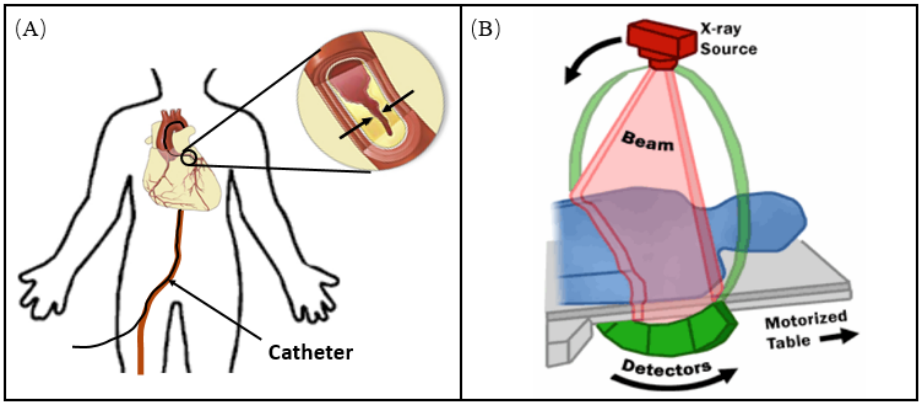

Figure 1.1: Comparison between CCA and CTA. (A) CCA is invasive in that it requires an insertion of a catheter from the upper thigh which then threads through the aorta into the heart. The intraarterial injection of contrast agent enables visualization of the arterial blockage via x-ray imaging. (B) CTA utilizes x-rays in combination with computerized analysis for imaging. Beams of x-rays are sent from several different angles of a rotating device through the area of interest in the patient's body. CTA is a less invasive technique compared with CCA. Figure (B) reproduced from [15].

up from 93% to 100% [16]. On the other hand, the low diagnostic yield (low positive predictive value) of CCA raises the concern of undergoing unnecessary invasive tests for people at low to intermediate risk of CVD. Approximately 40% of the CCA examinations reveal no coronary artery disease [17]. It is important to mention that cardiac CTA and CCA can possibly achieve the same level of diagnostic quality. Therefore, cardiac CTA may be a more suitable diagnostic technique for the low-risk group of individuals.

Yet, cardiac CTA is limited by temporal resolution. In the context of cardiac imaging, high temporal resolution is achieved when imaging is conducted fast enough to "suspend" the motion of the heart. Otherwise, the reconstructed images could be blurred or mis-aligned due to cardiac motion. Cardiac motion artifact is one of the important factors that compromises image quality which directly affects diagnoses. Therefore, to improve the diagnostic quality of cardiac CTA, it is crucial to obtain cardiac CTA images during a time interval when the heart is in the state of minimal motion, or within the *quiescent period* of the cardiac cycle.

A primary factor that affects the diagnostic quality and radiation dose of the cardiac

CTA is the scan acquisition type. The two main scan acquisition types are retrospective gating and prospective triggering[2]. Gating is a general term describing the action of a cardiac CTA machine sending x-rays to start acquiring imaging data. Triggering is a special case of gating which requires a timed triggering signal to activate the action of data acquisition. In retrospective gating, x-rays are sent throughout the whole cardiac cycles for a continuous data acquisition until the heart volume is covered. Afterwards, retrospectively, only part of the selected data that yield high image quality are reconstructed. Alternatively, for prospective triggering, x-rays are triggered to be sent only during quiescent periods. In this case, a limited radiation dose occurs within each cardiac cycle. Prospective triggering is also called the step and shoot scan acquisition method. Currently, cardiac gating of clinical CTA machine relies almost exclusively on the ECG signal. An illustration of the two scan acquisition types are presented in Figure 1.2.

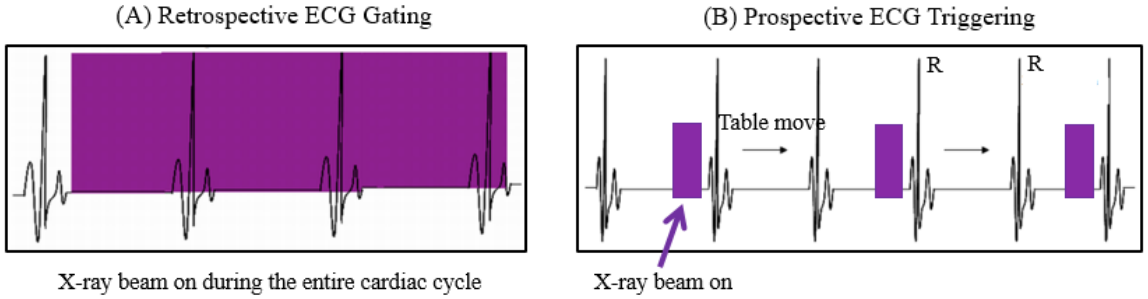

Figure 1.2: (A) Retrospective ECG gating and (B) prospective ECG triggering. Purple area is the period during which the patient's body is exposed to radiation. R denotes the R-peak of ECG signal. Figure reproduced from [18].

With prospective cardiac CTA, the radiation exposure of 12 mSv associated with the 128-slice retrospective cardiac CTA can possibly be reduced to only approximately 4 mSv [5, 19]. Figure 1.3 summarizes the mean effective dose associated with the two scan acquisition types. The radiation dose is especially important for individuals with congenital heart disease as they have to go through many cardiac CTA scans throughout their lives. Therefore, imaging using prospective triggering for cardiac CTA data acquisition is vital

[2]Prospective triggering is a rigorous term. A more general term used interchangeably in some publications is prospective gating.

for the health of individuals.

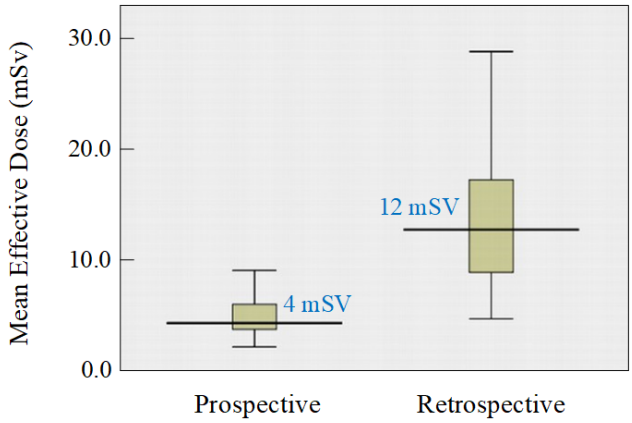

Figure 1.3: Mean effective dose associated with retrospective (12 mSv) gating and prospective triggering (4 mSv). Statistics are based on the Siemens Definition Flash dual-source 128-slice CTA scanner (Siemens, Erlangen, Germany). Horizontal line in each box shows median and top and bottom lines of boxes show interquartile range. Figure reproduced from [18].

1.1 Research Statement

For prospective triggering, the CTA machine is only triggered to acquire data during predicted cardiac quiescence whose occurrence is determined prior to data acquisition. *Cardiac quiescence* is a state of minimal motion relative to the overall motion within a cardiac cycle. The predicted quiescence is often in the form of a time delay from a particular feature (e.g., the most recent R-peak of ECG) in the cardiac signal. Accordingly, accurately predicting cardiac quiescence is crucial for obtaining cardiac CTA data that yield high diagnostic quality. *The focus of this research investigates the cardiac-motion-based signal, seismocardiography (SCG), as a supplemental gating signal, that can potentially provide more robust and accurate quiescence prediction for prospective triggering of CTA data acquisition.*

1.2 Research Contributions

To achieve the goal of optimizing quiescence prediction for prospective triggering, a multimodal gating strategy encompassing a cardiac-motion-based signal was developed. Currently, clinical quiescence prediction relies almost exclusively on the real-time ECG signal. This is not always reliable since ECG is only a proxy of the heart motion and has been demonstrated to be an imprecise marker of the instantaneous cardiac mechanical motion [20, 21]. As an alternative, SCG [22, 23] directly measures the mechanical state of the heart vibration and has the potential in improving quiescence prediction [8, 24, 25].

To date, cardiac CTA is yet to be the mainstream diagnostic tool for examining individuals with suspected CVD due to lack of reliability in achieving enhanced diagnostic quality with low radiation dose in widespread clinical practice. The ultimate goal of this work is to apply a multimodal gating framework to cardiac CTA scanner. To achieve this goal, a proof-of-concept near real-time prototype was developed and tested.

In summary, the major contributions of this work include:

1. Design of a waveform matching quiescence prediction algorithm that utilizes personalized heart sound waveforms of SCG signal. Using quiescence derived from the B-mode echocardiography as the baseline, SCG-based prediction was more accurate as compared to ECG-based prediction on a beat-by-beat basis[3]. This demonstrated the potential of SCG as a supplemental gating signal to ECG to achieve more accurate quiescence predictions.

2. Development of an ECG-SCG-based multimodal framework that fuses predictions from ECG and SCG using an artificial neural network (ANN). Cardiac features extracted from ECG and SCG signals enable the ANN to generate weights corresponding to predictions from ECG and SCG. Combining information from electrical and

[3]Ideally, quiescent periods exist in every cardiac cycle, and within each quiescent period cardiac imaging data can be acquired with the best diagnostic quality. Thus, the quiescence prediction can be made for each cardiac cycle.

mechanical signals compensates for the sub-optimal prediction from ECG as well as for the susceptibility of SCG signal to noise and artifacts. Fusion-based quiescence prediction advanced ECG-only- and SCG-only-based methods because its predictions were more accurate and robust[4].

3. Assessment of the diagnostic quality of the coronary vessels based on CTA images reconstructed at predicted quiescence from ECG-, SCG- and fusion-based methods. The radiological interpretation in visualization of calcification and motion artifacts quantitatively validated the value of incorporating the cardiac-motion-based signal for quiescence prediction.

4. Integration of hardware and software platforms to serve as a proof-of-concept prototype of a near real-time multimodal framework for triggering CTA data acquisition. Testing results demonstrated the feasibility of the real-time fusion-based quiescence prediction framework.

[4]In the case of quiescence prediction for cardiac gating, robustness refers to the ability to resist heart rate variability and heart rate prediction error caused by inter- and intra-personal differences. Quantitatively, it was measured by the variability of quiescence prediction error.

CHAPTER 2

BACKGROUND

To develop gating strategies for triggering cardiac CTA data acquisition, it is necessary to understand the related cardiac sensing modalities. Additionally, it is also important to grasp some basic knowledge of cardiovascular physiology.

2.1 Cardiac Sensing Modalities

This work investigated three sensing modalities, electrocardiography (ECG), seismocardiography (SCG) and B-mode echocardiography. Visualization of these signals, including the B-mode echocardiography, echocardiography deviation, ECG and SCG signals are displayed in Figure 2.1. The echocardiography deviation is a magnitude of velocity derived from the B-mode echocardiography, and in the case of Figure 2.1 is applied to the inter-ventricular septum. The cardiac quiescence detected from the echocardiography deviation signal is used as the baseline while comparing the performance of ECG and SCG.

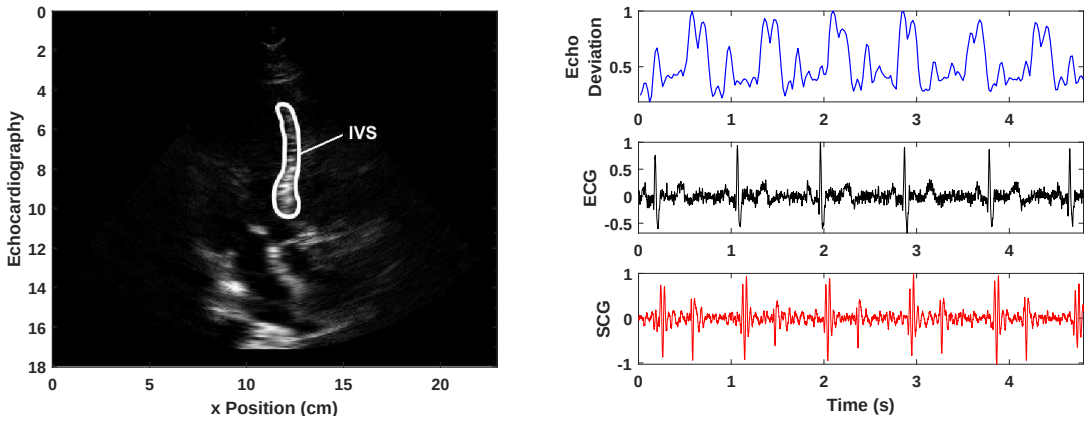

Figure 2.1: Echocardiography: B-mode echocardiography frame from an apical four chamber view of the heart, with contour shown around the inter-ventricular septum (IVS); Echo Deviation: Motion signals derived from B-mode sequences by applying the phase-to-phase deviation measure elaborated in [26]; ECG: Time-series de-noised ECG signal; SCG: Time-series de-noised SCG signal.

2.1.1 Electrocardiography

Pioneered in the early 1900s, ECG is a traditional yet still a predominant technique for diagnosing cardiac-related conditions. ECG records the electrical activity of the heart through electrodes placed on the skin [27]. Identifiable features in an ECG signal are shown in Figure 2.2. In an ECG waveform, a pair of adjacent R-peaks is an indication of one cardiac cycle and thus ECG is usually used to segment cardiac signals.

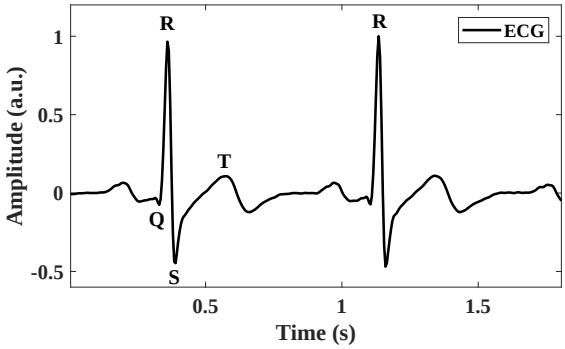

Figure 2.2: Waveform of ECG. ECG nomenclatures: ventricular depolarization (QRS complex) and repolarization (T wave).

Since the inception of prospective cardiac CTA, quiescence prediction has relied almost exclusively on the real-time ECG signal. A pre-defined linear piece-wise function $\mathcal{F}$ predicting the quiescent phase with respect to heart rate is often employed [28, 29]. Given a predicted heart rate (HR) $\hat{r}$, the gating function $\mathcal{F}$ maps $\hat{r}$ to a one-on-one predicted quiescent phase P and

$$P = \mathcal{F}(\hat{r}) \tag{2.1}$$

Cardiac phase (%) is a percentage interval of a cardiac cycle normalized for heart rate variability. Quiescent phase is a cardiac phase that lies within a quiescent period of a cardiac cycle. Figure 2.3 displays five different ECG gating functions [28–32] that are summarized in multiple works on different cardiac CTA scanners. The different versions of gating functions suggests that ECG-based gating lacks standardization, which leaves room for improvement. In addition, such function-based gating approach neglects the intra- and

inter-personal variation in cardiac signals with respect to the cardiac motion and thus is not always reliable. Furthermore, while providing important information as to the electrical activity during the cardiac cycle, ECG gating fails to inherently capture the mechanical motion of the heart.

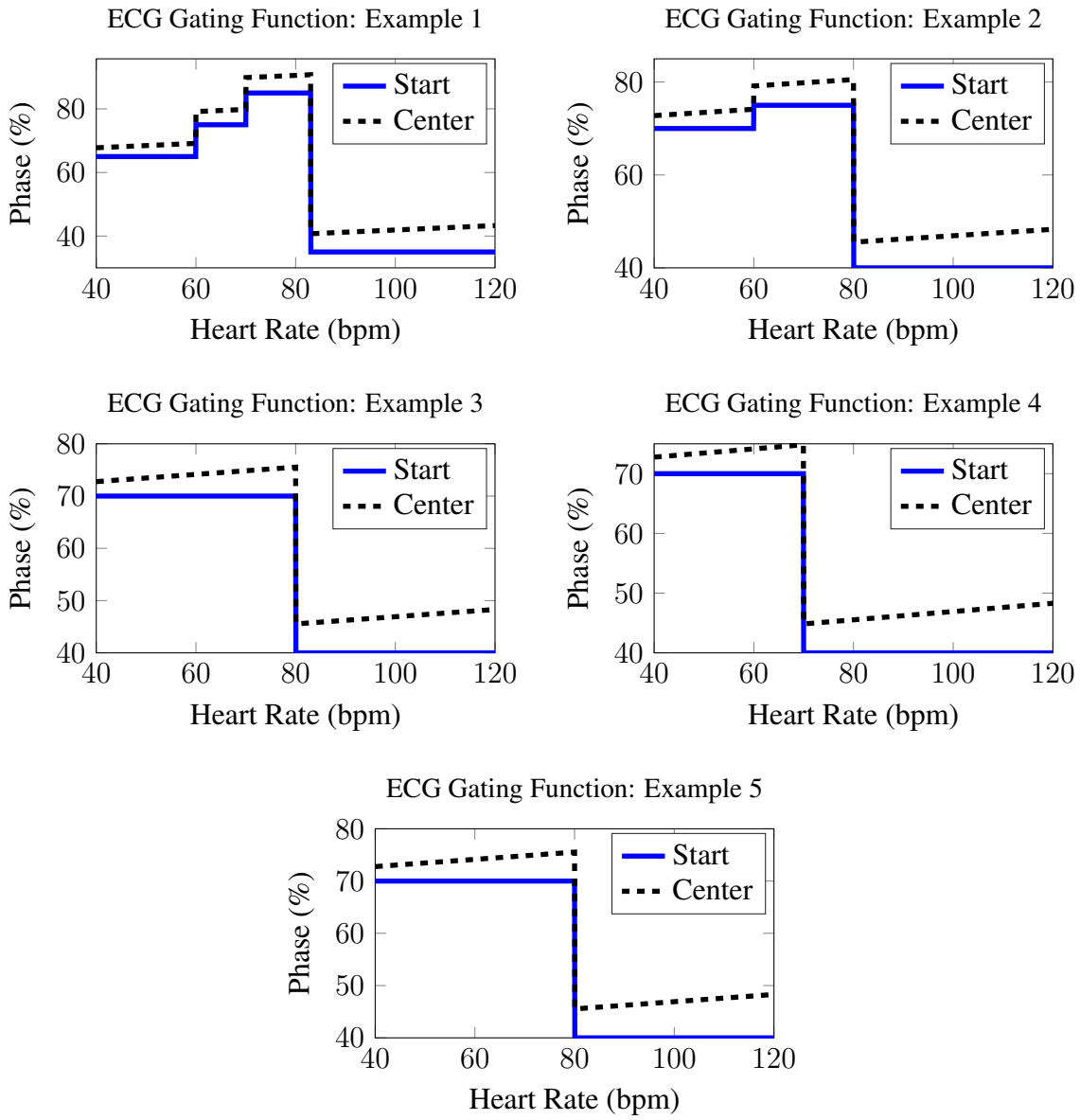

Figure 2.3: ECG gating functions. Examples 1-5 are summarized from [28–32], respectively. Center represents that gating information is the center of the quiescent period, and start represents that gating information is the start of the quiescence period. Depending on the requirement of different CTA scanners, the gating information may vary.

Depending on the CTA scanner, the predicted phase for gating is either the center or start of the data acquisition window. This research used a Siemens SOMATOM Definition dual-source 64-slice CTA scanner (Siemens, Erlangen, Germany). The temporal resolution of this scanner remains at 83 ms at all heart rates. In other words, the length of the reconstruction window is a constant $T_{acq} = 83\,\mathrm{ms}$ [33]. The configuration of this scanner requires a predicted phase to indicate the middle of data acquisition widow. Therefore, in the computerized processing of this work, the phase of minimal motion was identified and designated as the midpoint of the cardiac CTA data acquisition window. The relationship between the center and start phase of the data acquisition window at a predicted HR $\hat{r}$

$$P_{center}(\hat{r}) = P_{start}(\hat{r}) + \frac{T_{acq}}{2}/\frac{60}{\hat{r}} \times 100\%, \tag{2.2}$$

where P_{center} and P_{start} are cardiac phases (%) denoting the center and start of the quiescence, respectively.

2.1.2 Echocardiography

Echocardiography utilizes the transmission and reception of ultrasound to directly evaluate cardiac motion in real-time. Important echocardiographic techniques for assessing cardiac dynamics include M-mode, B-mode, Doppler and speckle tracking. B-mode echocardiography [34] is a two-dimensional presentation that results from modulating the brightness of the spot in the echo-producing interface. The four chambers of the heart can be visualized from the B-mode echocardiography.

In early works, echocardiography was demonstrated to provide accurate gating timing [20, 35] for cardiac CTA. The intersection that separates the left and right ventricular chambers is the inter-ventricular septum (IVS). An echocardiographic visualization of the four-chamber apical view and the IVS are shown in Figure 2.4. The motion of IVS can be recorded in echocardiography and IVS has been shown as a reliable predictor for coronary

vessel quiescence [36]. Therefore, quiescence derived from the B-mode echocardiography is considered as an excellent tool for assessing cardiac conditions in real-time [35] and can be used as a baseline for quiescence.

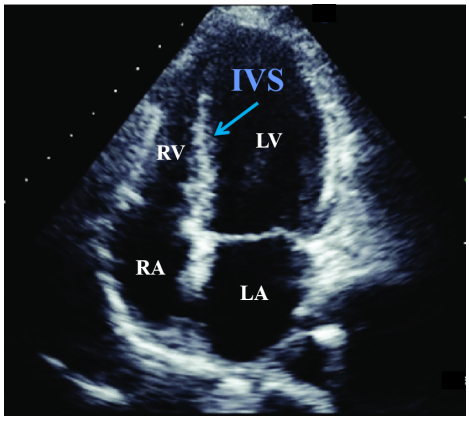

Figure 2.4: Echocardiographic visualization of the four-chamber apical view. RV: right ventricle; LV: left ventricle; RA: right atrium; LA: left atrium; IVS: inter-ventricular septum. Figure reproduced from [37].

Applying a frame-to-frame deviation measure developed by a previous research [26], the magnitude of the IVS velocity was derived from B-mode sequences. This converts the two-dimensional cardiac information from the B-mode echocardiography into a unidimensional signal. Quiescence can be identified from this derived velocity magnitude and modeled as a linear function of heart rate [38]. In this work, quiescence derived using the modeled linear function was considered as the baseline when comparing quiescence derived from ECG and SCG.

Despite the merits of echocardiography in quiescence prediction, it has some disadvantages, including operator-dependence and incompatibility with CTA since clinically available transducers can cause artifacts in the CTA images [8], making it impractical for the real-time CTA data acquisition.

2.1.3 Seismocardiography

Seismocardiography (SCG) is a noninvasive strategy that records the low-frequency vibration due to heart motion by placing an accelerometer on the chest wall [39]. An example

of SCG waveform along with its identifiable features are displayed in Figure 2.5. Different from ECG, SCG signal provides information about the mechanical movement of the heart.

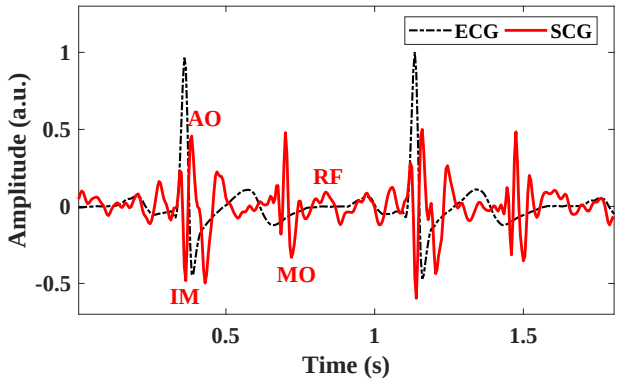

Figure 2.5: Waveforms of ECG and SCG. SCG nomenclatures: isovolumic movement (IM), aortic valve opening (AO), mitral valve opening (MO), and rapid filling (RF).

The effectiveness of SCG in facilitating diagnosis for cardiac disease have been demonstrated by multiple studies. Early research compared the diagnostic accuracy of ECG with SCG and suggested that SCG can significantly improve the accuracy for detection of anatomic and physiologic coronary artery disease (CAD) [40]. It was also reported that SCG simultaneous with ECG is helpful in detecting cardiac abnormalities such as premature ventricular contraction. With respect to at-home monitoring and remote CVDs follow-up systems, SCG-based measurement modalities were emphasized due to its robustness, feasibility and capability in detecting cardiac vibrations [41].

SCG bears superior promise as a cardiac gating signal due to its operator-independence as compared to echocardiography. The SCG accelerometer possesses a smaller footprint than the echocardiography transducer, thus significantly minimizes streak artifacts [8]. Furthermore, the inclusion of SCG in cardiac CTA gating guards against missing ECG signals when a pacemaker is used to electrically pace the cardiac cycle.

With respect to SCG as a gating signal, a recent study evaluated the potential of tri-axis SCG as a gating signal for positron emission tomography (PET) [42]. The same research group presented a dual-sensor quiescence detection and prediction method relying on a

tri-axial chest accelerometer and gyroscope for PET [43], reporting an improvement in diagnostic accuracy on both reconstructed phantom images and two patients with atherosclerotic disease.

The quiescence predicted using SCG signal can possibly achieve the same level of accuracy as the baseline echocardiography. An early research evaluated the relationship between SCG and echocardiography and reported consistency between the timing of phases of these two modalities, indicating the similar accuracy in measuring cardiac time intervals [23]. Further comparison between SCG and echocardiography [22–25] suggested that SCG can reliably capture cardiac motion and therefore potentially be a supplement to ECG in CTA gating.

The current advances in SCG signal processing include but are not limited to, the identification of quiescent heart phases [44, 45], extraction of respiratory and cardiac gating information [42], and delineation of the SCG signal [46, 47]. Multiple signal processing techniques including frequency analysis, time series regression [48] and wavelet transform [49] have been applied to ECG signals for cardiac research, but the exploration of SCG-based prediction is still at an initial stage.

2.2 Cardiovascular Physiology Basics

While there are multiple approaches to mitigate the effects of cardiac motion on cardiac CTA such as using advanced cardiac CTA reconstruction algorithms [50] or lowering the heart rate pharmacologically with β-blocker medication [51], the most straightforward approach is to avoid it altogether. In other words, acquiring data during quiescent periods.

The quiescent period exists in two portions, systole and diastole, of a cardiac cycle, as illustrated in Figure 2.6. Systole and diastole make up one cardiac cycle wherein the heart contracts to pump blood out during systole and dilates to relax during diastole [52]. Systolic quiescence occurs during the ventricular reduced ejection period and diastolic quiescence occurs during the reduced ventricular filling period [53], or more accurately diastasis. Di-

astasis occurs in the middle 1/3 of diastole. The duration of systolic and diastolic quiescent periods vary with the heart rate.

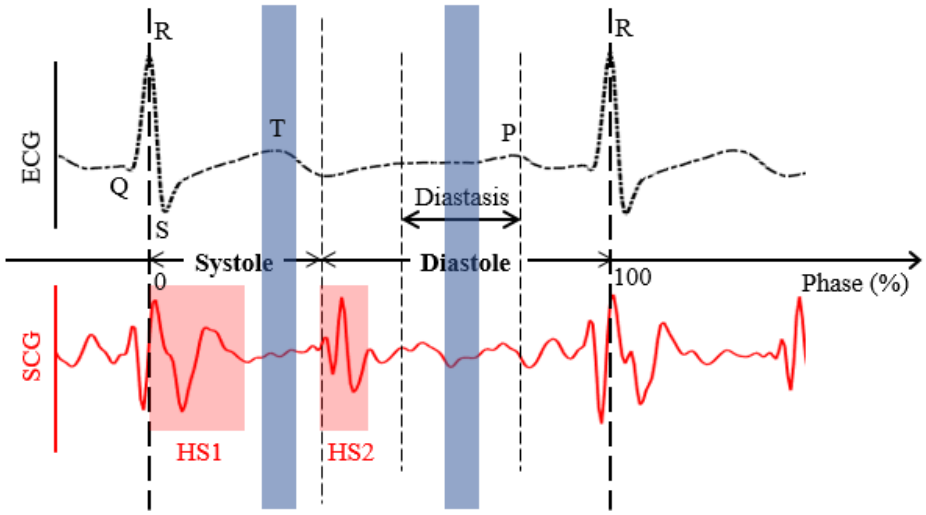

Figure 2.6: ECG and SCG traces. One cardiac cycle can be divided into systole and diastole. The heart contracts to pump blood out during systole and dilates to relax during diastole. Diastasis is the middle stage of diastole and is typically when quiescent period takes place. The systolic and diastolic quiescent periods are highlighted in blue. In SCG signal, the two high frequency accelerometric components, HS1 and HS2, are associated with the first and second heart sounds, respectively.

Heart sounds are discrete bursts of acoustic vibrations that vary in intensity, frequency, quality and duration [54]. The first heart sound is caused by the closure of atrio-ventricular valves; the second heart sound is from the closure of semilunar valves [55]. Phonocardiogram (PCG) is the graphical representation of a heart sound recording. As a standard nomenclature, the first and second heart sound denote as S1 and S2 in phonocardiogram (PCG) [56, 57]. S1 leads the onset of systolic quiescent period while S2 occurs after the systolic quiescent period and precedes the diastolic quiescent period. By placing an accelerometer on the sternum, the first and second heart sound associated waveforms can be detected [55] by the SCG. Different from PCG, SCG presents relative low frequencies of body vibrations. This research focuses on the high frequency accelerometric component of SCG which is associated with cardiac sounds. To refer to the same cardiac event but differentiate the sensing modalities, PCG and SCG, HS1 and HS2 are used in represent-

ing SCG as the source signal in this work. In addition, the term "heart sound associated waveform" refers to the high frequency accelerometric component in SCG. Table 2.1 summarizes characteristics of the first and second heart sound. These characteristics set criteria for identifying the heart sound associated waveforms in SCG to be discussed in Chapter 4.

Table 2.1: Comparison of 1^{st} and 2^{nd} Heart Sound

	S1	S2
Occurrence	Systole	Diastole
Frequency	Lower	Higher
Intensity	Stronger	Weaker
Duration	Longer ($\sim$ 0.14 s)	Shorter ($\sim$ 0.11 s)

Time intervals of cardiac events and relationship between events set a baseline for computerized processing for detecting and predicting quiescence. The QRS complex is the most visually obvious part of the ECG signal. It indicates the depolarization of the ventricles. The duration of the QRS complex is 0.06 to 0.10 second for adults. The first heart sound overlaps with the R-peak of ECG.

Yet, many relationships among cardiac features cannot be consolidated into a universal pattern that applies to everyone. The identification of cardiac features becomes challenging without a quantified pattern. For example, the T wave in an ECG represents the ventricular repolarization and occurs at the end of systole. The T wave is often observed to coincide with the 2^{nd} heart sound associated waveform in SCG. However, the T wave is in fact labile and does not have a bounded relationship with mechanical events such as the 2^{nd} heart sound. Another example is the variable duration of systole and diastole. For a healthy subject with a steady heart rate, e.g. 75 bpm, systole normally lasts about 1/3 and diastole 2/3 of a cardiac cycle [58, 59]. However, this ratio varies with heart rate [60]. Typically, the higher the heart rate, the shorter the percent of diastolic time compared to the entire duration of the cardiac cycle. However, cardiac features from cardiac patients fail to follow these rules most of the time.

In such cases, empirical conclusions are followed. It was found in [31] that end-systolic CTA reconstruction yielded sharper images for high heart rate individuals and end-diastolic reconstruction for low heart rate individuals. This indicates that for individuals with lower heart rate, for example average heart rate below 80 bpm, prospective triggering of data acquisition at diastolic quiescence is more suitable because diastolic reconstructions is more likely to achieve superior image quality as compare to systolic reconstruction [29]. As heart rate increases, the duration of cardiac cycle decreases.

2.3 Cardiac Gating

In 2004, a method and apparatus of cardiac CTA imaging using ECG and mechanical motion signals was proposed in [61, 62] but not yet validated nor implemented. In addition, this proposed method of comparing and correlating the ECG and mechanical motion signal is designed to determine the phases of cardiac region which serves for retrospective gating. In recent years, the idea of dual gating has been investigated for cardiac magnetic resonance imaging (MRI) [63] and positron emission tomography (PET) in existing works [42, 43]. This current research dates back to a proposed method and system that employs ultrasound gating during the CT scans [64]. However, this method is not feasible during the CTA exam due to the technician-dependent property of the ultrasound data acquisition. As a step forward, the current research investigates the SCG signal as a viable potential.

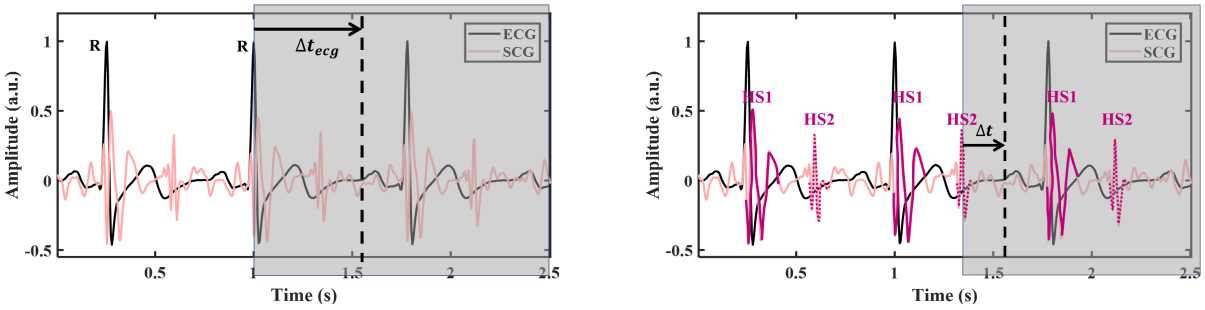

Figure 2.7: ECG-based (A) and SCG-based (B) quiescence prediction. Areas covered in grey contain succeeding unknown cardiac cycles. HS1 and HS2 are the 1^{st} and 2^{nd} heart sound associated waveforms of SCG; ΔT_{ecg} and ΔT_{scg} are predicted time durations.

Figure 2.7 demonstrates the conventional ECG- (A) and the SCG-based (B) prediction investigated in this work. HS1 and HS2 are heart sound associated waveforms of SCG in systole and diastole, respectively [54, 55]. The vertical dotted line is the quiescence derived from echocardiography which is considered as the baseline for quiescence in this study. Areas covered in grey contain succeeding unknown cardiac cycles. The predicted quiescence, measured as a time duration ΔT, is in reference to a cardiac feature within the upcoming cardiac cycle. As a demonstration, only quiescence prediction in diastole is reviewed here. Predicting ΔT_{scg} from HS2 involves less uncertainty than that from ΔT_{ecg} using R-peak of ECG as HS2 is more proximal to the quiescence, therefore this SCG-based prediction method can potentially predict quiescence more accurately.

In this work, the SCG-based prediction was developed from a waveform template matching approach in combination with a constructed delay function. Overall, SCG-based prediction was more accurate than ECG-based prediction using quiescence derived from echocardiography. To optimize the prediction accuracy on a beat-by-beat basis, a fusion-based ECG-SCG prediction relying upon an artificial neural network (ANN) was further developed. The fusion-based method quantitatively evaluates the signal quality based on features such as the power spectral density and wavelet decomposition coefficients extracted from ECG and SCG signals as the input to the ANN.

CHAPTER 3
PROTOCOL AND DATA ACQUISITION

This chapter lays an experimental foundation for the algorithm development and validations to be discussed in the following chapters 4 and 5. In addition, this chapter reviews the pre-processing procedures for raw signals of ECG and SCG.

3.1 Human Subject Protocol

Cardiac signals including ECG, SCG and echocardiography were acquired from seven healthy subjects (mean age: 31; age range: 22-48; female/male: 3/4) and eleven cardiac patients[1] (mean age: 56; age range: 31-78; female/male: 5/6). Written, informed consent was obtained from each participant and the study was conducted under the approval of the Emory University Institutional Review Board.

3.2 Custom Data Acquisition System

This work used two sets of trimodal data acquisition systems. This section introduces the custom data acquisition system which was developed by earlier work [8]. Chapter 6 will elucidate an enhanced system. Simulations presented in Chapter 4 and Chapter 5 were generated using data acquired from the old data acquisition system.

The custom data acquisition system consists of an in-house designed ECG-SCG device and a commercial ultrasound machine Sonix RP Scanner (BK Ultrasound, Richmond, BC, Canada) [8]. Figure 3.1 illustrates the data acquisition setup.

During data acquisition, each participant was resting in a supine position for approximately 30 minutes, with the single-axis linear accelerometer placed against the sternum

[1]Cardiac patients studied in this work have structural or valvular heart diseases. The rationale for including these patients was to enlarge the testing population since we scan several of these patients prior to various interventions.

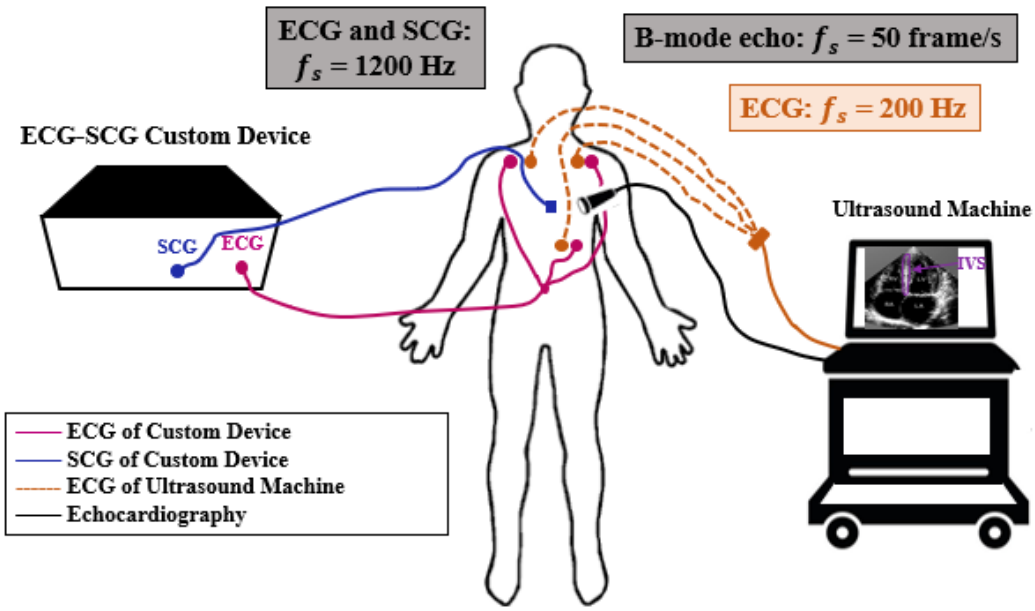

Figure 3.1: Custom data acquisition system setup.

recording dorso-ventral vibrations transmitted to the chest wall. Figure 3.2 shows the time line of data acquisition. It is worth mentioning that the participants were asked to be as motionless as possible during the recordings. However, the beginning and end of the recordings were typically heavily contaminated by motion artifacts while starting and terminating the recording, and thus approximately 7% of the noisy recordings were not included for analysis. After approximately 20 minutes of data acquisition using solely the ECG-SCG custom device, at least six sessions of B-mode echocardiography data was acquired simultaneously with the ECG-SCG recording from the custom device. Each session of echocardiography was independent and ran for 10 seconds. Afterwards, the echocardiography data was synchronized with signals acquired from the custom device by matching the ECG signals from both devices.

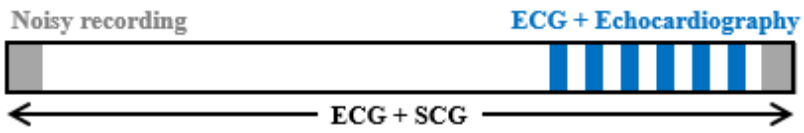

Figure 3.2: Data acquisition timeline.

The ECG-SCG custom device acquired ECG and SCG signals at the rate of 1.2 kHz. Both signals were pre-filtered and amplified by the analog end before feeding to a 16 bit analog-to-digital converter (ADC). The single-axis accelerometer (ADXL327, Analog Devices, Inc., Norwood, MA, USA) weighs approximately 5 g and and has an RMS noise of $250\,\mu g/\sqrt{Hz}$. The accelerometer was tuned to have a passband of 50 Hz [8]. While many studies used the tri-axis accelerometer to measure the mechanical movement of the heart, the tri-axis SCG signals have not yet been quantified with a widely acknowledged standardization in terms of cardiac events, particularly with the heart sound in the lateral-medial and superior-inferior directions for this study. A potential reason for this is the intersubject variability observed in the tri-axis SCG signals [65, 66]. B-mode echocardiography data, specifically apical four-chamber view, were obtained at a rate of 50 Hz and the associated ECG was recorded at 200 Hz. The redundant ECG signals from the two machines were used to align SCG and echocardiography signals, as well as to segment cardiac beats.

Retrospective cardiac CTA data were acquired and reconstructed independently using a Siemens SOMATOM Definition dual-source 64-slice CT scanner (Siemens, Erlangen, Germany) with data acquisition window length of 83 ms. This CTA data will be used for assessing the diagnostic quality of quiescence predicted from different modalities. The work discussed in Chapter 4 and 5 used Siemens SOMATOM Definition as the CTA data acquisition machine. In Chapter 6, a more advanced scanner, Siemens Force dual-source 192-slice CT scanner (Siemens, Erlangen, Germany), is introduced. The Siemens Force is the most up-to-date cardiac scanner which is able to complete data acquisition within one cardiac cycle. The temporal resolution of the Siemens Force is 66 ms. The work discussed in Chapter 6 relates to Siemens Force scanner.

3.3 Signal Pre-Processing

Raw signals were pre-processed to remove the noise and baseline drift [67]. Figure 3.3 illustrates the procedures of pre-processing. By analyzing the frequency spectrum, the ECG signal and SCG signal were conditioned by a 256^{th}-order FIR low-pass filter with a Hamming window configuration and cutoff frequency 50 Hz [68]. For the ECG signal, this was to ensure retention of the QRS complex of the ECG whose frequency range is 10-50 Hz [69]. For the SCG signal, this was to retain the high frequency components related to heart sounds that are within 10 - 50 Hz [70]. Following the low-pass filter, was a notch filter centered at 0 Hz with a cutoff of 1 Hz to remove the DC component and remaining respiratory baseline drift in ECG and SCG signals [8, 71].

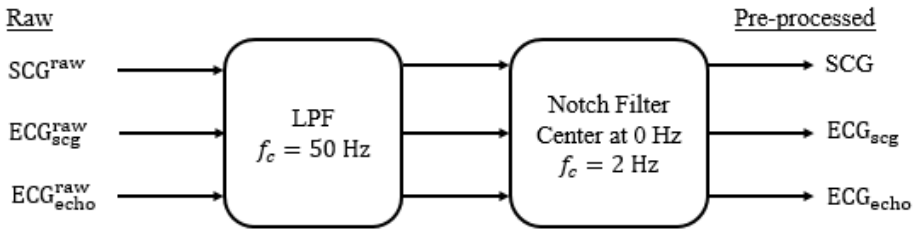

Figure 3.3: Pre-processing flowchart. f_c is the cut-off frequency of the filters.

Figure 3.4 displays the ECG and SCG signals before and after pre-processing. The spectrograms visually demonstrate the spectrum of frequencies over time for the signals before and after pre-processing. The high-frequency noise and baseline drift have been effectively removed.

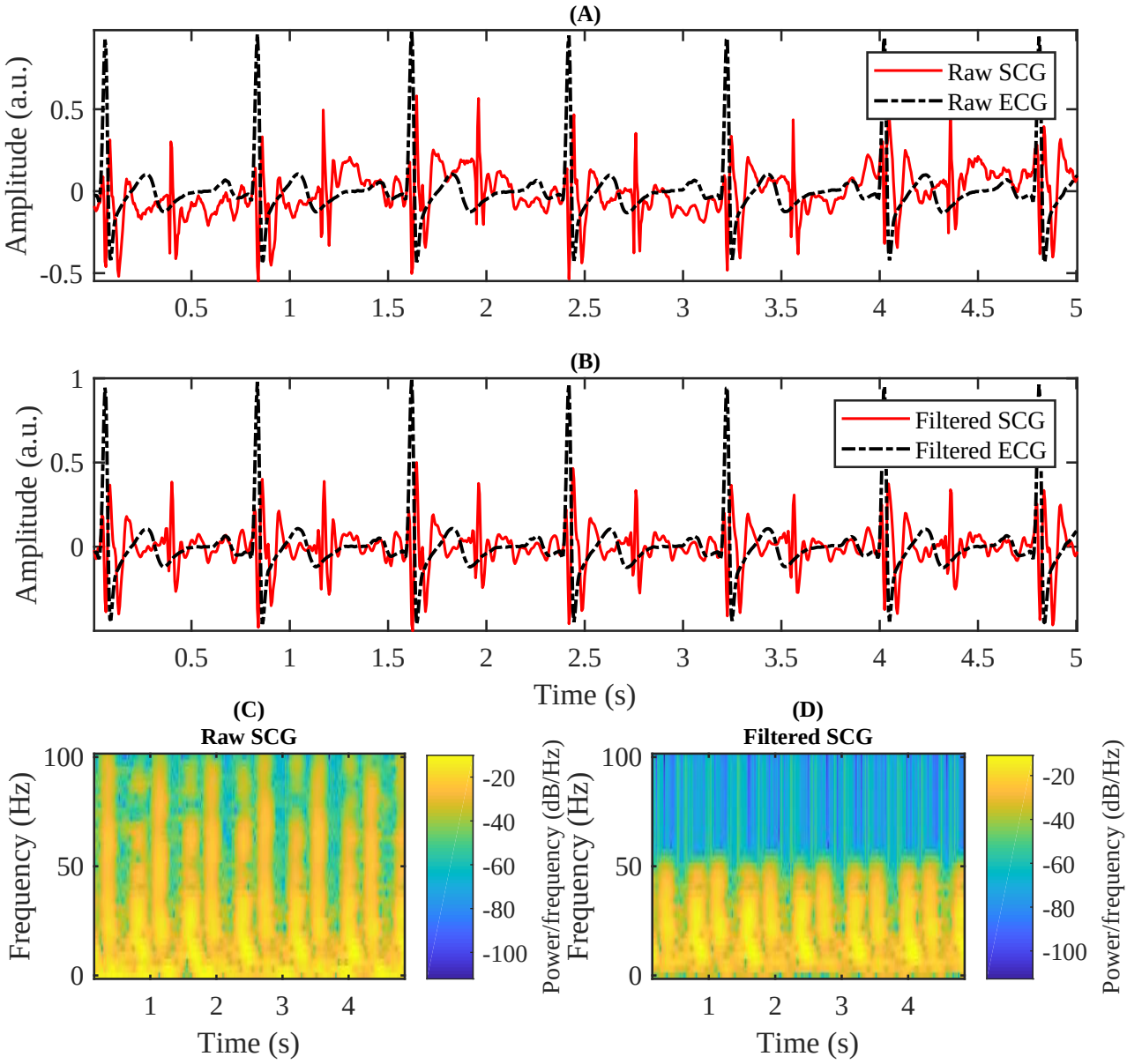

Figure 3.4: ECG and SCG signals (A) before and (B) after pre-processing. The spectrograms of SCG signals (C) before and (D) after pre-processing indicate that the high frequency noise and low-frequency baseline drift have been filtered.

CHAPTER 4

SEISMOCARDIOGRAPHY (SCG) - BASED QUIESCENCE PREDICTION

As an intermediate stage towards optimizing real-time cardiac CTA gating, investigation was first made on the cardiac-motion-based quiescence detection and prediction. SCG as a motion-based signal captures the mechanical movement of the heart and has the potential to more accurately predict cardiac quiescence than the ECG-only-based prediction [40], as introduced in Chapter 2. Thus, this part of the work focuses on SCG-based detection and prediction.

Among various identifiable features in the SCG signal such as aortic valve opening (AO) and rapid ejection (RE), the high frequency components associated with the first and second heart sounds [55, 70] were selected as the cardiac features of interest. Figure 4.1 illustrates the two detected heart sound associated waveforms, HS1 and HS2, in a synthesized SCG signal. The synthesized signal highlights the selected heart sound associated components by completely filtering out other components of the signal. The heart sound associated components are morphologically embodied as waveforms with high frequency.

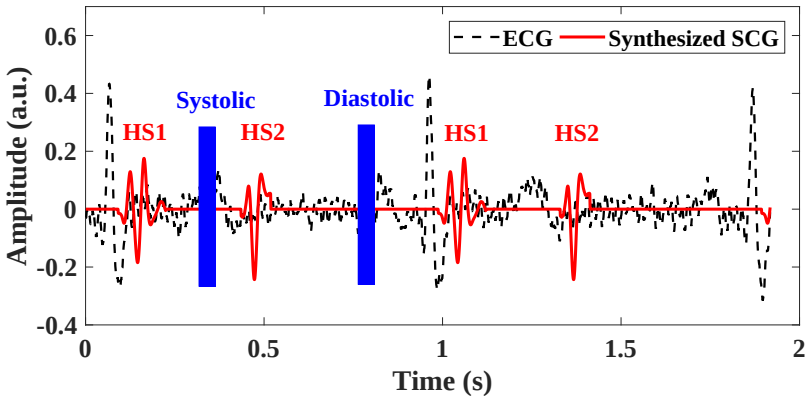

Figure 4.1: Traces of de-noised ECG and synthesized SCG signals. The heart sound associated waveforms HS1 and HS2 are presented in the synthesized signal as waveforms with high frequency and intensity. The systolic and diastolic quiescent periods are highlighted in blue.

The rationale for selecting the heart sound associated cardiac feature is twofold. Single features are instantaneous and variable, while the selected accelerometric components last for a relative longer duration and indeed encompass multiple cardiac features, making the accelerometric waveforms easier to identify. In addition, the heart sound associated accelerometric component occurs after the onset of the R-peak of ECG. As a more proximal reference to the quiescence, the heart sound associated component thereby can potentially predict the cardiac quiescence more accurately. Correspondingly, HS1 can be the reference for predicting systolic quiescence and HS2 for predicting diastolic quiescence. The temporal localization of HS1, HS2 and the corresponding quiescent periods are presented in Figure 4.1.

However, capturing the heart sound associated waveform in SCG faces challenges. Traditionally, a waveform nomenclature-based approach to identifying cardiac features is not robust. The SCG markers are inconsistent if solely following the template indices [42, 72]. Additionally, there is no universal identification template that works for signals of all individuals. The automatic annotation approach for SCG proposed in [73] shows accurate identification, but only for healthy subjects. Therefore, identifying features based on a designated template can be nontrivial and complicated.

This work developed a template matching approach to detect the heart sound associated waveforms. In summary, the template matching approach employs the similarity in morphology across heart beats by generating an ensemble template to correlate with the streaming SCG signal, thereby, the occurrence and timing of the desired waveforms are detected.

The heart sound associated waveform advances the corresponding quiescence by a duration of time, or time delay, to be predicted. This time delay can be derived from a pre-generated function, i.e., a phase delay function with respect to the heart rate, using accelerometric and echocardiographic information. Since both the waveform template and delay function are constructed out of the personalized cardiac signals, the inter-personal

variation issue in the ECG-only-based prediction is diminished. To be able to extract personalized cardiac information, a 2-3 minute pre-test is required before the actual cardiac CTA exam.

To present the SCG-based quiescence prediction in a strategic manner, a schematic diagram in Figure 4.2 shows major components for prediction. The SCG-based prediction consists of two sequential epochs, the pre-test epoch and offline prediction epoch. The 3 minute pre-test enables construction of the personalized phase delay function (Section 4.3) and waveform template (Section 4.2), which then facilitates quiescence prediction on pre-recorded cardiac signals (Section 4.6) in the offline prediction epoch. Each component for prediction is elaborated individually in the following sections. The offline prediction lays a foundation for developing a real-time prediction strategy. The real-time implementation is presented in Chapter 6.

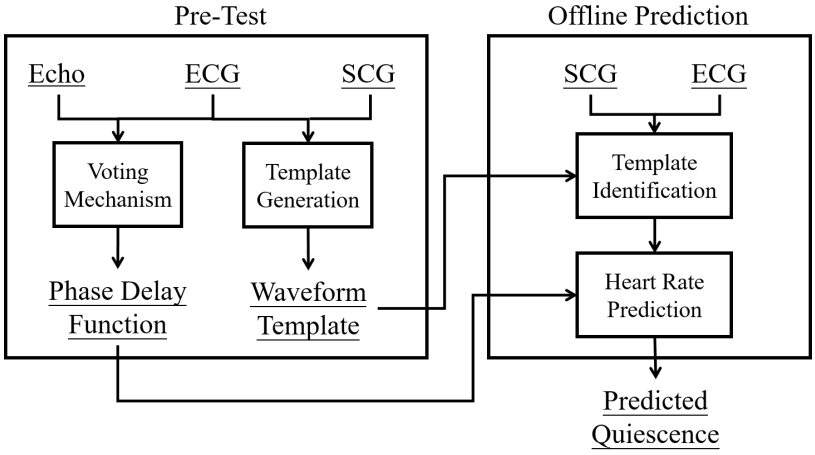

Figure 4.2: Schematic diagram of the SCG-based prediction. The SCG-based prediction consists of two sequential epochs, the pre-test epoch and offline prediction epoch. The 3 minute pre-test enables construction of the personalized phase delay function (Section 4.3) and waveform template (Section 4.2), which then facilitates quiescence prediction on pre-recorded cardiac signals (Section 4.6) in the offline prediction epoch. Major components are elaborated individually in the following sections.

The quiescence predictions were made on a beat-by-beat basis. To evaluate the prediction performance, the prediction errors were retrospectively obtained by comparing against the baseline quiescence derived from the personalized echocardiography. The prediction

errors of ECG-only- and SCG-only-based methods were then compared as a primary measure of prediction performance. Other measures include variation of prediction errors with respect to the heart rate variability and to the heart rate prediction errors.

4.1 B-mode Echocardiography Baseline

The cardiac quiescence derived from the B-mode echocardiography was used as the baseline for comparing the prediction performance of ECG- and SCG-based methods. It was reported that the approximated magnitude of velocity of the coronary vessels can be derived by estimating the motion of the interventricular septum (IVS) [36]. An earlier work developed a method to quantify the motion of IVS from the echocardiographic B-mode sequences by applying the phase-to-phase deviation measure [26]. As a result, the motion of IVS can be presented as a uni-dimensional motion signal from which systolic and diastolic quiescences can be derived, as presented in Figure 4.3.

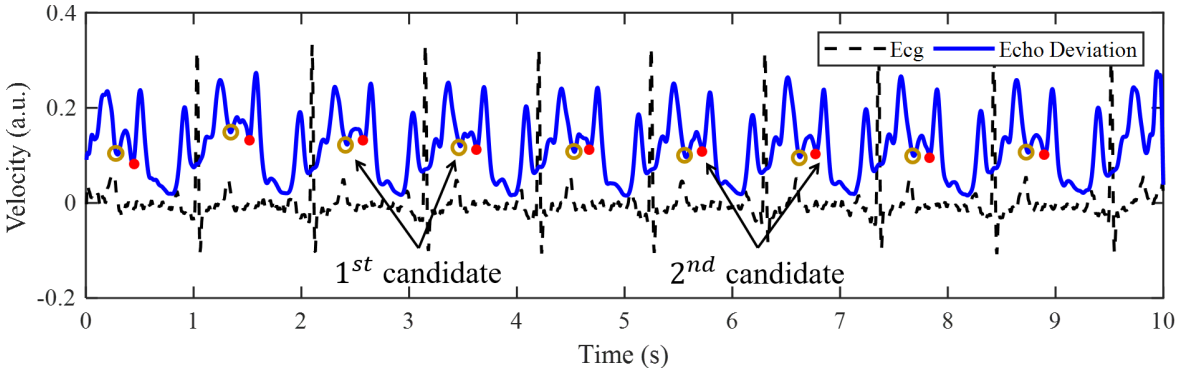

Figure 4.3: Estimated echocardiographic motion signal derived from the movement of IVS using the phase-to-phase deviation measure [26]. The voting mechanism was applied to identify robust quiescences. Two groups of candidate quiescence in systole, one in gold circle marker and the other in red solid marker, are shown as an example.

As mentioned earlier, the R-R intervals of the synchronized ECG were used to segment the uni-dimensional cardiac signals and were used to define the cardiac phases (%). Systolic and diastolic quiescent phases are characterized as phases with the least velocity in the systolic (typically with center before 60% of a cardiac cycle) and diastolic (typically with center after 60% of a cardiac cycle) periods of a cardiac cycle, respectively.

To generalize the relationship between the derived quiescence from echocardiography and the heart rate based on the acquired echocardiography data[1], a linear model was employed. A linear model is by nature straightforward and easy to implement. Previously, a linear relationship was observed between the quiescent phases (%) derived from both the SCG as well as the echocardiography with respect to the heart rate, respectively [44]. Therefore, relying on the assumption that there exists a linear relationship between a cardiac event, i.e. cardiac quiescence (in percentage phase), and the heart rate (bpm), this work condensed the cardiac signal information into pairs of slope and intercept.

However, to obtain an optimal linear model is not straightforward. The traditional approach to identifying the lowest point, or the quiescence, within a certain searching range is not robust enough to identify the same feature, because there could be more than one potential minima that meet the requirement of being a quiescence. Therefore, a voting mechanism was designed to generate a linear model with the least fitting error.

The voting process involves two epochs. The first epoch selects two candidates, both from systole or from diastole, as cardiac quiescences. These quiescences from multiple cardiac cycles form two groups of candidates. In the second epoch, the total least square residuals obtained by forming a linear fit of the quiescences with respect to the heart rate from the two groups were compared. The group with less residual was considered as an optimal linear model to generalize for the relationship between cardiac quiescence and the heart rate. Figure 4.3 marks the two groups of candidate quiescence. Figure 4.4 presents the corresponding linear fit and fitting residuals.

4.2 Template Generation and Identification

Template generation refers to extracting desired waveforms based on the pre-test data to construct a composite waveform for identifying the occurrence of the desired waveform in the offline quiescence prediction epoch. The template identification was achieved by

[1]Note that each session of echocardiography acquires 10 second duration of B-mode frames.

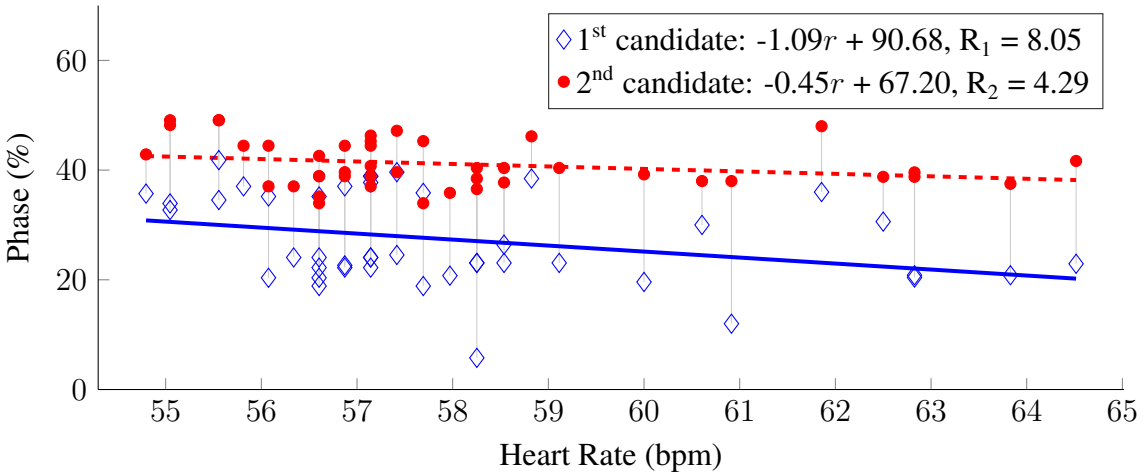

Figure 4.4: Voting mechanism selects the linear model associated with less residual. R_1 and R_2 are residuals measured by the least square error. The group formed by the 2^{nd} candidates is associated with less fitting residual ($R_2 = 4.29$) compared to the 1^{st} candidate group ($R_1 = 8.05$), thus, the linear model derived from the 2^{nd} candidate group is more suitable to generalize the relationship between the quiescent phase and heart rate.

a template matching approach. In this work, the desired waveform is the high frequency accelerometric component related to the heart sounds. As elaborated in Chapter 3.3, the raw data was first pre-processed to obtain a conditioned signal for the follow-on processing.

To extract the waveforms associated with the first and second heart sounds, temporal windows were designed individually based on statistics from previous studies on heart sounds [54, 74]. The primary configurations of the searching window are the window length and region of occurrence within a cardiac cycle. Normally, the S1 is lower in frequency and lasts for a longer duration than the S2 [54]. The average duration of the S1 and S2 components are approximately 0.14 second and 0.11 second, respectively [74]. Since the custom-built device synchronously acquired ECG and SCG signals at a rate of 1.2 kHz, accordingly, the systolic and diastolic searching window were set with 160 and 100 samples in length, respectively. The heart sound associated waveforms occur prior to the corresponding quiescent period, indicating that the region of occurrence can be estimated based on the timing of the quiescent period. In a prior study, the timing of the quiescent periods was studied by analyzing SCG signals acquired from seven healthy subjects and eleven

patients with valvular or structural cardiac disease [45]. It was found that on average, the center of systolic and diastolic quiescent periods were at 29% and 76%, respectively, for healthy subjects, and 33% and 79%, respectively, for patients with CVD. Therefore, the searching range of the two heart sound associated waveforms were set from $S_{start} = 1\%$ to $S_{end} = 30\%$ and $D_{start} = 30\%$ to $D_{end} = 65\%$ for healthy subjects, and 1% to 33% and 33% to 79% for the cardiac patients.

The procedures for generating the heart sound associated waveform templates correspond to HS1 and HS2 consists of the following steps:

1. Extract the waveform associated with the heart sound with the aforementioned windowed searching approach in each cardiac cycle. For a specific subject, denote the the waveform from the i-th cardiac cycle $w(i)$, $i = 1, ..., N$.

2. Use the longest waveform as the reference length, and padding zero at the end of the rest of the waveforms to achieve equal length as the reference length, and obtain the composite waveform $\bar{w} = \frac{1}{N}\sum_{i=1}^{N} w(i)$.

3. Apply Hilbert transform to obtain an upper (e_{upper}) and lower envelope (e_{lower}) around the composite waveform $\bar{w}$. The difference envelope is the difference between the two envelopes $\bar{w}_d = e_{upper} - e_{lower}$ [55]. The envelopes are displayed in Figure 4.5.

4. Locate the peak of the difference envelope $\bar{w}_d$, τ_P, measured as the sample index within the difference envelope. The delay from the most recent R-peak to the τ_P becomes $\tau_{PR} = \tau_P + \bar{L} * search_{start}$, where $search_{start} = S_{start}$ or D_{start} and $\bar{L}$ is the average cycle length.

5. Recapture waveform associated with the heart sound by extracting the waveform around τ_{PR} in each cardiac cycle and τ_{PR} being the center of the window and with the window details the same as aforementioned.

6. Generate the waveform template by averaging the recaptured waveform and normalize to unit energy. The unite energy is calculated by taking the square root of the sum of squares on a sequence.

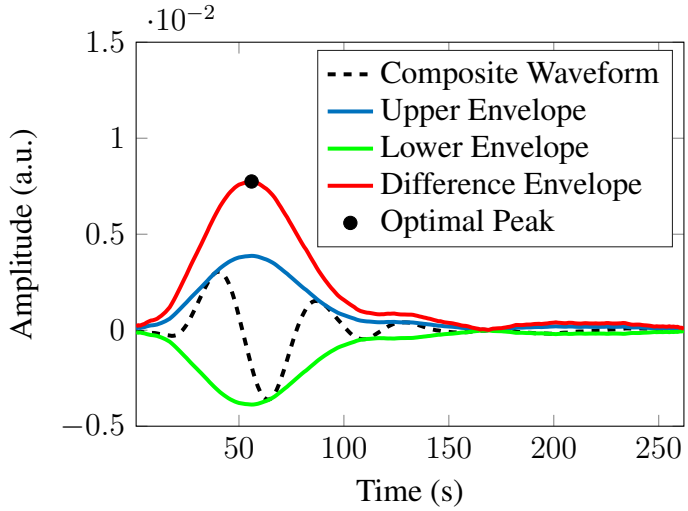

Figure 4.5: The composite waveform and envelopes. The difference envelope is the difference between the upper and lower envelope formed using Hilbert transform on the composite waveform. The peak of the difference envelope is considered the optimal peak of the composite waveform.

The generation of the composite waveform and difference envelope in steps 2 and 3 are for multiple purposes. The composite waveforms are able to narrow down the noise and artifacts and increase the robustness in determining the optimal peak of the heart sound associated waveform. The difference envelope increases the temporal resolution in detecting the optimal peak of the heart sound associated waveform. The peak of the difference envelope, as illustrated in Figure 4.5, indicates the temporal position corresponding to the peak of the waveform. Steps 1 - 4 approximately capture waveform of the high frequency accelerometric components and step 5 - 6 more accurately recaptures the waveform based on the timing of the optimal peak τ_{PR}.

The application of the Hilbert transform facilitates the construction of the template waveform. Any real signal $s(t)$ can be written uniquely in the form $s(t) = e(t)\cos(2\pi f_c t + \theta(t))$ where $e(t)$ is the envelope and $\theta(t)$ is the phase of $s(t)$. The relationship of the signal

and its Hilbert transform is $\tilde{s}(t) = \frac{1}{\sqrt{2}} e(t) e^{j\theta(t)}$. It is noted that the Hilbert transform was originally exploited for periodic functions. The accelerometric waveform associated with the two heart sounds in this study are sinusoidal-like (and thus quasi-periodic), so the Hilbert transform works well in constructing the desired envelopes. However, it is important to note that the Hilbert transform may fail in accurately capturing the envelopes of some skewed waveforms.

As part of the offline prediction epoch (refer to Figure 4.2), the heart sound associated waveforms in a streaming SCG signal can be identified by correlating the generated template waveform with the conditioned SCG signal in the time domain. As a result of the correlation, the resulted peaks indicate where the center of the desired HS1 and HS2 waveforms locate.

4.3 Phase Delay Function

The phase delay function characterizes the relationship between the heart rate and the delay in phases (%) from the cardiac feature, i.e., the optimal peak of HS1 or HS2 in SCG, to the corresponding cardiac quiescence derived from the echocardiography. Obtaining the phase delay function requires generation of the SCG waveform function and the echocardiographic quiescence function discussed in Section 4.1.

It has been discussed in Section 4.1 that a linear function has the potential to model the relationship between the cardiac feature and heart rate, indicating that there may exist a linear relationship between the optimal peak (in phase) of the SCG waveforms and the heart rate. Figure 4.6 shows the systolic and diastolic SCG waveform function derived from a set of pre-test signals.

For both of the linear functions, one was the SCG waveform function and the another was the echocardiographic quiescence function, an outlier removal technique was applied to get an unbiased linear function. Specifically, outlier removal was applied to both the variables, the identified cardiac feature and heart rate. For the set of identified features,

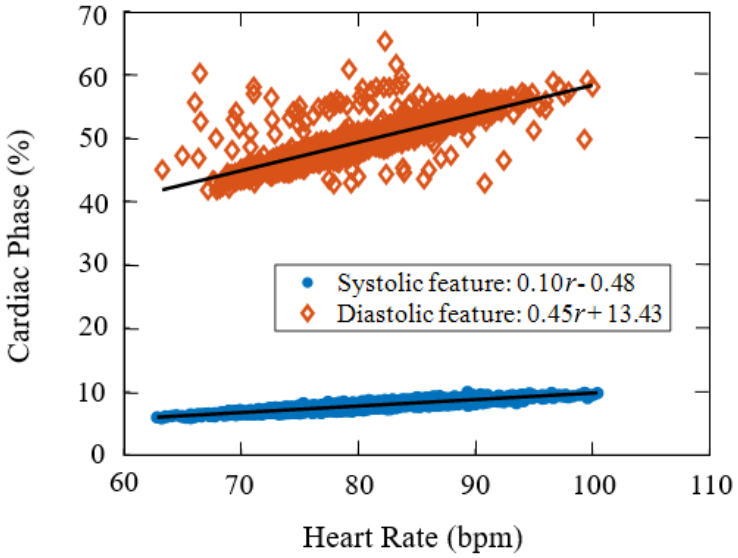

Figure 4.6: Heart sound associated waveforms in phase (%) as a linear function of the heart rate (bpm).

any sample that strays away from the linear fit by more than two standard deviations was removed. For the heart rates, any sample that strays away from the average heart rate for more than three standard deviation was removed. A new linear fit was then constructed after removing the outliers from both variables.[2] Therefore, the difference between the two linear functions generates another linear function, namely, the phase delay function. The systolic and diastolic phase delay functions are presented in Figure 4.7.

The phase delay functions for systole and diastole can be mathematically represented as

$$P^{sys}_{delay}(r) = P^{sys}_{echo}(r) - P^{sys}_{scg}(r), \tag{4.1}$$

$$P^{dias}_{delay}(r) = P^{dias}_{echo}(r) - P^{dias}_{scg}(r), \tag{4.2}$$

where $P^{sys}_{scg}(r)$ and $P^{dias}_{scg}(r)$ are phases of the systolic and diastolic optimal peaks detected from the SCG waveforms, respectively, for heart rate r. $P^{sys}_{echo}(r)$ and $P^{dias}_{echo}(r)$ are systolic and diastolic quiescent phases derived from echocardiography, respectively.

[2]The cardiac features, i.e., the optimal peaks, have more natural variance as compared to the heart rates, so the outlier remover for cardiac phases was set to have a tighter range of tolerance.

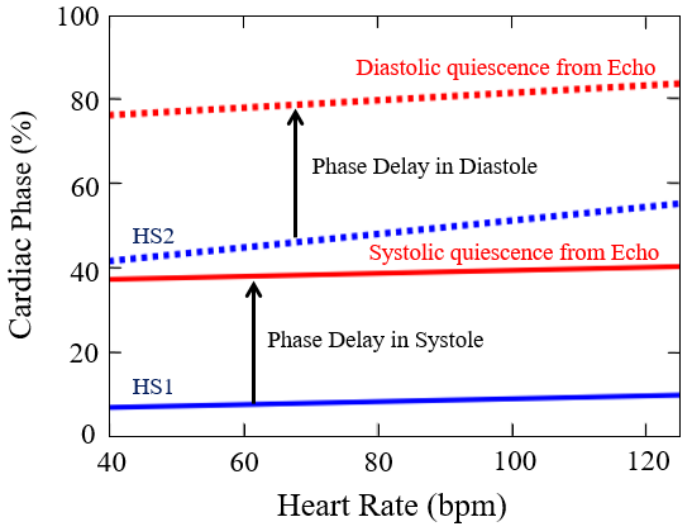

Figure 4.7: The phase delay functions in systole and diastole, respectively.

In this work, two forms of phase delay functions were obtained, one was the patient-specific and the other was the cohort-specific function. The former one was derived using the patient-specific echocardiography data. The latter one was derived from an average echocardiography quiescence function, namely,

$$P^{sys}_{delay}(r) = \bar{P}^{sys}_{echo}(r) - P^{sys}_{scg}(r), \tag{4.3}$$

$$P^{dias}_{delay}(r) = \bar{P}^{dias}_{echo}(r) - P^{dias}_{scg}(r), \tag{4.4}$$

where $\bar{P}^{sys}_{echo}(r)$ and $\bar{P}^{dias}_{echo}(r)$ are the average systolic and diastolic echocardiography quiescence functions, respectively, obtained by taking the mean of the echocardiography quiescent quiescence functions of individuals within the same cohort, with the application of the leave-one-out method. A cohort is a group consisting of either healthy subjects or cardiac patients. A general representation of the average echocardiography quiescence function is

$$\bar{P}_{echo}(r) = \frac{1}{N-1}\sum_{j} P_{echo}(r_j), \tag{4.5}$$

where j is the index of the subjects/patients exclusive of the current subject of study and

N is the total number of subjects within the same cohort. Accordingly, two forms of evaluation are to be presented in Section 5.5. Both forms assess the potential of SCG as a gating tool. However, the cohort form is applied in the actual CTA data acquisition scenario and the patient-specific echocardiography is only for validating the accuracy of the ECG- and SCG-based prediction. This is because acquiring the patient-specific echocardiography is limited by its operator-dependent property and thus is not feasible during CTA data acquisition.

4.4 ECG Gating Function

Currently, prospective CTA is triggered relying on an ECG signal. Specifically, a predefined piece-wise constant gating function with respect to the predicted heart rates is employed, as mentioned in Chapter 2.1.1. Previous literature has extensively studied the optimal systolic and diastolic reconstruction intervals for ECG-based CTA using retrospective analysis. This work selectively uses a comprehensive gating function from [28] (corresponds to the first example in Figure 2.3),

$$P_{ecg}(\hat{r}) = \begin{cases} 65\% & \hat{r} \leq 60 \text{ bpm}, \\ 75\% & 60 \text{ bpm} < \hat{r} \leq 70 \text{ bpm}, \\ 85\% & 70 \text{ bpm} < \hat{r} \leq 83 \text{ bpm}, \\ 35\% & \hat{r} > 83 \text{ bpm}, \end{cases} \tag{4.6}$$

where $\hat{r}$ is the predicted heart rate. P_{ecg} is the predicted quiescence phase (%) measured as a delay from the start of the most recent R-peak of the ECG to the start of the quiescent period. As an important aside, the given function provides the phase of the triggering signal with respect to the beginning of the systolic and diastolic quiescent period rather than the center of the acquisition window. A linear conversion reported in Chapter 2.1.1 was applied to the gating function, making it a heart-rate-dependent piece-wise function for the purpose

of this work.

4.5 Heart Rate Prediction

In prospective CTA, as part of the quiescence prediction, the upcoming heart rate is unknown and needs to be predicted. Various typical statistical models were experimented on the heart rate sequence. The four models that were experimented include taking the mean of the previous six heartbeats[3], linear regression (LR) [75] using the previous six heartbeats, cubic spline (CS) [76] using the previous six heartbeats, and the autoregressive model (AR) [77] of order 3. The comparison was based on the mean square error (MSE) associated with each model. The results using the data of a subject whose average heart rate is $\bar{r} = 83.02$ bpm (corresponds to heartbeat of 0.72 s) and heart rate variability $\sigma_r = 5.76$ ms are illustrated in Figure 4.8. It was observed that the LR model resulted in the least MSE. Thus, this work used the LR model for predicting the heart rate.

The mathematical form of LR_6 can be expressed as

$$r_n = LR_6(r_i) = \sum_{i=n-6}^{n-1} \beta_n r_i + \epsilon_n, \tag{4.7}$$

where r_n is the current heartbeat to be predicted, r_i is the previous heartbeat with index i, and ϵ_n is the n-th noise term, that is, random error. As a side note, LR is a useful linear model that can be applied to real-valued time series to recognize the pattern of a set of samples and thus is an appropriate model in predicting the instantaneous heart rate.

4.6 Pre-Test and Offline Prediction

To validate the proposed SCG-based prediction method, pre-test and offline prediction were carried out on a set of data acquired from seven healthy subjects (mean age: 31; age range: 22-48; female/male: 3/4) and eleven cardiac patients (mean age: 56; age range: 31-78;

[3]To differentiate with the measurement in beat per minute (bpm) which is typically called heart rate, the term heartbeat is used to represent the duration of a cardiac cycle in time, i.e. seconds or milliseconds.

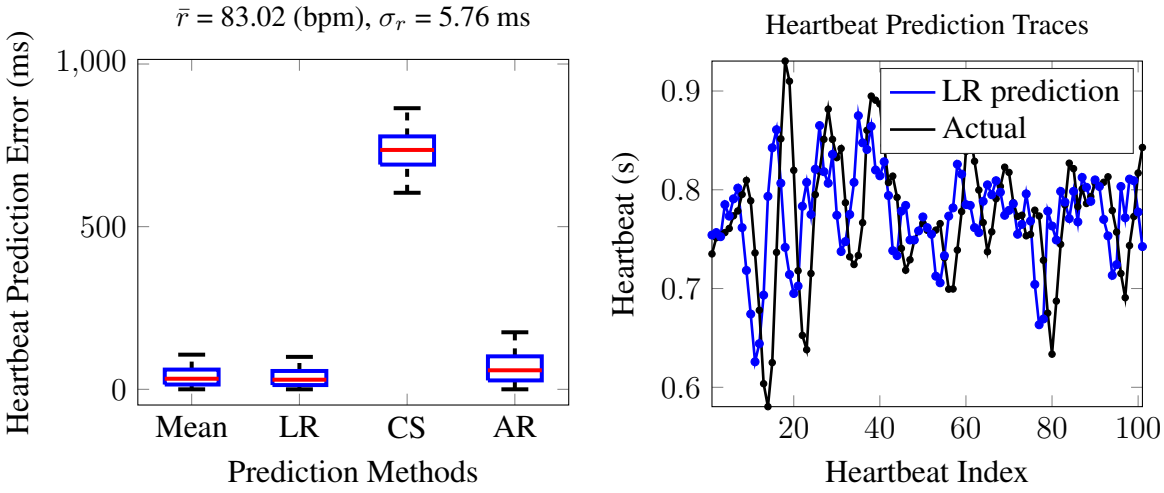

Figure 4.8: Left: comparison of different heart rate prediction methods using a patient's heart rate sequence; Right: heartbeat traces of linear regression method. The mean heart rate is 83.02 bpm and heart rate variability [78] is 5.76 ms. Mean: mean of the previous six heartbeats; LR: linear regression; CS: cubic spline using the previous six heartbeats; AR: autoregressive model of order 3. The red marks indicate the median values, and the bottom and top edges of the box indicate the 25th and 75th percentiles, respectively, and the whiskers are outliers.

female/male: 5/6). The data acquisition process and subject protocol were described in Chapter 3.

For each subject, the synchronized ECG and SCG data were divided into two parts, one for pre-test and one for offline prediction. Inspired by the rule of thumb in machine learning, the ratio of the number of cardiac cycles for pre-test and prediction is 4 to 1 [75]. The two datasets are exclusively independent continuous cardiac cycles.

In the offline prediction epoch, the SCG waveform template generated in the pre-test epoch correlates with the streaming SCG data in the prediction dataset to identify the timing of the heart sound associated waveforms t_{scg}. With the heart rate prediction algorithm presented in Section 4.5 that predicts the heart rate $\hat{r}$ (bpm) for the current cardiac cycle, the phase of the current waveform becomes $P^w_{scg} = t_{scg} \times \hat{r}/60$. Therefore, then the predicted quiescent phase from SCG is $P_{scg}(\hat{r}) = P^w_{scg} + P_{delay}(\hat{r})$ where $P_{delay}(\hat{r}) = P_{echo}(\hat{r}) - P^w_{scg}(\hat{r})$ as reported in Section 4.3.

4.7 Performance Metrics

Four performance metrics were examined as listed below:

1. Waveform identification rate. The percentage of valid waveforms that were identified over cardiac cycles in the pre-test dataset. This measures the robustness of the proposed waveform identification algorithm.

2. The variation of phase error along with the change of heart rate.

3. The variation of phase error against the heart rate error.

4. The overall phase error versus heart rate variation for each subject.

The phase error is defined as the absolute difference between the predicted quiescent phase and that derived from the patient-specific echocardiography baseline,

$$E_{scg}(r_n) = |P_{scg}(\hat{r}_n) - P_{echo}(r_n)|, \tag{4.8}$$

or,

$$E_{ecg}(r_n) = |P_{ecg}(\hat{r}_n) - P_{echo}(r_n)|, \tag{4.9}$$

where n is the index of a specific cardiac cycle; r_n represents the true heart rate and $\hat{r}_n$ is the predicted heart rate. While the predict phases depend on the predicted heart rate, the baseline quiescent phase is obtained from the echocardiography linear function against true heart rate.

The heart rate error is the numerical difference between the true heart rate and the predicted heart rate, presented as

$$E_{hr}(r_n) = r_n - \hat{r}_n. \tag{4.10}$$

The average heart rate error for a specific subject is the mean of the absolute value of

the heart rate values, presented as

$$\bar{E}_{hr} = \frac{1}{N}\sum_{n=1}^{N}|E_{hr}(r_n)|. \tag{4.11}$$

For each subject, the average phase error is the mean of all the phase error over all cardiac cycles in the prediction dataset, presented as

$$\bar{E}_{scg} = \frac{1}{N}\sum_{n=1}^{N}E_{scg}(\hat{r}_n), \tag{4.12}$$

or,

$$\bar{E}_{scg} = \frac{1}{N}\sum_{n=1}^{N}E_{ecg}(\hat{r}_n). \tag{4.13}$$

Heart rate variability is a measure of the variation in heartbeats within a certain time frame. The unit of measurement is in millisecond (ms) [47]. While there are multiple ways to calculate the HRV, for example, the number of pairs of adjacent normal RR intervals that differ by more than 50 ms, this work used the mean-square of the successive differences in time between cardiac cycles [78, 79], presented as

$$var_{hb} = \frac{1}{N}\sum_{n=1}^{N}(r_n - \mu_{hb})^2, \tag{4.14}$$

where μ_{hb} is the mean of heartbeats of cardiac cycles in the prediction dataset. The duration of heartbeat is measured in time. The relationship of the heartbeat (*hb*) measured in time and heart rate (*r*) measured in bpm is

$$hb = \frac{60}{r}. \tag{4.15}$$

As discussed in Section 4.3, the SCG-based prediction can be derived using two approaches, depending on the type of the phase delay function, either patient-specific or cohort-specific. Therefore, SCG-based prediction derived from both approaches were eval-

uated against the aforementioned metrics.

4.8 Results

The ECG- and SCG-based prediction results are summarized in Table 4.1, with the phase errors presented both for patient-specific and cohort-specific forms. While the cardiac phase normalized over a cardiac cycle for HRV is effective in mathematical modeling, the evaluation of temporal error is what essentially contributes to the degradation in CTA image quality, since the sensitivity to mistiming varies among individuals and the predicted HR. Therefore, the corresponding errors in time (millisecond) are also presented. Note that the cardiac cycles where waveform detection failed were omitted, and therefore were not included in the calculation of phase errors. In the actual CTA data acquisition scenario, cardiac cycles in which the waveform detection fails will by default apply the ECG-based prediction. On average, the prediction errors of SCG-based prediction in systole and diastole are 42.97 ms (5.53%) and 62.01 ms (8.21%), respectively, and 50.88 ms (7.17%) and 72.38 ms (8.52%) with ECG-based prediction.

Table 4.1: Error Statistics

Healthy Subjects								
Subject	Avg HR (bpm)	HRV (ms)	Average Phase Error (%)					
			Absolute Average Error (millisecond)					
			Personalized SCG		Cohort SCG		ECG	
			Systole	Diastole	Systole	Diastole	Systole	Diastole
H1	58	41	3.30 ± 5.26	5.50 ± 6.01	4.75 ± 4.07	6.62 ± 4.18	-	5.84 ± 4.06
			30.76 ± 48.77	52.36 ± 6.01	52.03 ± 50.75	62.12 ± 41.20	-	56.16 ± 42.30
H2	60	48	1.5 ± 2.38	2.54 ± 4.40	4.23 ± 1.94	8.61 ± 2.96	5.73 ± 3.37	4.89 ± 3.13
			13.06 ± 23.67	22.47 ± 4.4	37.06 ± 23.18	70.27 ± 21.97	43.23 ± 20.18	42.47 ± 27.63
H3	68	28	2.94 ± 4.99	3.46 ± 6.34	2.43 ± 4.04	6.12 ± 4.80	10.62 ± 10.61	6.07 ± 3.88
			25.22 ± 40.96	30.66 ± 6.34	22.39 ± 33.58	54.91 ± 33.31	63.81 ± 55.47	56.22 ± 35.65
H4	73	50	2.36 ± 4.74	2.72 ± 3.66	4.44 ± 4.78	2.46 ± 4.13	3.25 ± 3.81	9.15 ± 2.72
			18.99 ± 39.27	21.76 ± 3.66	36.82 ± 40.28	17.95 ± 30.60	31.66 ± 52.76	74.2 ± 23.83
H5	77	50	2.00 ± 2.48	1.70 ± 3.20	3.06 ± 2.07	4.04 ± 3.67	11.37 ± 2.94	7.77 ± 3.16
			14.59 ± 19.45	11.97 ± 3.2	21.84 ± 16.19	24.66 ± 21.00	76.16 ± 14.57	59.45 ± 27.19
H6	84	19	2.40 ± 3.96	0.92 ± 2.45	5.56 ± 1.47	2.78 ± 2.80	8.82 ± 0.88	5.30 ± 1.03
			17.25 ± 28.20	6.71 ± 2.45	39.70 ± 8.28	18.51 ± 14.18	62.36 ± 5.02	38.86 ± 8.48
H7	92	58	0.88 ± 0.94	1.68 ± 1.31	5.10 ± 1.79	4.83 ± 2.23	3.55 ± 1.23	7.68 ± 0.47
			6.04 ± 6.05	11.41 ± 1.31	34.55 ± 11.95	32.11 ± 13.49	23.37 ± 6.92	53.82 ± 5.25
Mean	72	42	2.20	2.65	4.23	5.07	7.22	6.67
	72	42	17.99	22.48	34.91	40.08	50.10	54.45
Std	12	13	0.82	1.50	1.11	2.20	3.54	1.55
	12	13	8.12	15.5	10.42	21.89	20.59	11.60

Cardiac Patients								
Subject	Avg HR (bpm)	HRV (ms)	Average Phase Error (%)					
			Absolute Average Error (millisecond)					
			Personalized SCG		Cohort SCG		ECG	
			Systole	Diastole	Systole	Diastole	Systole	Diastole
P1	52	20	2.11 ± 3.31	9.69 ± 11.17	1.95 ± 3.23	11.24 ± 6.01	2.51 ± 2.08	14.66 ± 3.22
			22.90 ± 35.23	107.36 ± 11.17	22.36 ± 35.05	124.19 ± 69.68	22.14 ± 16.45	157.34 ± 25.00
P2	54	65	1.21 ± 1.71	5.45 ± 6.29	1.85 ± 1.52	10.91 ± 4.59	-	17.91 ± 4.47
			13.10 ± 18.30	59.51 ± 6.29	20.45 ± 14.52	120.84 ± 56.24	-	192.72 ± 42.73
P3	54	208	2.84 ± 3.42	4.59 ± 4.10	6.16 ± 3.28	13.40 ± 3.77	1.22 ± 0.40	10.82 ± 0.85
			19.11 ± 2.40	31.33 ± 4.10	32.054.15	21.76 ± 7.40	8.11 ± 2.46	76.22 ± 10.06
P4	63	63	2.08 ± 3.42	2.81 ± 4.10	3.09 ± 3.28	6.77 ± 3.77	-	3.64 ± 3.06
			19.72 ± 32.19	26.97 ± 4.10	28.79 ± 29.41	62.33 ± 30.45	-	34.47 ± 27.08
P5	64	38	2.22 ± 2.22	4.27 ± 3.40	2.68 ± 2.03	3.48 ± 4.79	-	7.75 ± 1.29
			18.2218.03	35.14 ± 3.40	21.7 ± 16.36	25.08 ± 30.10	-	63.64 ± 11.41
P6	65	60	4.47 ± 2.56	5.92 ± 7.40	0.05 ± 2.39	9.75 ± 8.90	3.08 ± 1.12	8.93 ± 4.54
			38.79 ± 19.39	52.12 ± 7.40	24.51 ± 15.26	66.85 ± 71.45	31.56 ± 15.53	76.43 ± 41.73
P7	73	57	3.34 ± 3.37	2.89 ± 5.20	13.09 ± 3.63	11.64 ± 4.20	14.96 ± 0.8	0.2 ± 0.41
			24.68 ± 25.26	21.38 ± 5.20	96.15 ± 27.08	84.78 ± 29.35	108.36 ± 3.44	1.48 ± 2.33
P8	81	170	3.59 ± 5.10	15.37 ± 14.33	3.27 ± 4.64	12.05 ± 13.12	13.74 ± 13.68	11.54 ± 8.64
			31.87 ± 49.61	141.55 ± 14.33	31.09 ± 49.62	95.59 ± 115.28	91.58 ± 75.69	96.26 ± 78.36
P9	84	147	2.98 ± 3.54	9.47 ± 9.67	28.31 ± 4.48	11.98 ± 7.43	18.46 ± 0.42	11.6 ± 1.93
			21.15 ± 25.54	67.98 ± 9.67	201.48 ± 36.33	76.87 ± 53.61	131.32 ± 17.54	81.42 ± 16.18
P10	87	29	2.57 ± 4.17	6.31 ± 5.74	2.13 ± 4.03	12.28 ± 6.18	2.45 ± 0.73	16.59 ± 2.90
			18.38 ± 29.91	44.69 ± 5.74	15.21 ± 28.96	85.6 ± 45.63	17.16 ± 5.90	123.13 ± 26.06
P11	102	3	3.67 ± 1.84	0.48 ± 0.37	12.01 ± 2.91	27.92 ± 0.61	0.51 ± 0.12	-
			20.92 ± 10.54	2.76 ± 0.37	67.58 ± 14.58	159.48 ± 3.65	2.95 ± 0.74	-
Mean	70	78	2.76	5.95	6.82	11.34	7.12	10.37
	70	78	22.62	53.71	51.03	83.94	51.65	90.31
Std	16	66	0.94	4.21	8.16	6.18	7.28	5.52
	16	66	7.11	40.15	55.5	41.19	50.55	56.06

† H represents healthy subjects and P represents cardiac patients.

In Table 4.2 and Table 4.3, the two cohorts, healthy subjects and cardiac patients, are further grouped based on their heart rates, as low heart rate (< 75 beats per minute) or high heart rate (≥ 75 beats per minute). The numerical results report the average phase error and the corresponding standard deviation of each group.

Table 4.2: Average error calculated with patient-specific phase delay function

		$\bar{E}_{scg}^{systole}$ (%)	$\bar{E}_{scg}^{diastole}$ (%)	$\bar{E}_{ecg}^{systole}$ (%)	$\bar{E}_{ecg}^{diastole}$ (%)
		Absolute Average Error (millisecond)			
Healthy Subjects	Low HR (< 75 bpm)	2.52 ± 0.78	3.55 ± 1.35	6.53 ± 3.75	6.48 ± 1.84
		22.01 ± 7.66	31.81 ± 14.28	46.23 ± 16.28	57.26 ± 13.01
	High HR (≥ 75 bpm)	1.76 ± 0.78	1.43 ± 0.44	7.91 ± 3.98	6.91 ± 1.40
		12.63 ± 5.86	10.03 ± 2.89	53.97 ± 27.38	50.71 ± 10.64
Cardiac Patients	Low HR (< 75 bpm)	2.61 ± 1.05	4.94 ± 2.34	5.44 ± 6.39	9.13 ± 6.08
		22.36 ± 8.12	47.69 ± 29.63	42.54 ± 44.93	86.04 ± 67.03
	High HR (≥ 75 bpm)	3.20 ± 0.52	7.90 ± 6.21	8.79 ± 8.96	13.24 ± 2.89
		23.08 ± 6.00	64.24 ± 58.17	60.75 ± 61.02	100.27 ± 21.14

Table 4.3: Average error calculated with the cohort-specific phase delay function

		$\bar{E}_{scg}^{systole}$ (%)	$\bar{E}_{scg}^{diastole}$ (%)	$\bar{E}_{ecg}^{systole}$ (%)	$\bar{E}_{ecg}^{diastole}$ (%)
		Absolute Average Error (millisecond)			
Healthy Subjects	Low HR (< 75 bpm)	3.96 ± 1.04	5.95 ± 2.56	6.53 ± 3.75	6.48 ± 1.84
		37.07 ± 12.10	51.31 ± 23.11	46.23 ± 16.28	57.26 ± 13.01
	High HR (≥ 75 bpm)	4.57 ± 1.33	3.88 ± 1.03	7.91 ± 3.98	6.91 ± 1.40
		32.03 ± 9.19	25.09 ± 6.81	53.97 ± 27.38	50.71 ± 10.64
Cardiac Patients	Low HR (< 75 bpm)	4.12 ± 4.36	9.59 ± 3.37	5.44 ± 6.39	9.13 ± 6.08
		35.14 ± 27.22	72.26 ± 41.06	42.54 ± 44.93	86.04 ± 67.03
	High HR (≥ 75 bpm)	11.43 ± 12.08	16.06 ± 7.90	8.79 ± 8.96	13.24 ± 2.89
		82.60 ± 103.26	86.02 ± 9.37	60.75 ± 61.02	100.27 ± 21.14

Note that in Table 4.1, there are average phase errors in systole that do not apply to ECG. This is because the ECG-gating function is a one-ton-one mapping of a predicted heart rate to a quiescent phase. For subject H1 whose overall heart rate is low, all the

predicted quiescent phases fall within diastole. Therefore, this subject only has prediction errors in diastole.

Table 4.2 reports the results generated using the patient-specific phase delay function. The SCG-based prediction demonstrated less prediction error (measured in ms) and less standard deviation for all subjects, while ECG yielded more prediction errors and larger variance in all cases.

Table 4.3 shows the results generated from the cohort phase delay function. For healthy subjects, the SCG-based prediction yielded less prediction error (measured in ms) than ECG, both in systole and diastole. For cardiac patients, particularly with high heart rate, SCG-based prediction in systole produced slightly more average errors (measured in ms) than ECG. However, the diastolic prediction errors measured in time was significantly reduced using the SCG-based prediction.

4.8.1 Waveform Identification Rate

The waveform identification rate is referred to as the number of valid waveforms associated with heart sounds identified within each cardiac cycle over the totally number of cardiac cycles in the prediction dataset. Figure 4.9 shows the identification rate of the first and second waveform of each individual. The first seven data samples correspond to the seven healthy subjects and the following eleven data samples correspond to the cardiac patients. The average identification rate over the 18 subjects for the first waveform is 78.8%, and 67.5% for the second waveform. The algorithm performed poorly on subject H6 due to the noisy SCG data. Among the 17 other subjects, 15 had higher identification rates for the HS1 waveform as compared to the HS2 waveform. Therefore, in general, the HS1 tends to be easier to identify, this may relate to the stronger intensity of HS1 and its relatively fixed timing of occurrence within a cardiac cycle. In addition, the duration of diastole varies more with respect to heart rate variation, leading to a higher level of variability in the timing of HS2.

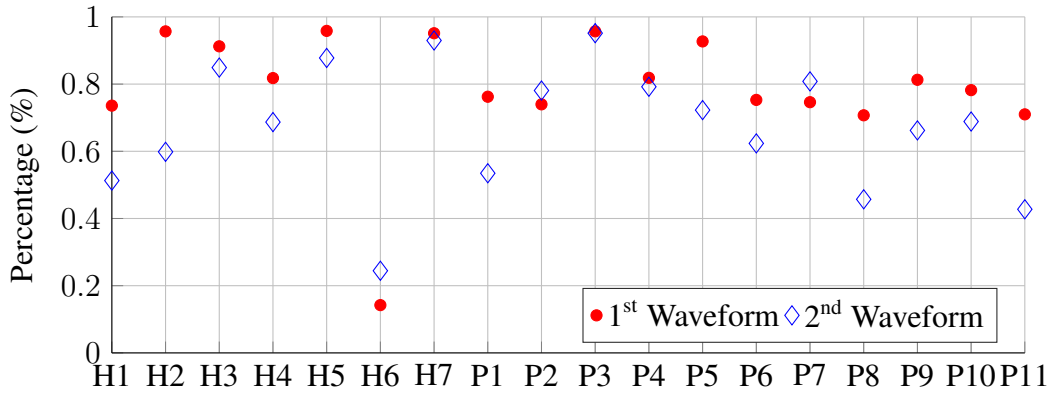

Figure 4.9: Waveform identification rate. H represents healthy subjects and P represents congenital cardiac patients. The subject number corresponds with those in Table 4.1.

In summary, factors that could affect the identification rate are

1. The quality of signal. Noisy signals contain more high-frequency components on top of the true signal making it harder to distinguish the high-frequency waveforms.

2. The morphology of the signal itself. Abnormal morphology appears in signals of cardiac patients, making the identification process difficult.

4.8.2 Phase Error vs. Heart Rate

Depicted in Figure 4.10 are selected scatter plots of the phase error with respect to the actual heart rate from a healthy subject and a cardiac patient, respectively. The associated phase delay functions are cohort-specific.

The healthy subject shown in the left of Figure 4.10 has a higher heart rate and larger heart rate variation than the cardiac patient shown in the right. In both plots in Figure 4.10, ECG phase error decreases linearly as the heart rate increases, indicating that ECG could be a better predictor at higher heart rate. In addition, particularly for the cardiac patients, SCG phase error increases as heart rate increases, further implying that ECG could be a better indicator for high heart rates. Overall, the SCG-predicted phases still demonstrated higher accuracy than ECG-predicted phases, if neglecting the outliers. The systolic and diastolic

SCG-based predictions demonstrated comparable performance as the heart rate changes.

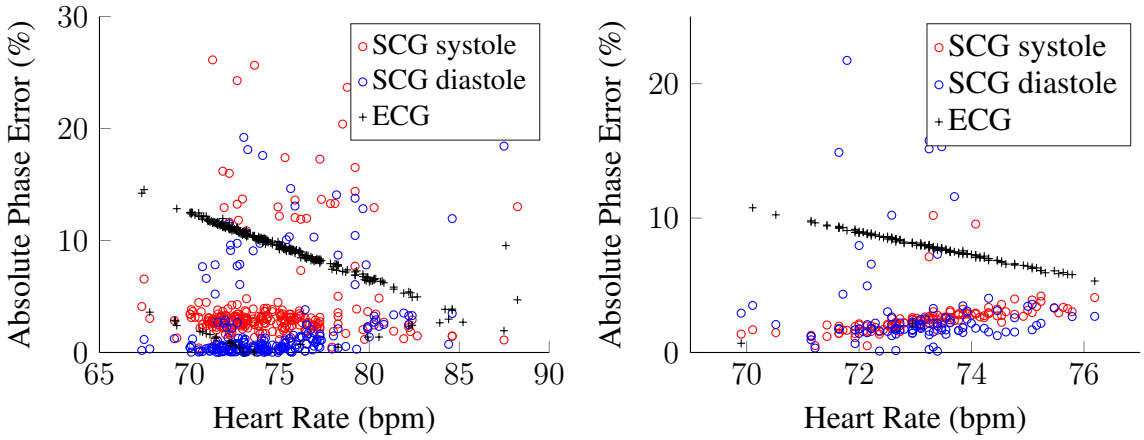

Figure 4.10: Example of the absolute phase error versus heart rate. The left figure corresponds to a healthy subject (subject H4), and the right figure corresponds to a cardiac patient (subject P7). The absolute phase errors were calculated based on the phase delay function within each cohort.

Plots of the average absolute phase error with respect to the average heart rate of all the 18 subjects are shown in Figure 4.11. SCG-prediction was derived using the patient-specific phase delay function on the left and was generated using the cohort-specific phase delay function on the right. The average phase error of SCG-based prediction using the patient-specific approach were generally lower . The systolic SCG-based prediction performs better than that of ECG-based prediction with both patient-specific and cohort-specific approach, while the performance of the diastolic SCG-based prediction was comparable to that of ECG.

4.8.3 Phase Error vs. Heart Rate Error

The phase error is expected to increase as the heart rate error increases. Therefore, intuitively, the expected plot of phase error against heart rate error for a specific subject is supposed to be a V shape centered at zero heart rate error. Note that not all the waveforms associated with heart sounds in SCG were identified successfully, however, the predicted heart rate from each cardiac cycle was mapped to a predicted quiescent phase in the one-

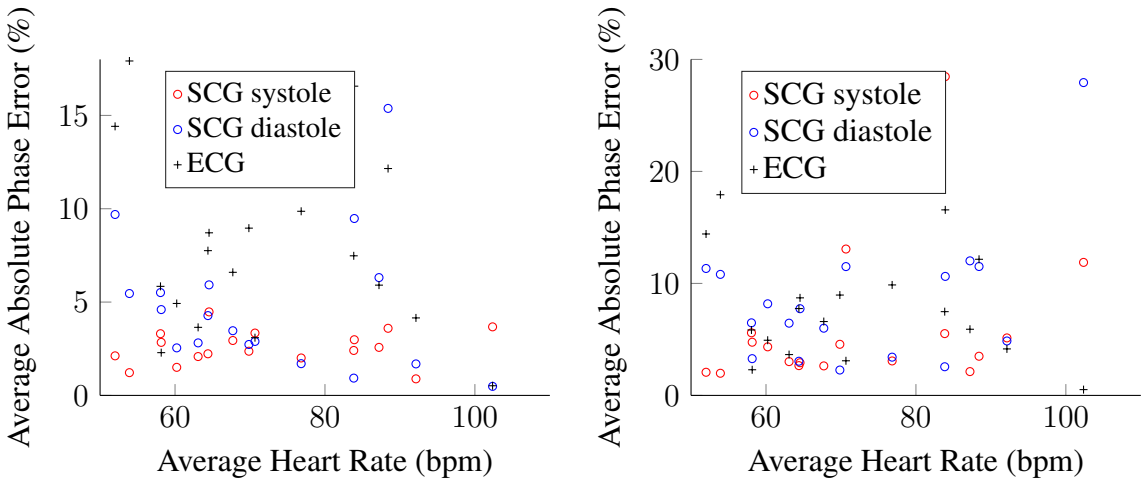

Figure 4.11: Average absolute phase error against average heart rate of all the 18 subjects. The absolute phase errors in the left figure were calculated based on the patient-specific phase delay function, and in the right figure was from each cohort.

to-one ECG gating function discussed in Section 4.4. Therefore, the individual number of scatter samples associated with the systolic and diastolic SCG-based prediction is no more than that of ECG in Figure 4.12. The SCG-based prediction for both subjects in Figure 4.12 similarly exhibit a V-shape. Both figures were generated using the patient-specific phase delay function. The absolute phase error increases as heart rate error increases more significantly when using the ECG-based prediction method as compared to that of the SCG-based prediction method.

Figure 4.13 illustrates plots of the average phase error with respect to the average heart rate error of all the 18 subjects, generated using the patient-specific phase delay function. The average heart rate error was derived from the absolute value of heart rate errors. The HS1 waveform of SCG yielded comparatively better prediction than that of ECG as well as the HS2 waveform. As heart rate error increases, the average phase error becomes much higher by using ECG-based prediction than that of SCG-based prediction.

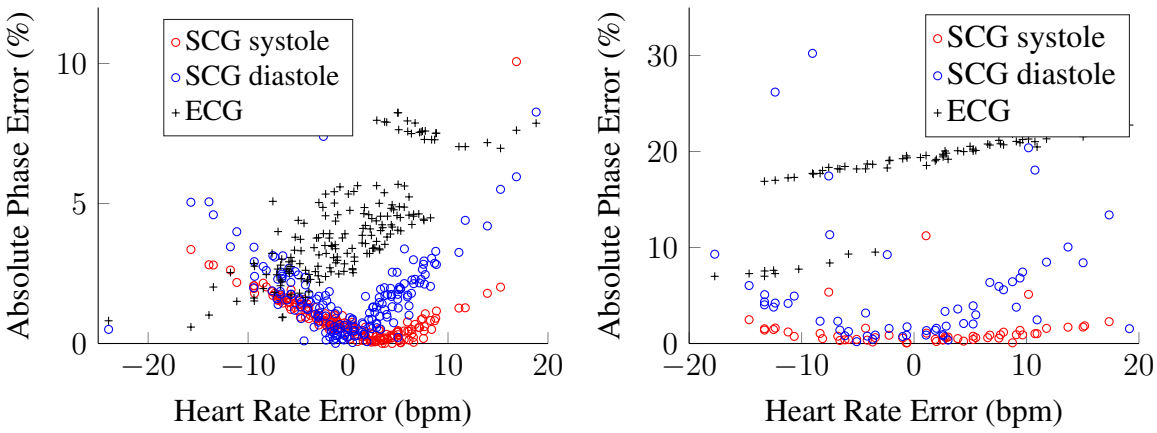

Figure 4.12: Example of the absolute phase error versus heart rate error. The figure on the left corresponds to a healthy subject (subject H7), and the figure on the right corresponds to a cardiac patient (subject P2). The absolute phase errors are calculated based on the patient-specific phase delay function.

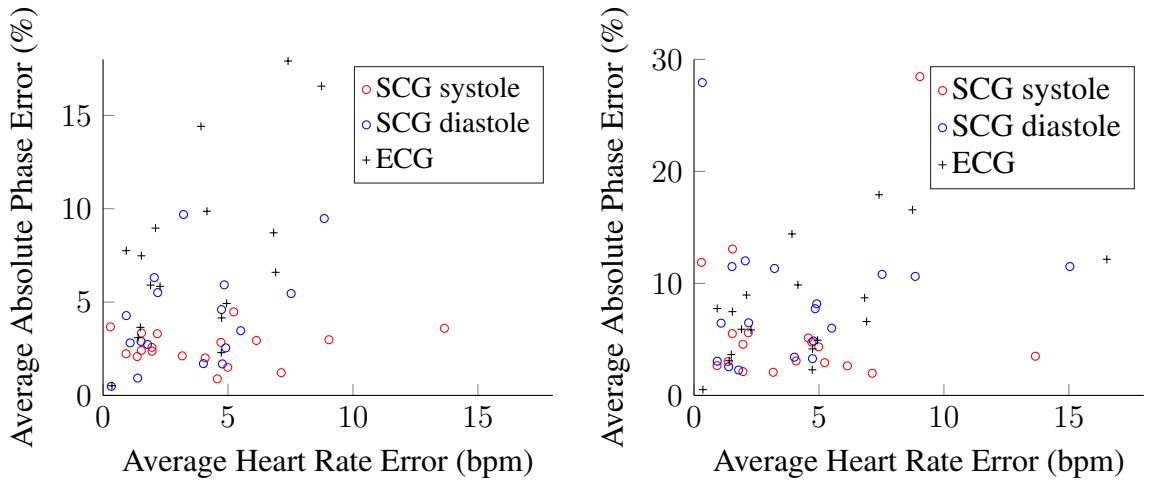

Figure 4.13: The average absolute phase error with respect to the average heart rate error of all the 18 subjects. The absolute phase errors on the left were calculated based on the patient-specific phase delay function, and the right were based on the cohort-specific function.

4.8.4 Average Phase Error vs. Heart Rate Variation

Figure 4.14 shows the impact of heart rate variation on the average prediction error. The plots were generated from results of each individual subject, using the patient-specific and cohort phase delay function, respectively. SCG-based prediction with the patient-specific

phase delay function yielded less phase error. With the cohort-specific phase delay function, the systolic SCG-based prediction predicted more accurately than the ECG-based prediction.

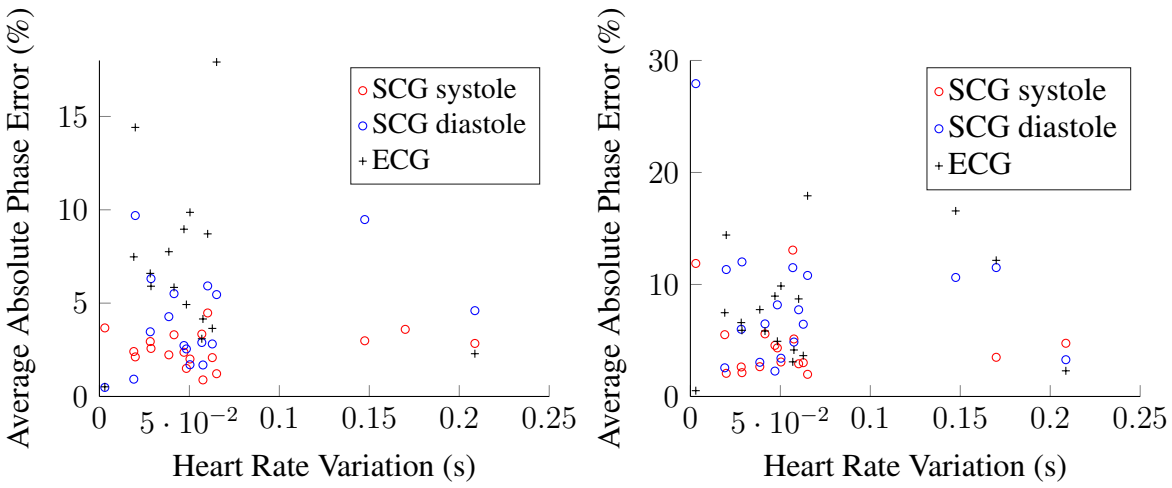

Figure 4.14: The average absolute phase error with respect to the average heart rate variation of all the 18 subjects. The absolute phase errors on the left were calculated based on the patient-specific phase delay function, and the right were based on the cohort-specific function.

4.9 Remarks

This part of the work developed an SCG-based prediction strategy that utilizes the heart sound associated waveform as a more proximal reference to the corresponding quiescence. Compared with the traditional ECG-only-based prediction, the SCG-based method yielded more accurate prediction both in systole and diastole.

However, no formal convention was established about when systolic or diastolic gating should be applied. An empirical but not yet validated conclusion indicates that systolic gating yields better image quality for higher heart rates. However, the predicted phase errors presented in Tables 4.2 and 4.3 did not match such conclusion. Considering echocardiography as the baseline, the velocity magnitude of the deviation measure within a CTA data acquisition window of 83 ms is a legitimate indicator to evaluate the suitability of systolic

or diastolic gating. Based on the observations of the deviation measure in this work, systolic gating did not always relate to less cardiac motion, implying that the heart rate should not be the only factor to consider.

The results demonstrated that SCG in general is an effective predictor of quiescence, however, as the heart rate increases, ECG-based quiescence prediction becomes more effective. Therefore, combining SCG and ECG could potentially lead to an improved cardiac gating of CTA.

A primary limitation of this work is that the hardware data acquisition system provided SCG signals in sub-optimal conditions. The heart sound associated waveforms were heavily distorted by noise, and an important source of the noise was the accelerometric sensor with a low signal-to-noise level. However, the waveform-based prediction method is particularly sensitive to the heart sound morphology. Section 4.2 outlined the waveform identification in which each cardiac cycle is supposed to produce one systolic and one diastolic peak after correlation, indicating the center of the waveform. However, due to the heavily distorted SCG signal, the peaks may not be obvious enough, or occur in an unexpected phase of the cardiac cycle. If an unexpected peak occurs beyond the searching range, it is suitable for prediction and thus will be discarded. In this case, the waveform-based prediction does not provide an optimal output if it fails in locating the waveform, further suggesting the need for fusing ECG and SCG.

Another limitation of this work relates to the heart rate prediction. The prediction is challenged by the heart rate variation. The current prediction method presented in Section 4.8 may be improved for tracing the actual heart rate more accurately when confronting large heart rate variation. Advanced prediction methods such as the autoregressive integrated moving average (ARIMA), general regression neural network (GRNN) and support vector regression (SVR) can be explored.

CHAPTER 5

FUSION-BASED QUIESCENCE PREDICTION

The SCG-based prediction was demonstrated to be effective in improving the quiescence prediction as compared to the traditional approach, the ECG-based prediction, indicating that SCG can potentially replace or supplement ECG to trigger cardiac gating. To date, ECG is still a predominant technique for diagnosing cardiac-related conditions [80, 81]. The R-peaks of ECG are straightforward and robust markers to segment the heartbeats. Although some explored segmenting heartbeats using cardiac features in the SCG signals [82, 83], no universally acknowledged approaches were developed thus far. Therefore, replacing ECG with SCG for general diagnostic purposes is not yet feasible; however, using SCG to supplement ECG for quiescence prediction is more reasonable to investigate.

While SCG deliberately captures the mechanical cardiac movement, the accelerometric sensor is highly sensitive to any motion, not only to the cardiac motion but also body movement and external environmental interference. This compromises the accuracy of the quiescence prediction since the SCG-based prediction method is waveform-dependent. Therefore, it is important that the subject is well-rested during the CTA exam. In the case when SCG-based prediction fails due to the excessive noisy waveforms, the ECG-based prediction can be employed. Therefore, a fusion-based prediction[1] that intelligently makes use of both ECG and SCG for cardiac gating is introduced.

A schematic diagram that demonstrates the fusion-based, or weighted fusion (WF), based prediction is shown in Figure 5.1. The fusion-based prediction was implemented replying on an artificial neural network (ANN). Each component in the diagram will be elaborated individually in the following sections.

[1] In this work, the terms "weighted fusion (WF)" and "fusion-based prediction" are used interchangeably for the purpose of simplicity in some circumstances.

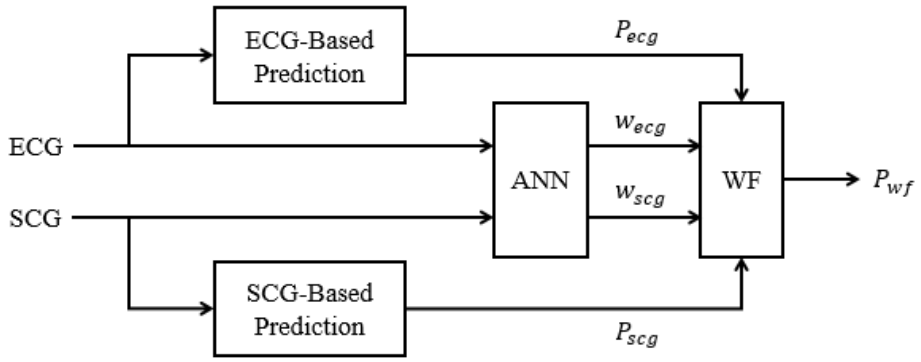

Figure 5.1: The schematic diagram that demonstrates the fusion-based prediction. P_{ecg} and P_{scg} are predictions from the ECG- and SCG-based methods, respectively. w_{ecg} and w_{scg} are weights of ECG- and SCG-based predictions, generated from the ANN.

5.1 Overview of the Multimodal Framework

The fusion-based prediction is an essential part of the comprehensive multimodal framework for quiescence prediction. The multimodal framework is an extension of fusion-based prediction by encompassing special cases of the fusion-based prediction, and the cases when the fusion-based prediction is not the optimal method. The multimodal framework can be outlined with simplified block diagrams shown in Figure 5.2. The framework incorporates three modules. Module 0 is making a pre-defined ANN by training on data from a cohort of subjects. The ANN can be pre-defined prior to the pre-test. The details of pre-defining the ANN parameters is elaborated in Section 5.4. Module 1 is conducting the 3-minute pre-test in which synchronized ECG and SCG data are recorded. The pre-test is dedicated to generating the personalized heart sound associated template and to pre-categorize a subject based on the SCG index[2]. The pre-categorization decides to apply the ECG-based prediction or the fusion-based prediction during the actual CTA exam, leading to two options in module 2 where the real-time data is processed for CTA gating. The pre-test and pre-categorization are discussed in Section 5.6.

[2]The SCG index threshold, -120, was selected empirically. As the population in the cohort increases, the selected threshold may vary but will get closer to its actual empirical value with a higher confidence level.

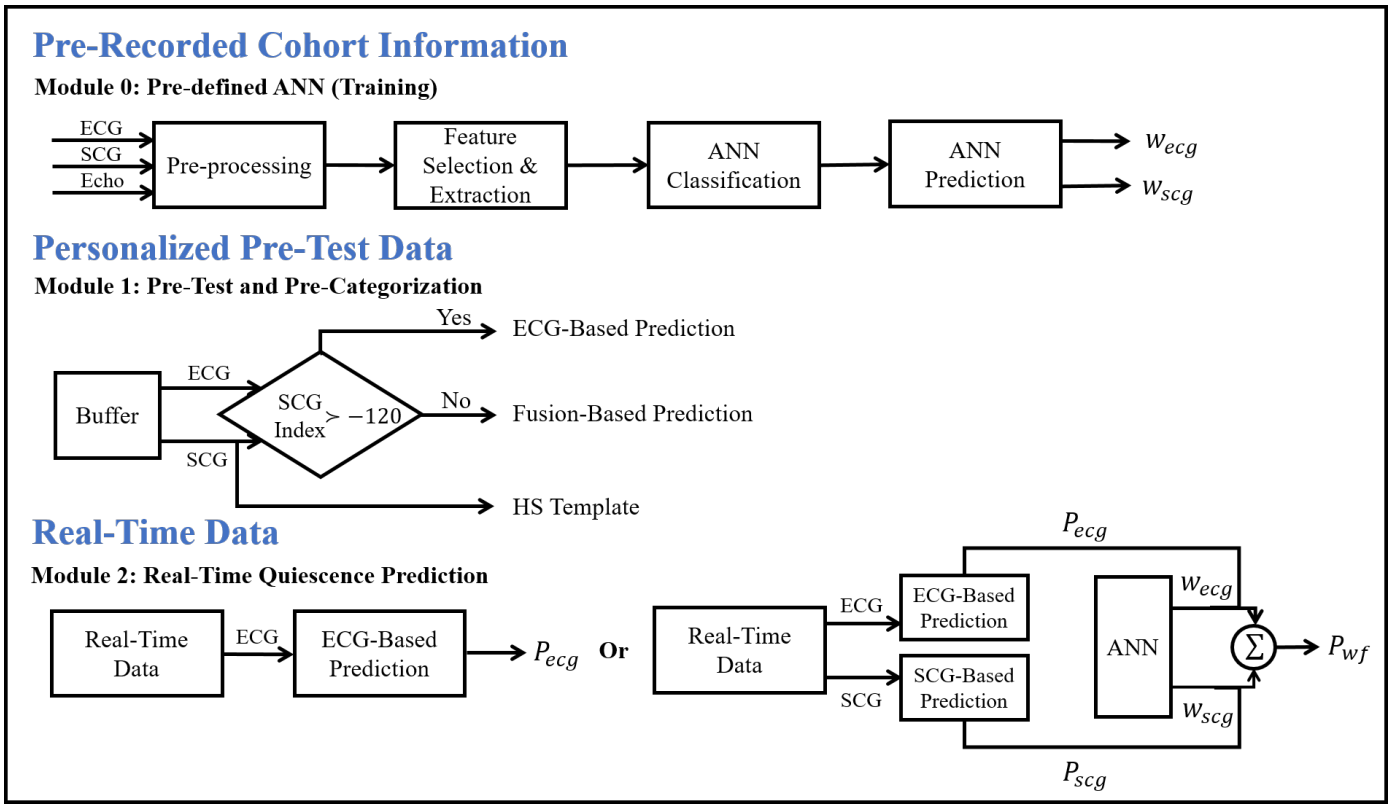

Figure 5.2: Schematic diagrams outlining the comprehensive multimodal framework.

5.2 Artificial Neural Network Configuration

The ANN is a machine learning tool inspired by biological neural network structures of the animal brain [84, 85]. ANNs utilize computer programs to simulate the way that the brain processes the information, thereby recognizing complex patterns that can be learned by a machine.

Fundamental elements that consists an ANN include an input layer, one or more hidden layers, an output layer, and neurons. Neurons, or nodes, within a layer change their states with different inputs and produce outputs based on the activation. Neurons are interconnected between layers. Each neuron from the hidden layer(s) and output layer is a weighted transformation of the neurons from the previous layer. The hidden layer imposes transformation on neurons whereby weights and bias are assigned to groups of neurons and their linear combination is passed through an activation function as the input to the next

layer. The values of weights and bias are initially randomly assigned and can be updated in a back propagated manner until the final output of the ANN best matches the desired outcome. A simple two-layer ANN structure is presented in Figure 5.3.

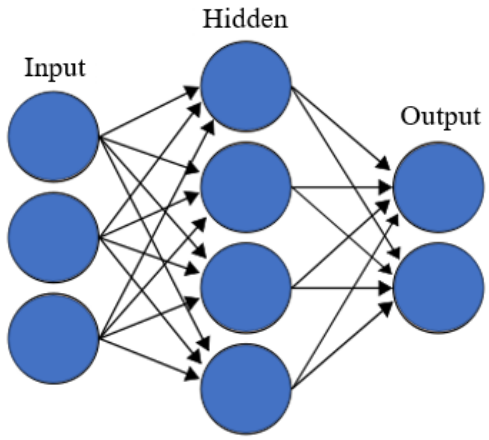

Figure 5.3: A two-layer ANN structure with an input layer (3 neurons), one hidden layer (4 neurons) and an output layer (2 neurons).

ANNs have multiple merits. Studies have demonstrated the competence of ANNs in capturing associations among vaguely understood variables [86] without imposing constraints upon the input data structure [87]. In addition, ANNs are efficient in dealing with real-time signal detection and classification, as well as with transient signals with low signal-to-noise ratio [88]. The training of ANN models may be time consuming, but once the training/learning process is completed, the model parameters will be saved for prediction, making the ANNs more time-efficient than algorithms such as the k-Nearest Neighbor and Support Vector Machine. ANNs also do not have constraints upon the input data structure, while Linear Discrimination Analysis and Quadratic Discriminant Analysis assume the conditional distribution is multivariate Gaussian [87]. In terms of prediction, an ANN outputs not only a classification decision but also Bayesian probability estimates, which can potentially serve as the relative weighting between SCG and ECG parameters in the multimodal framework.

To date, machine learning, especially classification algorithms such as ANNs, has been widely applied to solve biomedical-related problems such as identification of arrhythmias

from ECG [89] and screening sleep apnea from polysomnography [90]. Because the ANNs are especially useful in approximating nonlinear functions and dealing with a large number of inputs that are generally unknown [91, 92], ANNs have been applied extensively to classifying physiological signals [92, 93]. One example is the development of an automated generic classifier for detecting physiological signals whose type are unknown [93]. More examples can be found in a review on ANN for processing and classifying multiple biomedical signals [92].

With regard to cardiac gating, prior research focused mainly on quiescence prediction that relies exclusively on either ECG or SCG [8, 42], resulting in a limited background literature to refer to. In this work, fusion-based prediction was implemented using a predefined three-layer artificial neural network (ANN) whose output, Bayesian probability estimates, served as the assigned weights, w_{ecg} and w_{scg}, for fusing individual predictions from ECG and SCG. The weights can be interpreted as the likelihood that a specific cardiac cycle to be optimally gated using one modality, either ECG or SCG. Gating with solely ECG or SCG are special cases of weighted fusion where one of the weights takes the value of 0 and the other takes 1. Let P_{ecg} and P_{scg} be quiescence predicted from ECG- and SCG-based method, respectively, the ultimate fusion-based prediction is a linear combination of the individual predictions from the ECG and SCG and can be expressed as $P_{wf} = P_{ecg}w_{ecg} + P_{scg}w_{scg}$ where $w_{ecg} + w_{scg} = 1$.

The input to the ANN is a set of personalized features extracted from the ECG and SCG signals and will be elaborated in Section 5.3. In summary, the selected features include heart rate, heart rate variability [94], waveform correlation [95], heart sound (HS) associated waveform power intensity [96] and wavelet-based time-frequency coefficients [97, 98].

The specific configuration of the ANN applied to this work was obtained based on a few rational principles. A two-layer ANN is able to represent any arbitrary continuous function, and an ANN with greater than two layers is able to represent any function [99]. Thus, a

three-layer ANN configuration is an appropriate choice for this study in which the associated data structure is unknown. Figure 5.4 illustrates the feedforward ANN configuration used in this study. The ANN consists of three layers: two hidden layers with hyperbolic tangent-sigmoid and log-sigmoid as activation functions [100], respectively, and an output layer with softmax activation function [101]. The number of neurons in each layer was set heuristically. The network was trained with scaled conjugate gradient back-propagation [102]. The back-propagation feeds the error term back through the layers, by updating the weights at each node. The number of nodes in each layer was determined by using the trial-and-error method.

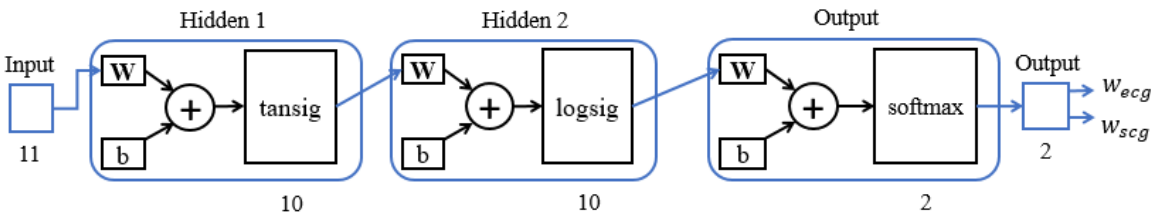

Figure 5.4: The three-layer ANN configuration [101]. The input is a set of features consisting of 11 single-valued entries linked with two hidden layers with activation functions tansig and logsig, each consisting of 10 neurons. $[\mathbf{W}, b]$ are configuration parameters representing the weights and bias. Two softmax output neurons in the output layer generate two values corresponding to the predicted probabilities, referred to as weights, of ECG- and SCG-based gating in the weighted-fusion (WF).

Similarly, the selection of two activation functions followed an intuitive logic. The activation functions were first heuristically chosen among a few commonly used activation functions. Then the trial and error method of multiple different combination of activation functions enabled discovery of the optimal pair that yielded the highest classification accuracy.

Typically, the activation functions can be categorized into linear and non-linear types as shown in Figure 5.5. Piecewise linear functions such as rectified linear unit (ReLU) function and pure linear function do not confine the output of the function within a closed and bounded domain. Additionally, linear functions fail in adapting with the complexity and nonlinearity of input data. Therefore, linear activation functions are not suitable for

this work.

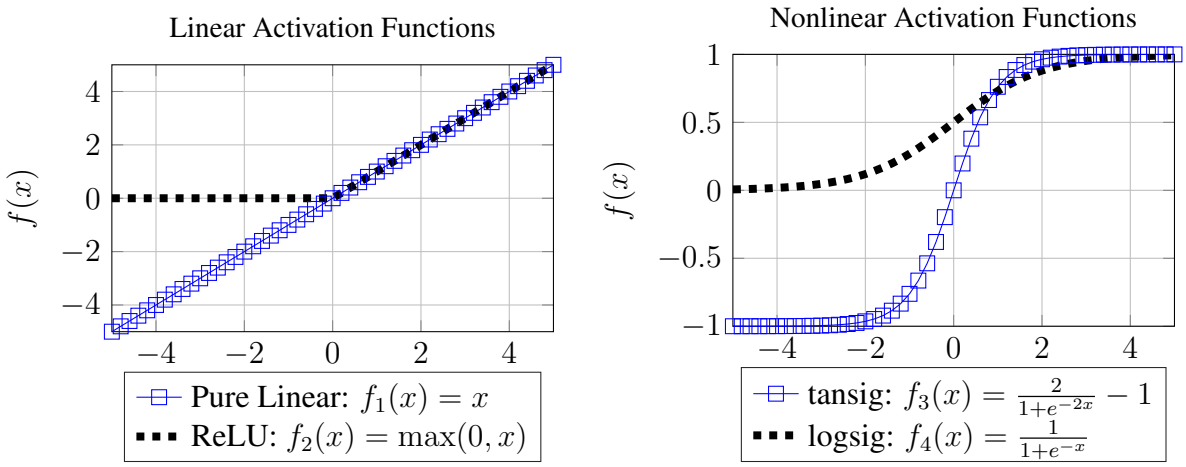

Figure 5.5: Examples of linear and non-linear activation functions.

The commonly used non-linear functions for artificial neural networks are hyperbolic tangent (also known as tanh) and sigmoid (also known as logistic) functions. Hyperbolic tangent function ranges from -1 to 1, hence, it is zero centered, making the gradient update faster and easier. The sigmoid function restricts any input value within 0 and 1 which is especially helpful for models that predicts the probability as an output. Therefore, this work chose to use the hyperbolic tangent sigmoid activation function (tansig) for the first hidden layer and log-sigmoid (logsig) for the second hidden layer.

5.3 Feature Selection and Extraction

This part of the work prepares the input to the ANN, wherein a few sequential procedures are involved. The procedures are embodied in the block diagram in Figure 5.6.

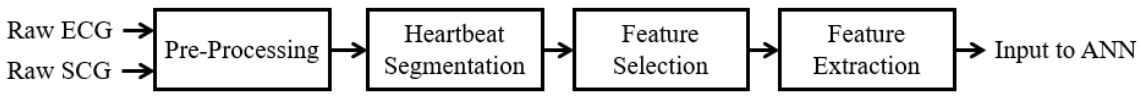

Figure 5.6: Block diagram of signal processing procedures to obtain input for the ANN.

Synchronized ECG, SCG and sessions of echocardiography signals were acquired and the raw signals were pre-processed to remove the noise and artifacts. Details about data

acquisition and pre-processing were delineated in Chapter 3. After pre-processing, signals were segmented into individual cardiac cycles and each cardiac cycle was re-sampled into 1000 sample length for computational simplicity. Quiescence prediction for cardiac gating is required on a beat-by-beat basis, therefore, subject-specific features were extracted on a beat-by-beat basis.

The rationale for selecting ANN features is three-fold. First, the feature set should contain as much information of the original dataset as possible. Second, the features are expected to be invariant to irrelevant transformations of the data. Third, features are expected to be distinguishing. More specifically, a new feature is only worth adding when it serves to increase information in the current feature set.

Feature selection involves two stages. The first stage is constructing an original feature set that contains a broad coverage of features. The original features and their corresponding number are summarized in Table 5.1. These features were selected based on published research demonstrating their effectiveness in representing cardiac information in ECG and SCG signals. This is not intended to be an exhaustive or optimized list of features.

Table 5.1: Original Features

Original ECG Features					Original SCG Features				Total
HR	*HRV*	SNR_{ecg}	C_{ecg}	DWT_{ecg}	PSD_{output}	PSD_{HS1}	PSD_{HS2}	DWT_{scg}	
1	1	1	1	4	1	1	1	3	14

The 8 ECG features in the original feature set are elaborated below:

1. *HR*: Heart rate. Reciprocal of the interval between two consecutive R-peaks. Measured in beat per minute (bpm).

2. *HRV*: Heart rate variability [94, 103]. Defined as the deviation to the mean of the most recent eight R-R intervals with respect to a specific cardiac cycle. The deviation was measured by the absolute difference [104]. The first eight cardiac cycles are for initialization.

3. SNR_{ecg}: Signal-to-noise ratio. An ensemble template was obtained by averaging the re-sampled cardiac cycles. The difference between the ensemble template and an individual re-sampled cardiac cycle was the difference time-series whose magnitude indicate the signal distortion due to noise. The root-mean-square (RMS) power of the difference time-series quantitatively measures the relative noise power with respect to an individual cardiac cycle. The estimated signal-to-noise ratio is the ratio of template waveform power (summation of squared sample values) to the noise power with respect to an individual cardiac cycle.

4. C_{ecg}: Waveform correlation [95, 105]. The correlation between an individual cardiac cycle and the aforementioned ensemble template as an evaluation of the morphological distortion level due to noise and artifacts.

5. DWT_{ecg}: Discrete wavelet transform (DWT) coefficients [97, 106, 107]. For ECG, Daubechies four (Db4) was tested to be a suitable mother wavelet and a decomposition level of 8 was found to be suitable [106, 108]. Four wavelet scales (5-8) were used, corresponding to the frequency band spanning approximately 2-20 Hz. The mean coefficient of each scale was then used as the original features.

The 6 SCG features in the original feature set are elaborated below:

1. $\{PSD_{output}, PSD_{HS1}, PSD_{HS2}\}$: Heart sound waveform intensity [96]. The power spectrum based on discrete Fourier transform within three frequency ranges: 0-10 Hz that relates to the cardiac output, 10-30 Hz that relates to the first heart sound (HS1), and 30-50 Hz that relates to the second heart sound (HS2) [70, 109, 110]. Periodogram estimates the power spectrum density of the time-series cardiac signal by squaring the magnitude components of the discrete Fourier transform of the signal. The aggregate power within each 10 Hz bin was calculated by summing the power within the aforementioned three spectrum ranges providing a periodogram estimate of the PSD.

2. DWT_{scg}: Discrete wavelet transform (DWT) coefficients. Previous work demonstrated the superiority of "Coif5" mother wavelet in decomposing the heart sound related signals [70]. Similar to ECG, a decomposition level of 8 was applied to SCG. Three wavelet scales (4-6) were used, corresponding to the frequency band spanning approximately 10-45 Hz. The mean coefficient of each scale was then used as the original features.

Compared to the classic discrete Fourier transform (DFT), the wavelet-based time-frequency decomposition, DWT, is a more advanced technique in analyzing the temporal resolution of a signal. The mother wavelet was selected based on the similarity in waveforms. Visualizations of the mother wavelets of ECG and SCG signals are presented in Figure 5.7. In addition to the frequency information, the DWT also captures local temporal information. The various option and scales of dilation of the mother wavelet enables the DWT to localize the time-frequency relation within a signal at a finer level. To ensure that the wavelet coefficients are free from boundary effects, the decomposition level was chosen to be no greater than $\log_2(L)$ for a signal of length L.

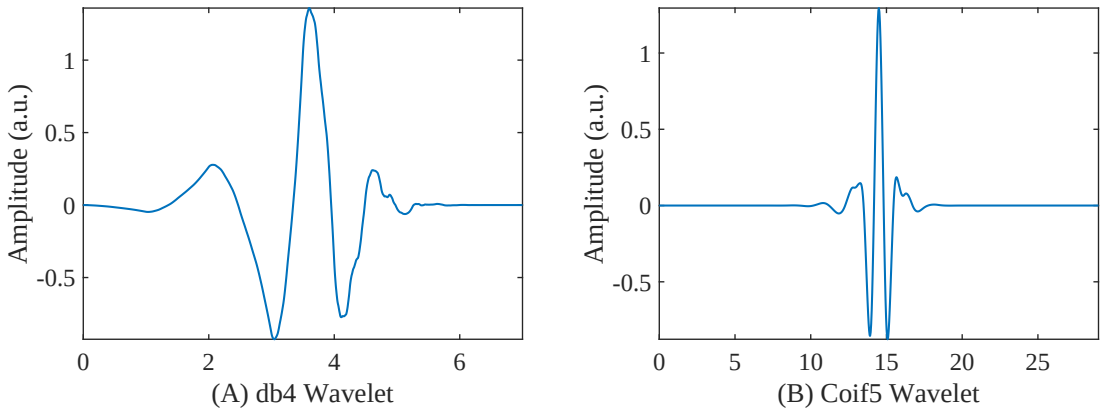

Figure 5.7: Mother wavelets (A) "db4" for ECG signal and (B) "Coif5" SCG signal.

To reduce the number of features as input to the ANN, only the DWT coefficients corresponding to the frequency range of interest were taken. Based on the Fourier transform analysis of the human ECG signal, it was found that the QRS complex frequency ranges

within 4 Hz and 20 Hz, the heart rate component is within 0.67 Hz and 5 Hz (corresponds to 40-300 bpm) and the P and T wave frequencies generally lie between 0.5 and 10 Hz [68]. Therefore, for the ECG signal, the wavelet decomposition coefficients corresponding to the frequency span of 2-20 Hz were used. Similarly, the wavelet decomposition of SCG within 10 Hz and 45 Hz were intended to make use of the information from the high frequency accelerometric waveforms associated with the first (10-30 Hz) and second heart sound (30-45 Hz). Thus, for the SCG signal, the wavelet decomposition coefficients corresponding to the frequency span of 10-45 Hz were used. The time-frequency visualization of continuous wavelet decomposition of ECG and SCG signals are illustrated in Figure 5.8.

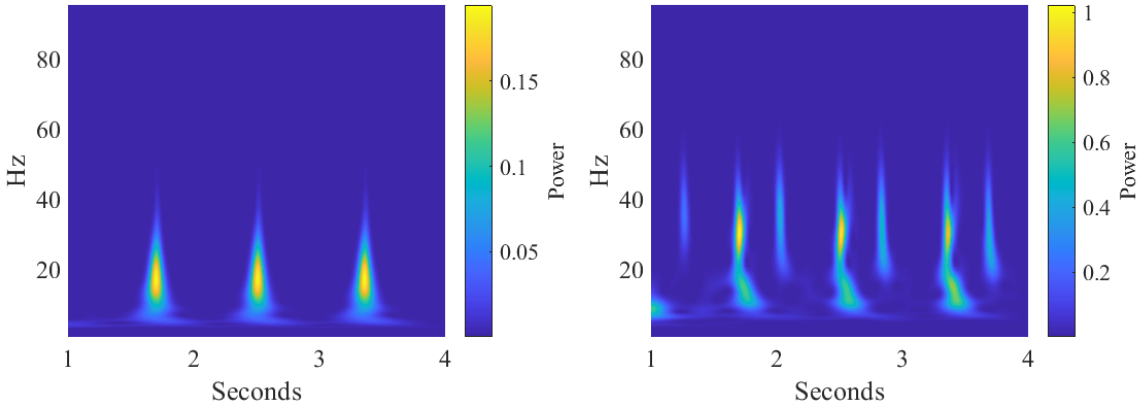

Figure 5.8: Time-frequency presentation derived from wavelet decomposition of (A) ECG signal and (B) SCG signal.

The ANN is sensitive to skewed values of features, e.g., extremely large or small values as the input. Heavily noisy cardiac cycles can potentially yield skewed features. To avoid deadlock in ANN processing, it is necessary to identify those cardiac cycles that may not be good candidates for feature selection. Therefore, each individual cardiac cycle is evaluated on its ECG waveform and its SCG HS waveform before feature selection. The criteria for selecting the good candidate cardiac cycles are as follows:

1. Cardiac cycles with $C_{ecg} < 0.3$ and HS not identified by the waveform template detection approach [38] are considered to be severely contaminated by noise, and thus are eliminated. No quiescence prediction is made for this cardiac cycle.

2. Cardiac cycles with $C_{ecg} > 0.3$ but with no HS identified are suitable for ECG-based prediction, indicating that $P_{scg} = 0$ and thus $P_{wf} = P_{ecg}w_{ecg}$.

3. Cardiac cycles with HS identified but $C_{ecg} < 0.3$ are suitable for SCG-based prediction, indicating that $P_{ecg} = 0$ and thus $P_{wf} = P_{scg}w_{scg}$.

4. Only those cardiac cycles whose ECG and SCG waveforms are clean enough are valid for fusion-based prediction by the ANN, indicating that $P_{ecg} \neq 0$ and $P_{scg} \neq 0$ and $P_{wf} = P_{ecg}w_{ecg} + P_{scg}w_{scg}$.

The threshold criterion is set based on empirical statistics of C_{ecg}. Cases 2 and 3 are special cases of 4, the fusion-based prediction. On average, 72% of the cardiac cycles were good candidates for feature selection.

The second stage of feature selection picks a subset of the original features to form a more select and computationally efficient feature set. The 14 single-value original features can be narrowed down by identifying the relative importance of each feature and constructing a more select feature set by discarding the less significant features. To this end, the neighborhood component analysis (NCA) [111] with regularization was applied to the original feature set. NCA is a non-parametric and embedded method that selects features with the goal of maximizing prediction accuracy of classification. The embedded method is one of the three typical feature selection algorithms, the other two are the filter method and wrapper method. The embedded method ranks the contribution of features in the process of creating the model. Regularization introduces additional constraints to improve the leave-one-out classification accuracy [112], which then generates an optimized feature weighting. The average weight of each original feature is presented in Figure 5.9 where the 3 features with the lowest weights, the DWT of ECG at level 5 and 8 as well as DWT of SCG at level 5, were discarded.

A select feature set of 11 single-value features was then created, consisting of 6 features from the ECG and 5 features from the SCG. Table 5.2 presents a listing of the select

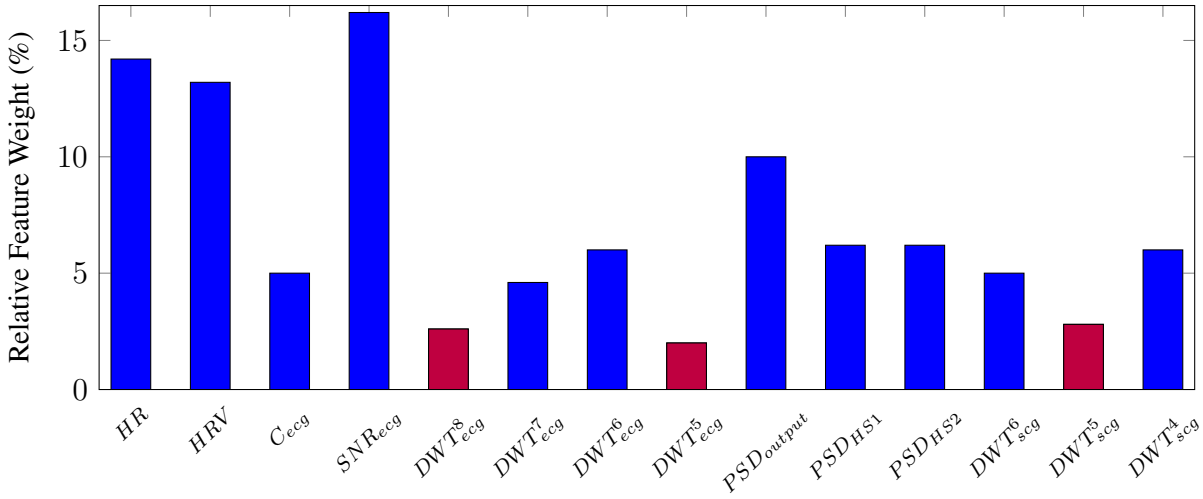

Figure 5.9: Relative feature weight (%) evaluated by the neighborhood component analysis. Features in purple bars demonstrated less importance in distinguishing ECG and SCG signals and consequently were discarded.

features. The number of 11 features may still seem large and an even more selective feature set with 4 features are presented in Chapter 6. Other related work used various number of features from ranging from 3 to 15, or ever larger [113, 114]. Many of these works only investigated one signal while this work involves two cardiac signals, thus, naturally, a larger number of features may be needed to present cardiac information of both signals. As an additional note, this work is not intended to be an exhaustive or optimized list of features.

Table 5.2: Select Features

Select ECG Features					Select SCG Features				Total
HR	HRV	SNR_{ecg}	C_{ecg}	DWT_{ecg}	PSD_{output}	PSD_{HS1}	PSD_{HS2}	DWT_{scg}	
1	1	1	1	2	1	1	1	2	11

The feature selection is followed by the feature extraction, wherein a new set of features was constructed based on the existing features in the select feature set. Feature extraction is an irreversible transformation to reduce the dimensionality of the feature set. The principal component analysis (PCA) was applied where eigenvalues less than 20% of the largest eigenvalue were discarded. Features were then normalized by calculating their Z-scores [115, 116] to eliminate the bias of mean and variance before inputting into the ANN. Note

that PCA uses an orthogonal transformation to convert the set of possibly correlated features into a set of linearly uncorrelated features. While the dimension of the feature set is reduced upon mapping to the principal axes, the number of features that comprises the feature set remain the same.

5.4 Training, Testing and Cross-Validation

To validate the proposed fusion-based prediction method, training and testing of the ANN were carried out on a set of data acquired from seven healthy subjects (mean age: 31; age range: 22-48; female/male: 3/4) and eleven cardiac patients (mean age: 56; age range: 31-78; female/male: 5/6). Hence, two cohort of subjects were formed, one consisting of all healthy subjects and the other consisting of all cardiac patients.

Training and testing were carried out in a leave-one-out manner. The *testing* dataset was formed by the designated subject's cardiac data. The corresponding *training* dataset was formed using cardiac data from the rest of participants who belong to the same cohort. To avoid over-training by the excessive number of cardiac cycles contributed by the rest of participants in the cohort, a subset of size four times of that of the testing dataset was blindly selected. On average, the evaluation for each subject involves 6336 cardiac cycles for training and 1584 cardiac cycles for testing.

The ECG-based prediction was obtained from a pre-defined piece-wise gating function [28] described in Chapter 2.1.1. This gating function maps a predicted heart rate to an one-on-one quiescent phase. According to Equation 4.6, for heart rate greater than 83 bpm, a systolic quiescent phase is assigned for CTA data acquisition, and heart rate no greater than 83 bpm is assigned with diastolic quiescent phase. To make it a fair comparison between the ECG- and fusion-based prediction, quiescent predictions from the same cardiac period, either systolic period or diastolic period, are compared.

The predicted heart rate was obtained from a linear regression formed by using the previous six heart beats. SCG-based prediction was obtained using the patient-specific HS

waveform detection method elaborated in Chapter 4.

The ANN binary classifier categorizes an input feature into two groups, labeled as "ECG" and "SCG". Labels in the testing dataset were obtained by comparing the ECG- and SCG-based predictions with the quiescence derived from the baseline subject-specific echocardiography, respectively. The modality that led to a smaller prediction error was considered to be an optimal modality for a particular cardiac cycle, and thus this modality was assigned as the label for that cardiac cycle. The prediction error, in milliseconds, was calculated as the absolute difference between the predicted quiescent timing and the baseline subject-specific echocardiography.

The properties of training and testing datasets are different. The feature values in the training dataset are deterministic, while the testing dataset contains predicted values as features. More specifically, in contrast to the training dataset, features $\{HR, HRV\}$ from the testing dataset were unknown since the upcoming cardiac cycle of this particular subject is unknown. As mentioned earlier, the upcoming instantaneous heart rate was predicted using a linear regression method with previous six heartbeats [38]. The instantaneous heart rate variability was the deviation of the predicted instantaneous heart rate from the mean of the most recent eight heart rates [104].

The training dataset was further divided into four uniform parts randomly, one of which was used for cross-validation [75]. This 4-fold cross-validation was repeated 10 times with random partition of the training dataset to make the whole process as 10x4-fold cross-validation. The output from ANN, including classification accuracy and modality probability, were the average results over the 10 iterations.

5.5 Results

The performance of the multimodal framework was evaluated from multiple aspects. The ANN prediction accuracy and precision reflect the effectiveness of the constructed ANN in binary classification. By combining the individual predictions from ECG and SCG, the

ANN produces a fused prediction. The quiescence prediction error was then calculated as the deviation of the fused prediction from the quiescence derived from the subject-specific baseline echocardiography. Lastly, the diagnostic quality of the CTA images reconstructed at the phases derived from ECG-, SCG- and fusion-based methods were evaluated and compared.

As mentioned in Section 5.2, one of the merits of ANN is its output of both prediction and classification functions. In this work, the output from the softmax function in the output layer are two entries within the range of 0 and 1, and the two entries add up to 1. In probability theory, the output of the softmax function can be considered as a categorical distribution, namely, a probability distribution over different possible outcomes. Classification is made based on the probability of each category, e.g., ECG or SCG, as compared to a specified threshold. The ANN classification performance, accuracy and precision, is presented in Section 5.5.1.

The fusion-based method utilizes the probability output from the ANN as weights of the linear combination of individual predictions from the ECG and SCG. The quiescence prediction error presented in this section was measured in time, e.g., seconds or milliseconds. As mentioned in Chapter 5.5, while the cardiac phase, normalized over a cardiac cycle for HRV, is effective in mathematical modeling, it is essentially the temporal error that results in the degradation of the cardiac CTA image quality. On the other hand, the error in phase neglects the sensitivity to mistiming that varies among individuals and the predicted heart rate. The quiescence prediction performance, prediction error and variation, is presented in Section 5.5.2.

5.5.1 Artificial Neural Network Classification Accuracy

The decision-making of the ANN binary classification was made by comparing the categorical probability with a threshold. Theoretically, a correct ANN binary classification leads to a value close to 1 for the weight associated with the correct category and close to 0

for the other category. A typical threshold is 0.5 (corresponds to 50% in probability) when each category hold similar percentage. The results from Chapter 4 indicate that the SCG-based prediction is more accurate for the majority of cycles, thus, the SCG is the dominant category in classification. In this case, a biased threshold is set based on the proportion of different categories over the total number of categorized predictions. More specifically, the accuracy for testing/prediction was set according to the subject-specific data in the training dataset: $T_{ecg} = N_{ecg}/N$ and $T_{scg} = N_{scg}/N$, where $N = N_{ecg} + N_{scg}$ is the total number of ECG-labeled (N_{ecg}) and SCG-labeled (N_{scg}) cycles. By comparing the ANN output, w_{ecg} and w_{scg}, with T_{ecg} and T_{scg}, respectively, classified/predicted labels were decided.

The ANN prediction accuracy and precision are listed in Table 5.3, in order of increasing heart rate, within each cohort. Subjects H1 to H7 are from the cohort of healthy subjects and P1 to P11 are from the cohort of cardiac patients. The classification accuracy is the percentage of correct labels being identified, and precision is the percentage of correctly predicted SCG-labeled cycles against the total number of cycles predicted as SCG-labeled cycles.

The average accuracy of the ANN is 89.9% for the healthy cohort and 80.6% for cardiac patients. The average precision of the ANN is 93.5% for the healthy cohort and 83.8% for cardiac patients. These values indicate that the selected features are fair representatives of the cardiac information from acquired signals. However, there is room for improving the classification performance. Several factors may affect the classification performance:

1. Acquired data: Outliers in the data may cause overlapping patterns. The training dataset is expected to have adequate number of instances for an effective learning for the ANN.

2. Selected features: The presence of irrelevant features or an inadequate number of effective features.

3. Classification algorithm: In general, this factor does not significantly impact the clas-

Table 5.3: Three-Layer ANN Binary Classification

Healthy Subjects				
Subject	HR (bpm)	HRV (ms)	Accuracy (%)	Precision (%)
H1	58	41	90.1	95.4
H2	60	48	89.4	92.7
H3	68	28	90.4	93.8
H4	73	50	92.2	94.7
H5	77	50	87.1	91.0
H6	84	19	90.2	93.7
H7	92	58	89.9	92.9
Mean	72	42	89.9	93.5
Cardiac Patients				
P1	52	20	80.6	82.8
P2	54	65	80.7	83.5
P3	54	208	77.3	81.3
P4	63	63	80.7	83.1
P5	64	38	81.3	84.1
P6	65	60	82.8	84.1
P7	73	57	83.3	86.5
P8	81	170	79.5	84.3
P9	84	147	81.3	85.8
P10	87	29	78.8	82.7
P11	102	3	79.9	83.3
Mean	70	78	80.6	83.8

sification accuracy when the dataset is large and the selected features for classification are salient representatives of the cardiac information of the raw signal. In this case, other classification algorithms are very likely to give similar results as the ANN in this study [75].

5.5.2 Quiescence Prediction Errors

Figure 5.10 reveals the individual average prediction error (in milliseconds) from the testing dataset. The optimal quiescent prediction method, either ECG, SCG or WF, was selected based on the least error (ms). The overall prediction error associated with ECG-, SCG- and WF-based method over all subjects are 76.15 ms, 48.30 ms and 43.95 ms, respectively. Out of the 18 subjects, only one subject (P2) would actually benefit from using ECG-based gating solely. It is also observed that subjects H3 and H4 are potential candidates for ECG-

based prediction, but fusion-based prediction works as well for them.

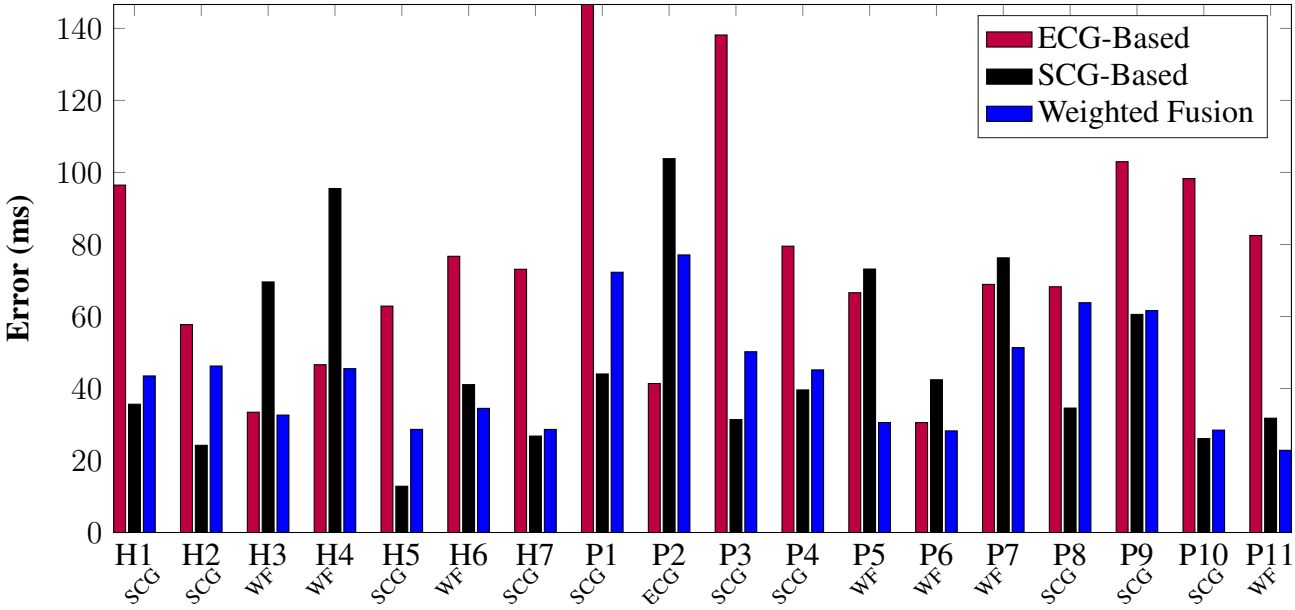

Figure 5.10: Quiescence prediction error (milliseconds) derived from different quiescent prediction methods. The overall prediction error associated with ECG-, SCG- and WF-based method over all subjects are 76.15 ms, 48.30 ms and 43.95 ms, respectively.

Figure 5.11 reports the quiescence prediction error derived from ECG-, SCG- and fusion-based method. The median of the three groups of prediction error are 71.01 ms, 40.34 ms and 44.32 ms. WF- and SCG-based prediction elicited comparable low errors than that from ECG, but WF caused less variability among the three methods.

Although the absolute prediction improvement in milliseconds by using WF- or SCG-based prediction may not seem very prominent for all individuals, it is noticeable that for some subjects whose ECG-based predictions yielded large prediction errors, such as patients P3 and P11, the SCG- and WF-based predictions were able to reduce the error significantly. For such subjects, SCG- or WF-based quiescent prediction could potentially lead to saliently improved diagnostic quality.

Figure 5.12 illustrates a subset of cardiac cycles from subject P11 with predicted temporal quiescence (time of quiescence occurrence within a cardiac cycle with respect to the most recent R-peak of the ECG) derived from different quiescent prediction methods.

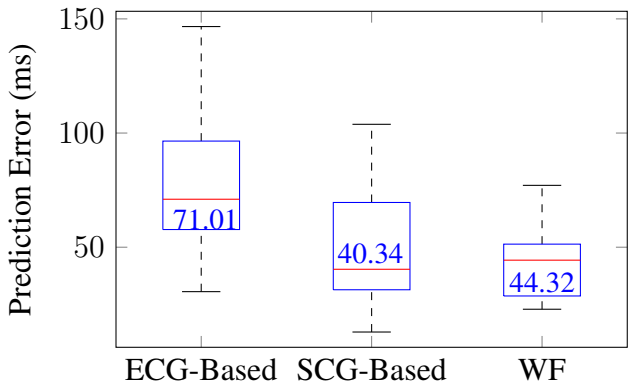

Figure 5.11: Box plot of quiescence prediction error (milliseconds) over all 18 subjects. On each box, the central mark indicates the median (value in red), and the bottom and top edges of the box indicate the 25th and 75th percentiles, respectively. The median prediction error for ECG-, SCG- and WF-based method are 71.01 ms, 40.34 ms and 44.32 ms, respectively. No outlier was observed. ECG-based prediction resulted in the most error. WF and SCG-based predictions are comparable. The smallest variability is seen in the prediction error associated with WF.

SCG-based prediction is closer to the baseline echocardiography than ECG-based prediction. Fusion-based prediction fuses predictions from ECG and SCG, and performed the best. This is consistent with results in Figure 5.10 where WF-based quiescence prediction is the most effective quiescent prediction method for patient P11.

To better appreciate the utility of fusion-based prediction, let $\bar{E}_{pred}$ be the quiescent prediction error, from either the SCG- or WF-based prediction method. The error reduction R against the ECG-based prediction is calculated by

$$R = (\bar{E}_{ecg} - \bar{E}_{pred})/\bar{E}_{ecg} \times 100\%, \tag{5.1}$$

where $\bar{E}_{pred}$ could be $\bar{E}_{wf}$ or $\bar{E}_{scg}$. Figure 5.13 reports the error reduction derived from different prediction methods. This error reduction measures the percentage of average error that can be reduced from ECG-only-based quiescent prediction. The median of the reduced error corresponding to SCG- and fusion-based method are 49.78 ms and 46.96 ms, respectively. WF- and SCG-based methods reduced comparable percent of prediction

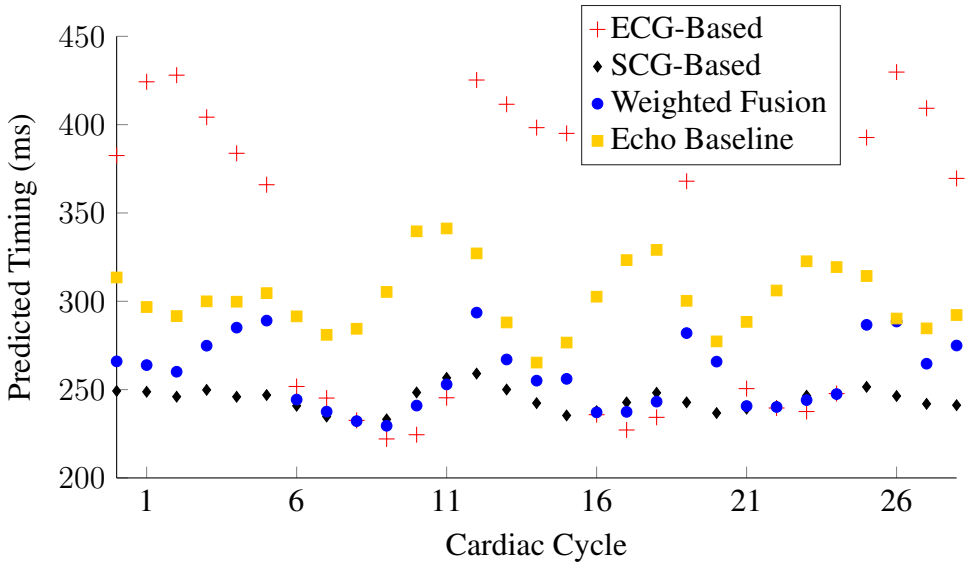

Figure 5.12: A subset of predicted temporal quiescence derived from different gating modalities for patient P11. Overall, WF gating is the optimal gating modality for P11 according to the average error presented in Figure 5.10.

error, however, WF resulted in less variability in the reduced error.

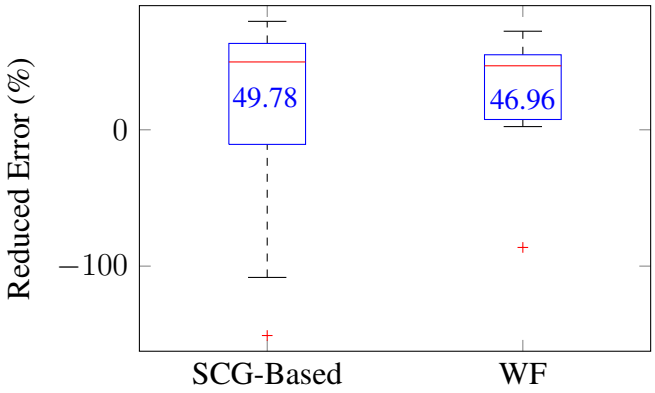

Figure 5.13: Box plot of percentage of error reduction (%) against the quiescent prediction error from the ECG-based prediction over the 18 subjects. On each box, the central mark indicates the median (value in red), and the bottom and top edges of the box indicate the 25th and 75th percentiles, respectively. The outliers are plotted individually using the "+" symbol. WF and SCG-based predictions are comparable, however, the variability in the reduced error associated with WF is smaller than with SCG.

5.5.3 CTA Reconstructed Image Quality

To place this work in the clinical setting, a board certified cardiothoracic radiologist, with over 7 years of experience interpreting cardiac CTA, evaluated the images and scored the quality of the coronary artery images using a 4 point Likert response format: 1 = excellent, 2 = good, 3 = adequate, 4 = non-diagnostic. The radiologist was blinded to the modality that selected the phase for the reconstruction. Significance was tested using the Wilcoxon signed-rank test.

Figure 5.14 illustrates the four main coronary arteries: left main (LM), left anterior descending (LAD), left circumflex (LCX) and right coronary arteries (RCA), from the origin to the first branch.

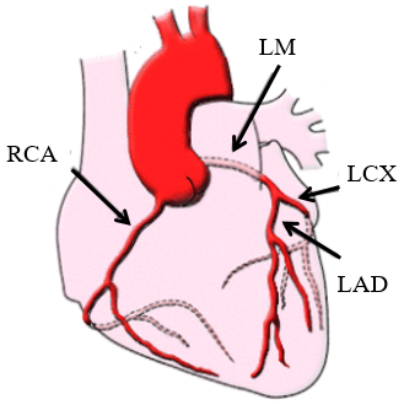

Figure 5.14: Four main coronary arteries. LM: left main; LAD: left anterior descending; LCX: left circumflex; RCA: right coronary arteries.

Table 5.4 reports the individual grading on LM, LAD, LCX and RCA. The histograms in Figure 5.15 further summarize the grade distribution of diagnostic quality associated with different prediction methods.

It was observed that the WF quiescence prediction is associated with a higher frequency of achieving lower Likert scale grade, indicating that WF yielded the best diagnostic quality overall. The SCG-based prediction achieved better diagnostic quality than the ECG-based method because SCG has slightly higher frequency in achieving the lower Likert format grade. The WF prediction consistently achieved the best diagnostic quality for all patients,

Table 5.4: Diagnostic Quality Grades

Patient No.	P1	P2	P3	P5	P6	P7	P8	P9	P10	P11	Mean	p-value
Left Main (LM)												
ECG	1	2	2	1	1	1	1	1	1	3	1.40	
SCG	1	1	2	1	1	1	1	1	2	1	1.20	0.75
WF	1	1	1	1	1	1	1	1	1	1	1.00	0.25
Left Anterior Descending (LAD)												
ECG	1	2	3	1	2	4	2	1	2	4	2.20	
SCG	1	2	3	1	2	3	2	1	4	2	2.10	1.00
WF	1	2	1	1	2	4	2	2	1	2	1.80	0.38
Left Circumflex (LCX)												
ECG	1	2	3	1	2	4	2	2	2	4	2.30	
SCG	2	2	3	1	2	4	2	1	3	2	2.20	1.00
WF	1	1	4	1	2	4	3	2	1	2	2.10	0.75
Right Coronary Arteries (RCA)												
ECG	1	2	4	2	2	4	2	3	4	4	2.80	
SCG	2	3	4	1	2	4	2	2	3	2	2.50	0.53
WF	1	1	2	1	3	4	3	3	2	3	2.30	0.25

* The CTA data of patient P4 is missing.
** Grade: 1 = excellent, 2 = good, 3 = adequate, 4 = non-diagnostic. p-values calculated against ECG.
*** The p-values were derived from the two-sided Wilcoxon signed-rank test ($\alpha = 0.05$).

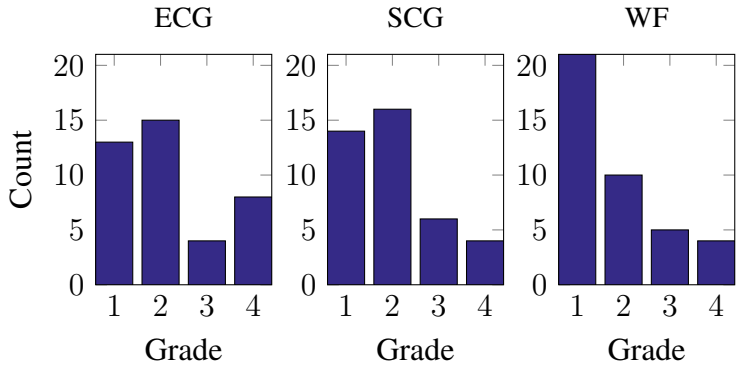

Figure 5.15: Histograms of the diagnostic quality grades. Four point Likert response scale: 1 = excellent, 2 = good, 3 = adequate, 4 = non-diagnostic.

whereas ECG achieves the least for all. The average grade over all the reconstructed volumes and all four vessel segments for the ECG, SCG and WF are 2.18, 2.00 ($p = 0.1957$) and 1.80 ($p = 0.0118$), respectively, assuming that there is no correlation among tests performed in LM, LAD, LCX and RCA. The p-values were derived from the Wilcoxon

signed-rank test ($\alpha = 0.05$). The current p-values are not sufficient to make strong conclusions about the effectiveness of the WF-based method in the diagnostic quality. However, the relatively smaller p-value of the WF-based method than the SCG-based method suggests a trend supporting WF-based method. Among the four segments, the RCA, which is generally degraded the most by motion artifacts of the coronary vessels, achieved the highest improvement in diagnostic quality using WF-based method as compared to the ECG.

Examples of RCA and LCX segments from cardiac CTA reconstructions of cardiac patient P11 are shown in Figure 5.16. Reconstructions associated with the WF-based prediction resulted in the highest diagnostic quality, while ECG-based prediction resulted in the lowest.

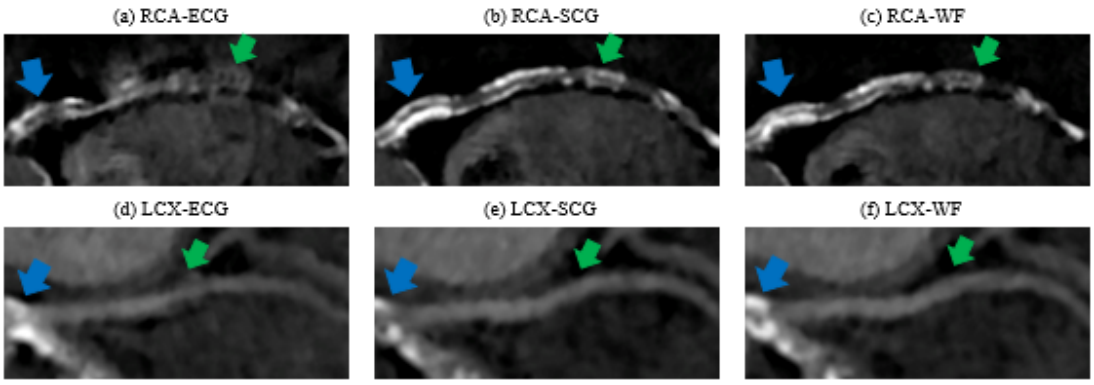

Figure 5.16: Comparison of the diagnostic quality of CTA images reconstructed at quiescent phases derived from different prediction methods. The CTA data presented were from patient P11. Blue arrows point to an example of calcification. Green arrows point to the motion artifacts. Compared to ECG-selected phases, the SCG-selected phases in (b) and (e), and WF-selected phases in (c) and (f) demonstrate sharper outline of the RCA and LCX. Calcification in the RCA is also more sharply defined by SCG- and WF-selected phases. The significant motion artifacts rendered the pointed (green arrows) regions of the RCA in (a) and LCX in (d) non-diagnostic for the ECG-selected quiescent phases.

Due to configuration limitations from the clinical CTA scanner, reconstructed CTA volumes for an individual are retrospectively generated at a constant phase over *all* cardiac cycles, rather than on a beat-by-beat basis. This constant phase is the average of the beat-by-beat quiescent phases derived from a specific quiescent prediction method. If the reconstruction is made on a beat-by-beat basis, the diagnostic quality associated with SCG- and

WF-based quiescence prediction could potentially provide a more substantial improvement over the ECG-based prediction.

5.6 Pre-Test and Pre-Categorization

As a crucial part of the SCG-based prediction, Chapter 4 proposed a pre-test of 3 minutes prior to the CTA data acquisition for collecting cardiac data to generate a personalized waveform template. This section investigates the value of the pre-test in the fusion-based prediction.

The fusion-based prediction adaptively fuses individual predictions from the ECG and SCG on a beat-by-beat basis. As mentioned in Section 5.3, special cases in which the SCG- or ECG-based prediction fails for a particular cardiac cycle may occur. A comprehensive model that encompasses different cases in the fusion-based prediction can be condensed to a mathematical form

$$P_{wf} = \begin{cases} P_{ecg} & w_{ecg} = 1 \text{ and } w_{scg} = 0, \\ P_{scg} & w_{scg} = 1 \text{ and } w_{ecg} = 0, \\ w_{ecg}P_{ecg} + w_{scg}P_{scg} & w_{ecg} \neq 0 \text{ and } w_{scg} \neq 0. \end{cases} \tag{5.2}$$

Although the results thus far showed that most of the subjects benefited from the fusion-based prediction, it is imprudent to exclude the possibility of getting better predictions from the ECG-only-based prediction, such as subject P2. The results in Section 5.5 indicate the existence of a rare case in which an individual may benefit from the ECG-only-based prediction, over all cardiac cycles. In this case, the fusion-based prediction becomes unnecessary. The cause of such a situation can be excessive body movement that deteriorates the SCG signal, abnormal heart sound associated waveforms that the template matching approach in the SCG-based prediction cannot recognize, or attachment issues of the accelerometer to the human body that leads to recording of random signals.

An individual who would only benefit from the ECG-based prediction can be categorized as the ECG-inclined subject, similarly, an individual who would benefit from the fusion-based prediction can be categorized as the WF-inclined subject. A pre-categorization using the cardiac data from the pre-test along with the pre-recorded cohort echocardiography data can possibly identify subjects of different categories. The subject-specific echocardiography is not feasible during the pre-test because of its operator-dependent property, thus, the subject-specific echocardiography was only used as the baseline for quiescent prediction to validate the performance of different prediction methods. However, the cohort-specific echocardiography is pre-recorded data from subjects within the same cohort, and thus is accessible during the pre-test.

The performance of the WF-based prediction relies on the relative goodness of SCG to ECG, as SCG serves to provide additional prediction information to correct the predictions derived from ECG alone. To quantify the goodness of the SCG relative to ECG, a subject-specific SCG index is derived during the pre-test, based on which pre-categorization can be made.

To derive the patient-specific SCG index, the quiescent phase generated from the cohort-specific echocardiography is used as the estimated baseline, denoted as $\bar{P}_{echo}(r)$ at heart rate r (bpm). The generation of $\bar{P}_{echo}(r)$ is elaborated in Chapter 4.3. During the pre-test where synchronous ECG and SCG are recorded, the estimated baseline is compared with the predicted quiescent phase derived from ECG- and SCG-based predictions, $P_{ECG}(\hat{r})$ and $P_{scg}(\hat{r})$, respectively, at a predicted heart rate $\hat{r}$. Thus, the estimated prediction errors can be presented as

$$\hat{E}_{ecg}(\hat{r}) = |\bar{P}_{echo}(r) - P_{ecg}(\hat{r})|, \tag{5.3}$$

$$\hat{E}_{scg}(\hat{r}) = |\bar{P}_{echo}(r) - P_{scg}(\hat{r})|. \tag{5.4}$$

Taking the mean of the estimated prediction errors over all cardiac cycles gives the average

estimated error for an individual, denoted as $\bar{E}_{ecg}$ and $\bar{E}_{scg}$ for ECG and SCG, respectively. The formula for deriving the SCG index I_{scg} is

$$I_{scg} = \frac{(\bar{E}_{ecg} - \bar{E}_{scg})}{\bar{E}_{ecg}} \bar{E}_{scg}. \tag{5.5}$$

The first term in the multiplication of Equation 5.5 measures the relative prediction error of SCG to ECG, and the sign of the first term indicates which error, $\bar{E}_{ecg}$ or $\bar{E}_{scg}$, is larger. The second term, $\bar{E}_{scg}$ serves as a scaling factor that zooms in the I_{scg} value for larger $\bar{E}_{scg}$. In this way, poor SCG signal that can potentially lead to large prediction error can be better distinguished. Intuitively, as the estimated SCG-based prediction error increases (i.e. $\bar{E}_{scg} > \bar{E}_{ecg}$), I_{scg} becomes more negative.

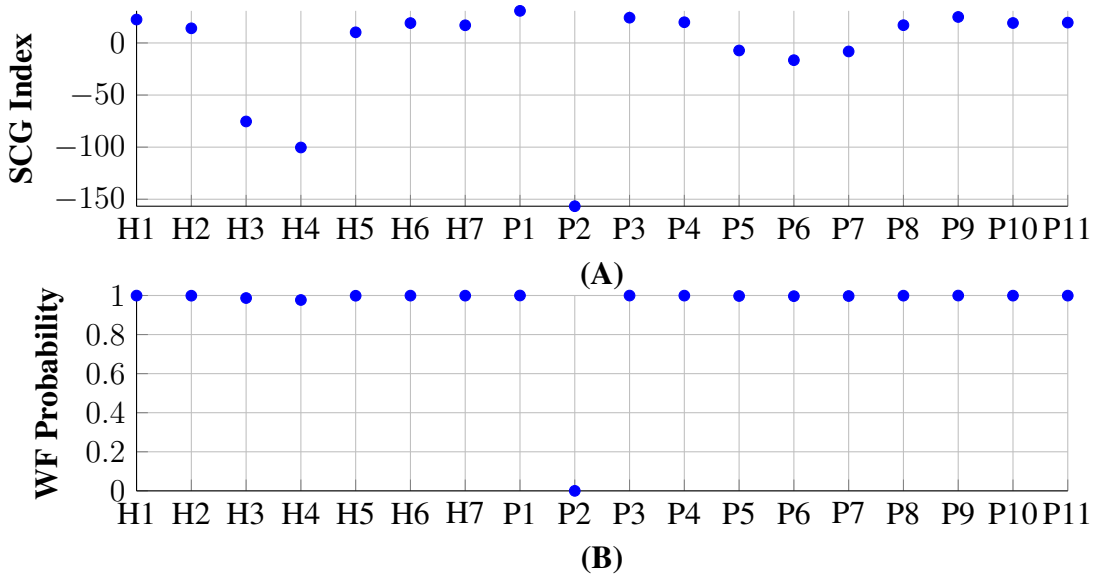

Figure 5.17: (A) The SCG index as a quantitative indication of the goodness of SCG relative to ECG. Larger SCG index indicates better performance of the WF-based prediction as compared to the ECG-based prediction. (B) The probability of applying the WF-based method, derived from the SCG index. The smaller the SCG index, the less likely it is to use the WF-based prediction. P2 has a very small SCG index, yielding low probability in using the fusion-based prediction, therefore, P2 is more suitable for using the ECG-only-based prediction method.

The SCG index of each individual was calculated and displayed in Figure 5.17 (A).

The results from the SCG index are consistent with those reported in Section 5.5.2. The larger the SCG index, the more likely the subject can benefit from SCG- or fusion-based predictions. The SCG index of subjects H3 and H4 are not high enough because they are potential candidates for ECG-based prediction. Patient P2 has the lowest SCG index, indicating that this subject has a large SCG-based prediction error and thus is more suitable for using the ECG-based prediction.

To better distinguish the subjects from the two categories, a transform was made in a way that converts the SCG index to a value that can be interpreted as the probability of using the WF-based prediction. To convert the SCG indices within 0 and 1, the array of SCG index from all subjects was subtracted by the minimal value and then divided by the maximal value to form a new array. An exponential transform of $e^{-\frac{100}{x}}$ for each value x in the new array was then made to take the smaller values closer to 0 and the larger values closer to 1. Lastly, the array was divided by the maximal value in the array. Figure 5.17 (B) presents the transformed SCG index, or the probability of using the WF-based method for quiescence prediction. Consistent with the result in Figure 5.10, patient P2 has a very low probability in using the fusion-based prediction.

5.7 Remarks

This part of the work developed a fusion-based quiescent prediction method by fusing individual predictions from the ECG and SCG on a beat-by-beat basis, relying on a three-layer ANN. Results from a pilot group of seven healthy subjects and eleven cardiac patients demonstrated that the fusion-based method is effective and robust. The major findings showed that the fusion-based prediction achieved 47% improvement in prediction error against the traditional ECG-only-based prediction. In addition, the prediction error derived from the fusion-based prediction method was less variant, and thus the fusion-based was more robust. In the observer study, the fusion-based prediction resulted in better diagnostic quality of CTA coronary vessels.

An additional investigation on the pre-categorization achieved the pre-test characteristics the ECG- and SCG-inclined subjects, which facilitates in deciding the optimal prediction method to apply. Overall, a comprehensive multimodal framework consisting of components investigated in Chapters 4 and 5 was established.

One limitation of this work is the evaluation of the diagnostic quality of the CTA reconstructed images. For each subject, one CTA volume was reconstructed over all cardiac cycles during the CTA data acquisition, at an average predicted phase derived from a specific prediction method. This average predicted phase was derived by taking the mean of the predicted phases from all cardiac cycles in the testing dataset. Therefore, each subject has three CTA reconstructed volumes that correspond to ECG-, SCG- and fusion-based prediction methods, respectively. Yet, during the CTA exam the prediction is supposed to be made on a beat-by-beat basis, rather than a single phase for all cardiac cycles. This was limited by the fact that the CTA data was not acquired simultaneously with the ECG and SCG signal, thus, validation cannot be achieved in a per cycle manner. The concern of acquiring CTA data simultaneously from the human body is the excessive amount of radiation. Future work may possibly start with simultaneous data acquisition on an animal model. In a complementary fashion, additional radiology readers will be recruited to explore the effect of inter-reader variability.

Another limitation lies in the features used in ANN of this study. The selected features were individually demonstrated to be effective representations of cardiac signals based on findings of previous research [70, 105–107, 109]. However, the applied feature set may be sub-optimal and a superior feature set can be established by investigating other features and attempting different combination of features.

With respect to the sample size, more participants are expected to be recruited, particularly coronary cardiac patients, to enlarge the subject population. The inclusion of additional subjects would enhance the statistical significance of improvement in diagnostic quality associated with the WF-based prediction. In addition, the expanded subject popula-

tion can lead to a more generalized training dataset, because the pre-defined ANN depends highly on the properties of the training dataset. The more comprehensive the extracted features, the less biased the trained ANN becomes. Furthermore, the threshold for the SCG index in pre-categorization can be optimized with more subjects' data.

Implementation of the multimodal framework in real-time with relevant hardware integration is the natural next step. This requires a rigorous consideration of computational complexity and time delay occurring in different stages of signal transmission and processing. In addition, the co-investigation and enhancement of both hardware and software makes it highly possible to achieve a better diagnostic image quality and reduced radiation exposure in cardiac imaging.

CHAPTER 6

NEAR REAL-TIME IMPLEMENTATION

Previous chapters are dedicated to demonstrating the effectiveness of the cardiac-motion-based signal in improving the accuracy of quiescence prediction, as well as the potential of the multimodal framework for cardiac CTA gating. This chapter focuses on establishing a real-time prototype for the multimodal framework. To this end, existing hardware and software platforms were integrated, and algorithms developed in previous chapters were adapted to achieve a near real-time implementation. Validation of the prototype was made using both pre-recorded and real-time streaming data. Additionally, a hardware layout was designed for developing an independent device dedicated to the multimodal prediction. Overall, this work demonstrates the feasibility of the ECG-SCG dual gating[1] framework for cardiac CTA data acquisition.

Near real-time implementation is an important step toward applying the dual gating strategy to the clinical setting. Other researchers have made initial attempts in dual gating, and the results thus far are promising. In 2004, General Electric (GE) Medical Systems (a subsidiary of GE, Boston, MA, USA) was awarded a patent regarding the invention of mechanical gating of CT [61, 62]. This invention proposed a method that uses a non-electrical sensor for gating, and reported a schematic hardware design of integrating a mechanical sensor to the CT machine. The proposed method correlates the set of ECG signals and mechanical motion signals to determine the cardiac phases at which CT reconstruction should be carried out. The goal of this method is to improve the quiescent phase selection, but not particularly for optimizing the quiescence prediction for prospective gating.

Another promising example of dual gating is the DTU200/300 dual channel MRI trig-

[1] Dual gating refers to utilizing two cardiac sensing modalities for the gating of a cardiac imaging machine, while traditionally, gating is achieved with only one sensing modality, e.g., the ECG signal.

gering and gating system (BIOPAC Systems, Goleta, CA, USA) [63] which was released in 2008. The purpose of this system is to improve tumor and/or lesion qualification when imaging the lung and abdominal regions by minimizing respiratory motion artifacts [117]. Dual mode in this system refers to a cardiac signal, either ECG or continuous blood pressure (BP) signal, in combination with the respiratory (RSP) signal. The modality of the cardiac signal (ECG or BP) can be manually selected to work together with the respiratory signal for MRI gating, based on the subject-specific data acquired prior to the MRI exam. The quiescent phases in the RSP signal are determined relying on a user selectable thresholding method. The output pulses indicating the trigger of MRI imaging is timed as a delay relative to the BP peak or R-peak of the ECG.

More recently, a group of researchers developed two approaches of dual gating for PET imaging, both of which demonstrated the potential of cardiac-motion-based signal in cardiac PET imaging. One approach is to use the SCG signal acquired from a tri-axis accelerometer together with the ECG signal for cardiac PET gating [42]. Another is a mircroelectromechanical (MEMS)-based dual gating method that relies on two non-electrical sensors, a tri-axial accelerometer and a gyroscope [43]. In the latter approach, cardiomechanical activities from the echocardiography observations were used to validate the accuracy of the dual-sensor solution. However, the feasibility of these dual-sensor approaches in real-time cardiac gating applications has not yet been established.

As a step further, this work developed a near real-time ECG-SCG quiescence prediction framework, and investigated its feasibility and effectiveness. This chapter presents the work from three aspects. The first two aspects introduce the hardware (Section 6.1) and software (Sections 6.2 - 6.3) implementation of the framework. The third aspect (Section 6.4) reports results from the human subject testing.

6.1 Enhanced Data Acquisition System

Chapter 3.2 elaborates the custom data acquisition system and the results presented thus far (Chapter 4 and 5) were achieved from the data acquired using the custom system. The accuracy of the SCG-based prediction was compromised by the sub-optimal configurations of the sensor/accelerometer in the ECG-SCG custom device, especially the relatively low signal-to-noise ratio. Hence, an enhanced data acquisition system was designed to overcome these technical issues.

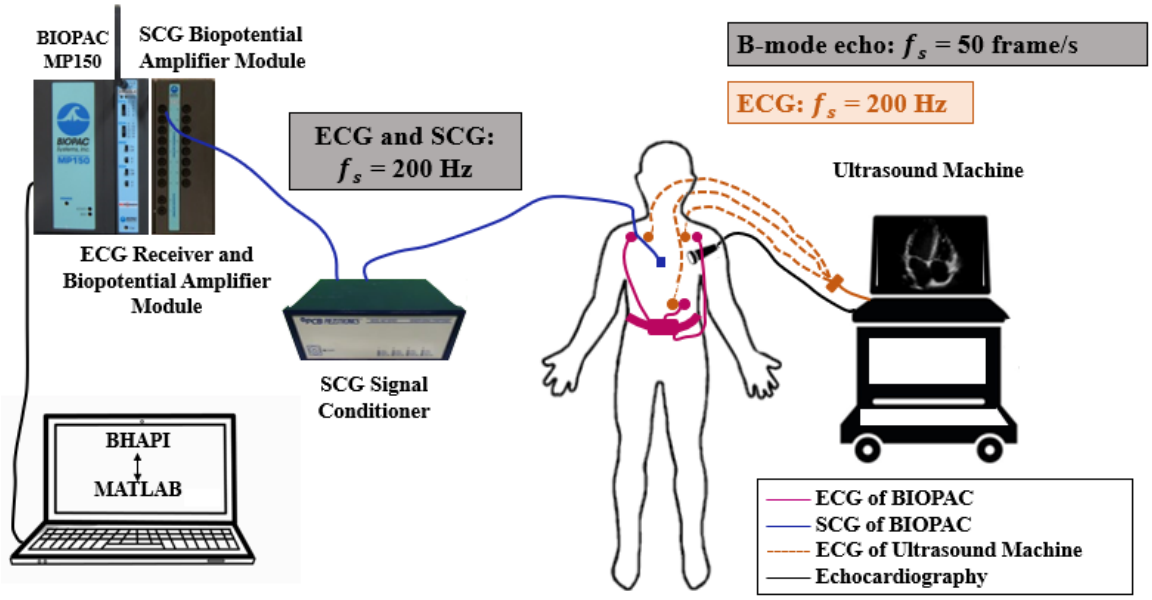

Figure 6.1: Overview of enhanced data acquisition system setup. f_s is the sample rate.

Figure 6.1 illustrates the data acquisition setup of the enhanced system. The procedure of data acquisition remains the same as that of the custom system, as described in Chapter 3.2, where the ECG, SCG and B-mode echocardiography data were acquired simultaneously. However, the characteristics of the devices in the enhanced system are different and are vital to the near real-time implementation. Thus, a detailed presentation of individual devices comprising the enhanced system is exhibited in Figure 6.2, and the specifics of each device are summarized in Table 6.1.

The BIOPAC MP150 System enables synchronized data acquisition and real-time anal-

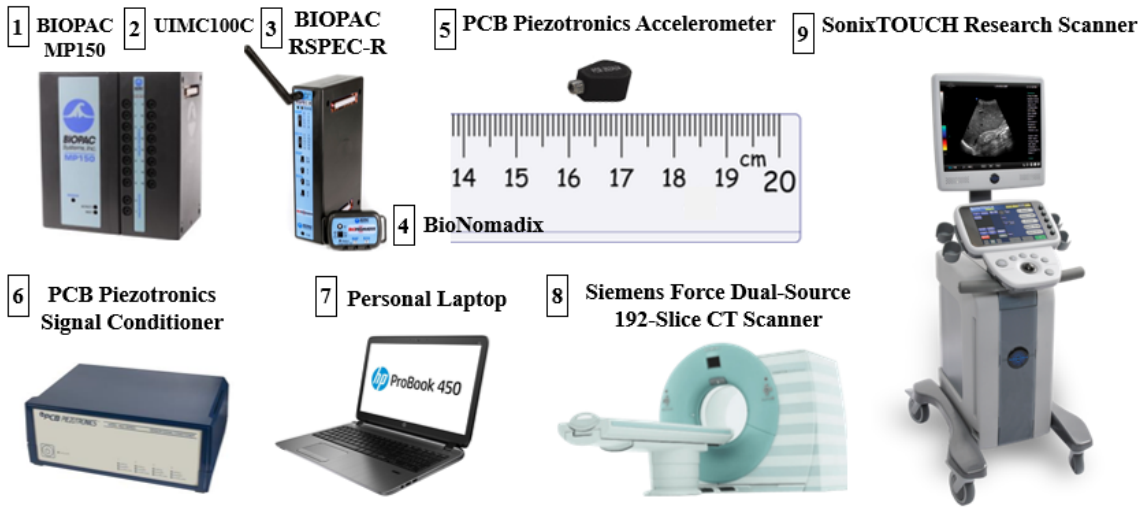

Figure 6.2: Devices used in this work.

Table 6.1: Hardware Specifics

Item	Component	Technical Details
1	BIOPAC MP150 (BIOPAC Systems, Goleta, CA, USA)	ECG and SCG data acquisition and analysis system Sample rate: 200 Hz (adjustable, aggregate sample rate up to 400 kHz) ADC resolution: 16 bit
2	UIMC100C (BIOPAC Systems, Goleta, CA, USA)	Biopotential amplifier module for SCG
3	RSPEC-R (BIOPAC Systems, Goleta, CA, USA)	Biopotential amplifier module for ECG
4	BioNomadix (BIOPAC Systems, Goleta, CA, USA)	Wireless ECG transceiver Transmitter carrier frequency: 2.4 GHz Analog filter bandwidth: 0-150 Hz
5	Accelerometer (Analog Devices, Norwood, MA, USA)	Cardiac-motion-based sensor (refer to Table A.1)
6	Signal Conditioner (PCB Piezotronics Inc, Depew, NY, USA)	In-line charge and voltage amplifier for SCG Spectral noise: $0.06\,\mu V/\sqrt{Hz}$ $(10-100$ Hz); $0.10\,\mu V/\sqrt{Hz}$ $(1-10$ Hz); $0.67\,\mu V/\sqrt{Hz}$ $(<1$ Hz)
7	Laptop (Hewlett-Packard, Palo Alto, CA, USA)	Processor: Intel Core i7-4702MQ, 4 cores, clock speed at 2.2 GHz Software: MATLAB 2017 (MathWorks, Natick, MA, USA)
8	Sonix RP Scanner (BK Ultrasound, Richmond, BC, Canada)	B-mode echocardiography and ECG acquisition machine B-mode frame rate: 50 Hz/frame ECG sample rate: 200 Hz
9	Somatom Force (Siemens, Erlangen, Germany)	CTA imaging data acquisition machine Dual-energy 192-slice Data acquisition window duration: 66 ms

ysis of the ECG and SCG signals. Upon receipt by the MP150, analog signals are individually filtered/conditioned by the corresponding biopotential amplifier modules. Both analog signals are then sampled by an analog-to-digital (ADC) in the MP150 at a rate of 200 Hz. This meets the requirement of Nyquist sampling theorem for both signals[2], while minimizing the computational efforts. The internal buffer of MP150 can store up to 6M samples. Digitized samples are then relayed to the laptop via an Ethernet crossover cable at a bit rate of 10 Mbps [118]. Before computerized processing, the incoming samples are temporarily stored in a buffer exploited by the MP150 in the laptop.

The enhanced data acquisition system advances the custom system in its capability of processing the streaming data in real-time. In the enhanced system, the streaming data is transferred to a computer for quiescence prediction in a near real-time manner, while the original custom system simply records and saves the data for offline computerized processing afterwards. Built upon previous work, this body of work continues to use MATLAB (MathWorks, Natick, MA, USA) as the computerized processing tool for the near real-time implementation. Future development can consider using low-level programming language, i.e. C language, to improve the real-time performance.

The BIOPAC hardware API (BHAPI) enables interaction between the data acquisition system, MP150, and third-party software programs, i.e. MATLAB, for basic data acquisition [119]. Specifically, BHAPI allows for streaming data transfer and programming interface via a dynamic link library (DLL). The precompiled routines, methods, functions and objects of the DLL can be readily used by MATLAB to control the MP150.

The accelerometer in the enhanced acquisition system is a primary component that significantly enhances the performance of quiescence prediction. Table A.1 in Appendix A briefly compares the sensor characteristics of the sensors used in the enhanced and custom data acquisition systems. The sensor in the enhanced system has significantly lower RMS noise level and is much lighter. The entire footprint of this accelerometer is as small as a

[2]The bandwidth of interest for both ECG and SCG signals are from 0 to 50 Hz.

fingernail (Figure 6.1, image No.5). Additionally, the sensor in the enhanced system was tested for CTA imaging by attaching to a phantom. The result demonstrated insignificant streak artifacts during the cardiac CTA scan.

Retrospective cardiac CTA data were acquired and reconstructed independently using a Siemens Force dual-source 192-slice CT scanner (Siemens, Erlangen, Germany) with data acquisition window duration of $66\,\mathrm{ms}$. These CTA data are used for assessing the diagnostic quality of quiescence predicted from different modalities.

The Siemens Force scanner not only achieves higher temporal resolution, but also significantly reduces the radiation dose, as compared with the previous generation of the dual-source cardiac CTA, the Siemens SOMATOM Definition (introduced in Chapter 3). It was reported that the radiation dose resulting from prospective gating on the Siemens Force is approximately 0.44 mSv [120], while it is approximately 2.8 mSv for the Siemens SOMATOM Definition [19]. The overall radiation dose resulting from retrospective gating of the Siemens SOMATOM Definition is as high as 18.4 mSv [121], while the Siemens Force can reduce the radiation to 12 mSv or lower [122].

The following sections discuss two major attributes of the software aspect of the near real-time implementation: latency (Section 6.2) and computerized processing (Section 6.3). Overall, the latency determines the feasibility, and the computerized processing contributes to the effectiveness of the near real-time system.

6.2 Latency

Latency is an important aspect for evaluating the real-time computing and is crucial for real-time prediction. The concept of "real-time" is not equivalent to achieving the fastest processing [123]. Real-time requires processing fast enough to meet the deadline within specified time constraints. In summary, the time constraints imposed on the near real-time implementation of this work are twofold:

1. The latency, Δt_4, introduced by the computerized processing cannot exceed a speci-

fied tolerance ΔT^*, namely,

$$\Delta t_4 \leq \Delta T^*, \tag{6.1}$$

where ΔT^* is the duration for receiving and accumulating a frame of data samples for processing. The value of ΔT^* relies on the frame size which is discussed in Section 6.3.1.

2. The effective prediction for gating, ΔT_g^*, is a valid time duration, namely,

$$\Delta T_g^* > 0. \tag{6.2}$$

This requires that the predicted timing for gating is not missed after synthesizing the total latency.

Figure 6.3 illustrates the epochs of signal transmission, $t_0 - t_3$, for ECG and SCG signals, respectively. Additionally, epoch $t_3 - t_4$ of computerized processing is also presented in Figure 6.3. Due to different device configurations, the transmission duration of ECG and SCG signals can be different for the same epoch. The total latency associated with a signal is the sum of latency introduced by each epoch.

The first epoch, $t_0 - t_1$, starts with the transmission of cardiac signal from the heart to cardiac sensors. The ECG signal, an electrical signal, has a negligible transmission through the body. However, the transmission of the seismographic signal is not as straightforward. The mechanical wave transmission relates to the heart-to-chest distance which varies due to multiple factors such as age, gender and patient body habitus [124, 125]. A conservatively large heart-to-chest distance of 4 cm is considered. Given that the compression wave propagation speed in tissue is approximately $1540\ \mathrm{m/s}$, the estimated mechanical signal transmission duration is $26\,\mu\mathrm{s}$.

The second epoch, $t_1 - t_2$, is the signal transmission from the sensor to the data acquisition device. In transmitting the ECG signal to the MP150, the wireless transceiver

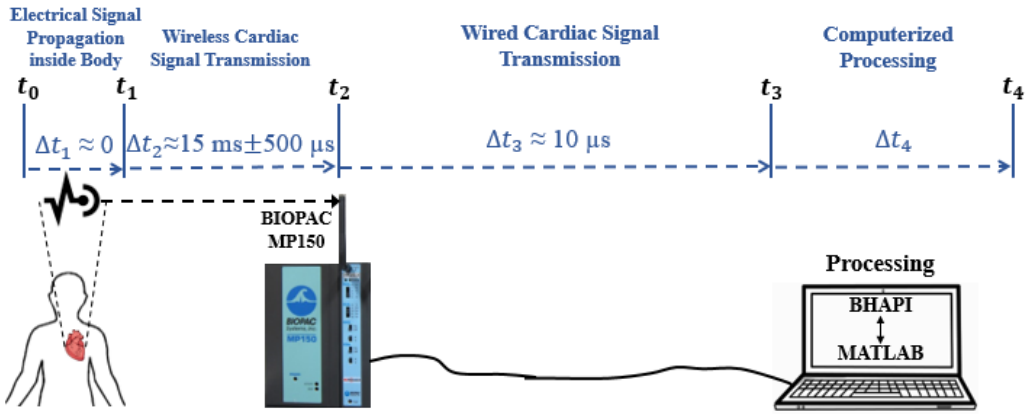

(A) ECG signal transmission and processing epochs.

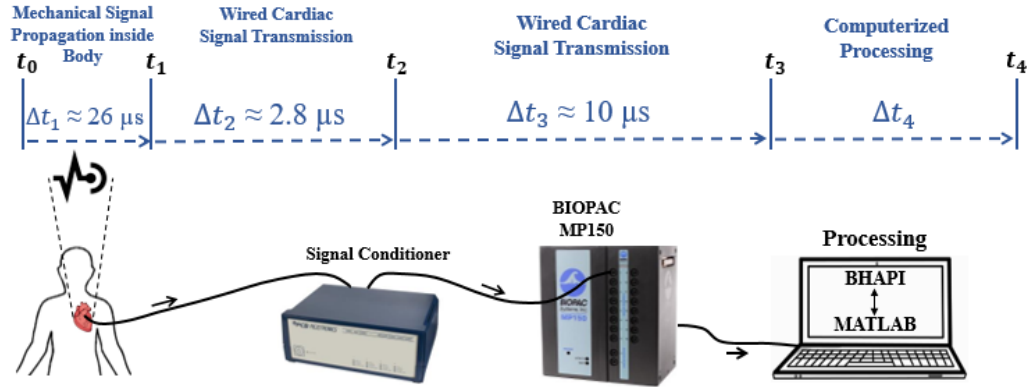

(B) SCG signal transmission and processing epochs.

Figure 6.3: Breakdown of epochs of (A) ECG and (B) SCG signals transmission and processing. The latency introduced by each epoch i is denoted as Δt_i for $i = 1, 2, 3, 4$.

introduces a $15\,\mathrm{ms}$ biased delay and $500\,\mu\mathrm{s}$ unbiased delay[3]. The wired signal transmission duration of the SCG signal to the signal conditioner is negligible. However, the SCG signal conditioner introduces approximately $2.8\,\mu\mathrm{s}$ of delay for the amplification operation.

In the next epoch, $t_2 - t_3$, signals undergo conversion and amplification in the MP150 system and are then relayed to the computer. The multiplexer switching between two signal channels causes a $5\,\mu\mathrm{s}$ delay and the ADC causes another $5\,\mu\mathrm{s}$ delay [126], resulting in a total of $10\,\mu\mathrm{s}$ of delay in this epoch. [4]

[3]The biased delay comes from the deterministic straight transmission and unbiased delay is caused by jitter

[4]As an additional note, the dual ADCs in the MP150 system sample any chosen two channels simultaneously, so two channels of data can be acquired at a rate as high as 200 kHz with zero channel-to-channel latency.

Following signal transmission is the epoch of computerized processing, $t_3 - t_4$. The computerized processing involves invoking functions in DLL to download the data from the computer buffer and process the frame-based data for prediction. The latency Δt_4 depends on the computerized algorithms and is intricate. Thus, Section 6.3 exclusively elaborates the computerized processing, as well as addresses the latency Δt_4 and tolerance ΔT^*.

In summary, the total latency introduced by the hardware transmission and computerized processing is $\Delta T = \Delta t_1 + \Delta t_2 + \Delta t_3 + \Delta t_4$. Specifically, the latency is $\Delta T_{ecg} = 15.51\,\mathrm{ms} + \Delta t_4$ for the ECG signal, and $\Delta T_{scg} = 38.8\,\mu\mathrm{s} + \Delta t_4$ for the SCG signal.

The total latency is crucial for effective prediction. Let ΔT_g be the predicted duration from a detected reference feature, i.e. R-peak of the ECG signal, to the predicted center of the quiescent period. The effective prediction for gating is a shorter duration obtained by synthesizing three durations: the total latency ΔT, data acquisition duration of the CT scanner T_{acq}, rising time of the x-ray tube potential Δt_r, and the delay from the detected feature to the most recent data sample Δt_d.

In this body of work, the Siemens Force Scanner (Siemens, Erlangen, Germany) was used and its data acquisition window is $T_{acq} = 66\,\mathrm{ms}$. The estimated duration for the x-ray tube to rise to its full potential[5] is $\Delta t_r = 0.5\,\mathrm{ms}$ [127–129].

Therefore, the effective prediction for gating, ΔT_g^* is

$$\begin{aligned}\Delta T_g^* &= \Delta T_g - \Delta T - \frac{T_{acq}}{2} - \Delta t_r - \Delta t_d, \\ &= \Delta T_g - \Delta T - \frac{66}{2}\,\mathrm{ms} - 0.5\,\mathrm{ms} - \Delta t_d, \\ &> 0,\end{aligned} \tag{6.3}$$

or equivalently, $\Delta T_g > \Delta T + 33.5\,\mathrm{ms} + \Delta t_d$.

If the prediction comes out ineffective, i.e. $\Delta T_g^* \leq 0$, CTA gating and data acquisition will not be carried out and the next cardiac cycle automatically becomes the target of

[5] Although typically a rising duration of less than $0.5\,\mathrm{ms}$ can be achieved, this work conservatively chose to use $0.5\,\mathrm{ms}$ for estimation.

quiescent prediction.

6.3 Computerized Processing

The computerized processing is a crucial part of the near real-time processing because it is closely related to the total latency and quiescent prediction accuracy. In summary, this section regarding the computerized processing addresses

1. Frame-based quiescent prediction strategies using the ECG-, SCG- and fusion-based methods in a near real-time manner.
2. The latency, Δt_4, introduced by the frame-based computerized processing.
3. The time tolerance, ΔT^*, to the computerized processing.

6.3.1 Frame-Based Processing

Frame-based data is a typical format in real-time systems. It maximizes the efficiency of the system by distributing the fixed process overhead across many samples. In addition, processing a frame of samples at once reduces the computational time of the signal processing algorithms.

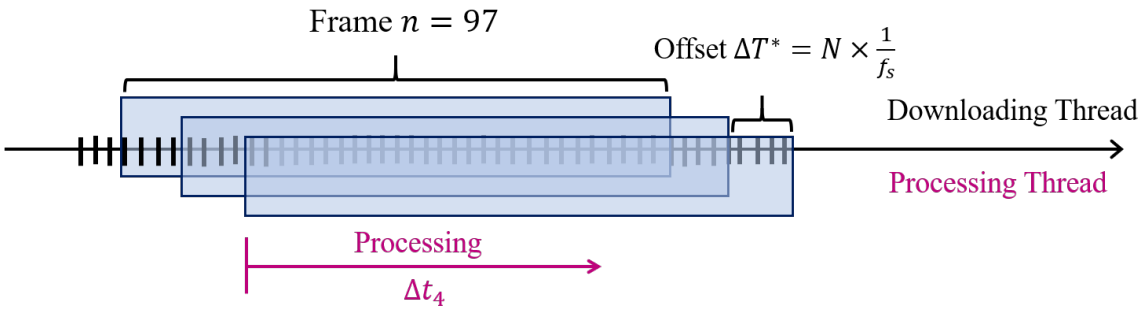

Figure 6.4: Frame-based processing. The processing frame size is $n = 97$ and offset is $N = 20$. f_s is the sample rate.

The processing frame and sliding offset are important components of the frame-based processing, as illustrated in Figure 6.4. The processing frame is a frame of samples that undergo computerized processing in one iteration, and the sliding offset indicates the number

of new samples per iteration in the processing frame. In this work, the sample size of the processing frame is $n = 97$, and the sliding offset is $N = 20$ data samples. The number of samples in the processing frame is restricted by the filter design. For pre-processing, a Hamming window configuration of order less than 32 does not effectively attenuate the high frequency noise and the order of 32 requires a minimal of 96 samples to process. The duration of QRS in ECG signal for adults is 0.06-0.10 s, corresponding to maximal 20 samples at 200 Hz sample rate. Therefore, the latency introduced by the computerized processing, Δt_4, cannot exceed the tolerance duration, ΔT^*, for accumulating a frame of the most recent N data samples, indicating that

$$\Delta t_4 \leq \Delta T^* = N \times \frac{1}{f_s} = 0.1 \text{ s}, \tag{6.4}$$

where $f_s = 200$ Hz is the sample rate. This is to guarantee to take in consecutive data samples for computerized processing without missing any.

Compared with the regular offline processing, the frame-based processing for real-time is limited by the frame size. Algorithms that used to process the pre-recorded long-term data may fail in dealing with the short-term data, or are not able to complete within a specific time tolerance. For example, a popular method to identify the QRS complex of the ECG signal in real-time was developed in an early work by W. Tompkins [104]. This method used a special digital band-pass filter and adaptive thresholds to significantly reduce the false detection rate. However, the "real-time" in this method is relative to approximately 2-3 cardiac cycles of delay due to the requirement of certain number of data samples to update the threshold. Therefore, this method is not suitable to be applied to this work.

To better present the near real-time processing, a breakdown of the modules of the processing system are illustrated in Figure 6.5. Major processing modules are highlighted in blue and are elaborated in Sections 6.3.2 - 6.3.5.

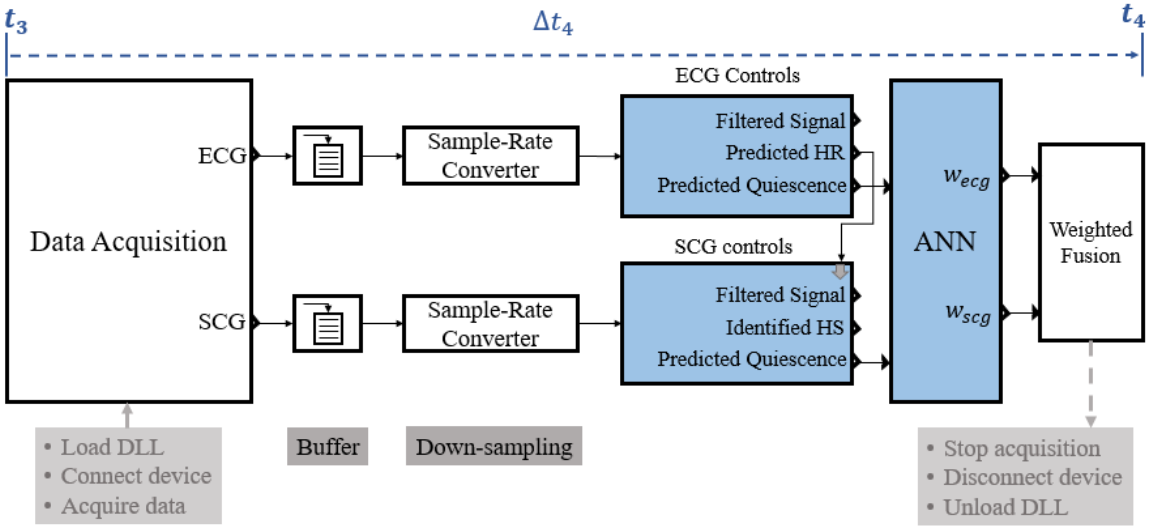

Figure 6.5: Computerized processing modules. Modules in blue are major processing modules discussed in Sections 6.3.2 - 6.3.5.

6.3.2 Pre-Processing and Pre-Test

The frame-based pre-processing includes filtering and obtaining initialization values from the pre-test prior to the CTA data acquisition. This part of work corresponds to the filtering function in the signal controls modules in Figure 6.5.

To minimize the artifacts and noise such as the skin-electrode interface interference and respiratory drift, as well as to preserve the QRS components in the ECG signal, a band-pass FIR filter with a Hamming window configuration and pass-band of 0.5-50 Hz was applied. The same filter configuration was used for filtering the SCG signal to reserve the heart sound associated waveforms that lie within 10-50 Hz. The order of filters for both ECG and SCG signals were chosen to be 32. This was for the sake of computational efficiency in real-time processing, while ensuring that undersired artifacts and noise are filtered out.

During the pre-test, a sequence of cardiac cycles are acquired and processed entirely in an offline manner. Processing of the pre-test data includes filtering the ECG and SCG signals, segmenting signals based on the R-peaks of the ECG, and detecting the heart sound associated waveforms in the SCG signal. To ensure that the heart rate can be predicted from the linear regression of the previous six heart beats, a minimum of eight cardiac

cycles are acquired during the pre-test. The acquisition of eight cardiac cycles also enables initialization for the detection of R-peaks in the ECG signal as well as the heart sound associated waveforms in the SCG signal.

As a bounding limit of this work, the fastest heart rate of interest is 120 bpm and the slowest is 40 bpm. Therefore, given the sample rate of $f_s = 200\,\mathrm{Hz}$, the maximum number of data sample within eight cardiac cycles is 2400, corresponding to 12 s of duration.

6.3.3 Quiescence Prediction

After pre-processing the ECG and SCG signals, individual predictions for the ECG and SCG signals are derived. This part of work corresponds to the prediction functions in the signal controls modules in Figure 6.5.

The ECG-based prediction was implemented using the ECG-gating function. The mathematical form of the ECG-gating function [130] used by the Siemens Force scanner is

$$P_{ecg}(\hat{r}) = \begin{cases} 70\% & \hat{r} \leq 65 \text{ bpm}, \\ 75\% & 65 \text{ bpm} < \hat{r} \leq 70 \text{ bpm}, \\ 40\% & 70 \text{ bpm} < \hat{r} \leq 80 \text{ bpm}, \\ 35\% & \hat{r} > 80 \text{ bpm}, \end{cases} \tag{6.5}$$

where $\hat{r}$ is the predicted heart rate. P_{ecg} is the predicted quiescence phase (%) measured as a delay from the most recent R-peak of the ECG to the start of the quiescent period.

The SCG-based quiescence prediction is not as straightforward. It requires detection of the heart sound associated waveform as the reference and estimation of the delay from the reference to the predicted quiescence. The peak of the systolic heart sound associated waveform (HS1) almost always 25 ms lags behind the most recent R-peak, corresponding to 5 samples of delay at a sample rate of 200 Hz. The peak of the diastolic heart sound associated waveform (HS2) is more challenging to identify since there is no such definite

marker as the R-peak to facilitate the identification. Therefore, a thresholding technique was applied to identify the peak of the diastolic waveform in real-time. The delay from the detected SCG feature to the quiescence can be derived from a phase delay function, e.g., delay in percentage with respect to the predicted heart rate. Figure 6.6 presents a visualization of the ECG- and SCG-based prediction implemented in a near real-time manner.

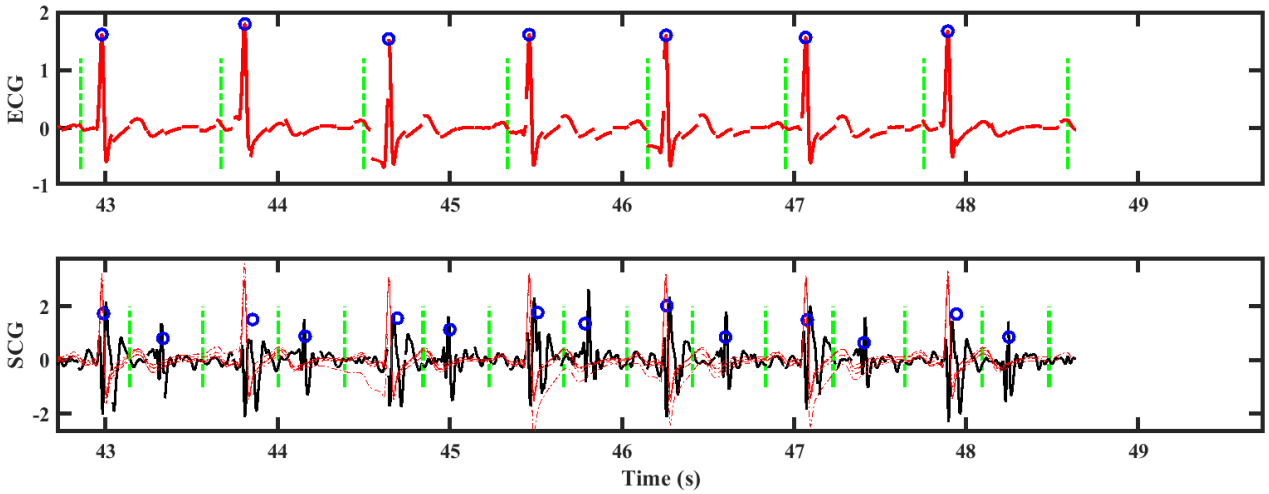

Figure 6.6: Visualization of the ECG- and SCG-based near real-time quiescence prediction, respectively. The blue circles are identified heart sound associated features as references for SCG-based predictions, and the green dotted lines indicate the predicted quiescence. The ECG-base prediction derives only one prediction for each cardiac cycle, while the SCG-based prediction is able to derive a systolic and diastolic prediction for each cardiac cycle.

Although the SCG-based method is able to achieve both systolic and diastolic predictions upon identification of the corresponding heart sound waveforms, to make it a fair comparison among the ECG-, SCG- and fusion-based methods, only the predicted quiescence from the same cardiac period, either systole or diastole, are compared.

The cardiac quiescence derived from the patient-specific B-mode echocardiography was used as the baseline while evaluating the performance of the ECG-, SCG- and fusion-based predictions. Descriptions of the B-mode echocardiography can be found in Chapter 4.1.

6.3.4 Quiescence Fusion

The fusion-based prediction employs a three-layer ANN that provides weights for combining individual predictions from the ECG and SCG based on some selected cardiac features. The ANN configuration and related rationales are discussed in Chapter 5.2.

Although features used in Chapter 5.3 were demonstrated to be fair representatives of the cardiac signals and were effective in quiescence prediction, this pilot work of near real-time implementation further scales down the features for the sake of computational and time efficiency. In summary, the revised feature set contains a total number of 4 single-value features, out of which 2 are from the ECG signal and 2 are from the SCG signal. The procedure of selecting the features set is similar to that presented in Chapter 5.3. A detailed description and analysis of the revised feature set are presented in Appendix B.

6.3.5 Training, Cross-Validation and Testing

To validate the real-time prediction, training and testing of the ANN were made on cardiac data acquired from two cohorts of subjects. One cohort consists of five healthy subjects (mean age: 26; age range: 24-30 ; female/male: 1/4), and the other cohort consists of three cardiac patients (mean age: 61; age range: 41-71; female/male: 1/2). The testing was conducted on two healthy subjects in a real-time scenario, while the rest of the subjects were tested using their pre-recorded data in a simulated real-time manner.

Similar to the validation procedure in Chapter 5.4, training and testing were carried out in a leave-one-out manner within the two cohorts. *Testing* for a designated subject involves feeding the consecutive frames of the subject-specific data sequentially to the trained ANN. The testing output, fused predictions, were compared against the baseline quiescence derived from subject-specific echocardiography.

To train the ANN, the corresponding *training* dataset was constructed using the cardiac data from the rest of the subjects who belong to the same cohort as the designated subject. The training dataset contains categorized frames if data, labeled as “ECG” and “SCG”. The

labeling was made by comparing the ECG- and SCG-based predictions with the quiescence derived from the subject-specific echocardiography, respectively. Illustrations of signals that were assigned to different categories are shown in Figure 6.7. The modality that led to a smaller prediction error was considered as the optimal modality for a particular cardiac cycle. Accordingly, the corresponding data frames that served for quiescence prediction for the cardiac cycle was assigned the same modality as the cardiac cycle.

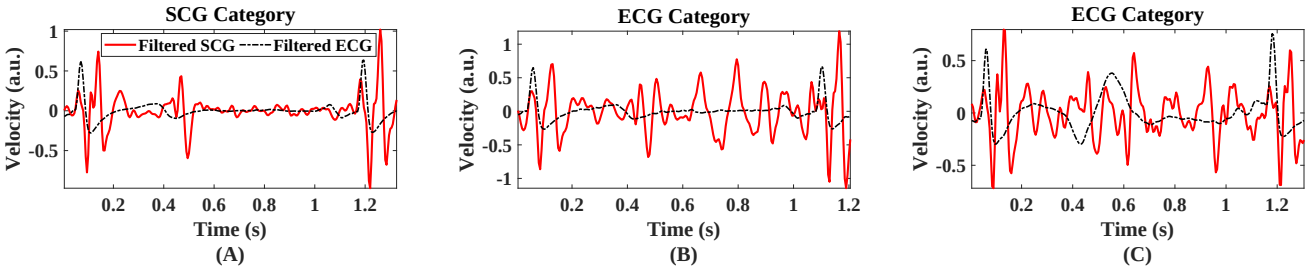

Figure 6.7: Examples of situations when different categories were assigned by the ANN binary classifier. The assignment was made according to the baseline subject-specific echocardiography. (A): Intuitively, when both the ECG and SCG signals are normal and devoid of noise, the SCG-based prediction will be assigned. (B) and (C): In the case when the SCG signal is noisy, the ECG-based prediction is assigned.

Overall, each category consisted of half of the training dataset. The training dataset was further randomly divided into four parts, one of which was used for cross-validation. Within each part of the training dataset, the percentages of the two categories remain consistent with the overall category percentages in the training dataset. On average, for each individual, the number of frames used for training the ANN was 7101, corresponding to an average of 720 cardiac cycle.

6.4 Results

6.4.1 Latency

As discussed in Section 6.2, two time constraints are imposed on the near real-time implementation, both of which are closely related to the latency introduced by the computerized

processing, Δt_4. First, Δt_4 cannot exceed the time tolerance $\Delta T^* = 0.1\,\mathrm{s}$. Second, the total latency ΔT has to be small enough to guarantee an effective prediction for gating.

To estimate Δt_4 of processing a single data frame, the latency of individual computerized processing module was first estimated. This was achieved by measuring the total time, T, of an individual module spent in processing a consecutive $n_1 = 500$ frames of 97 data samples[6]. The estimated duration t to process a single frame of 97 data samples is $t = \frac{T}{n_1}$. Table 6.2 summarizes the estimated duration introduced by modules in the computerized processing. In a similar manner, the total duration of processing a frame of 97 data samples was estimated.

Table 6.2: Latency of Modules in Computerized Processing

Module	Duration (ms)
Signal Condition	0.70
R-Peak Detection	1.70
HS Waveform Detection	1.40
ECG-Based Prediction	0.31
SCG-Based Prediction	0.15
Fusion-based Prediction	0.64
Other functions	0.20
Total	5.10

In fact, the latency associated with each data frame varies because the amount of computerized processing involved with each data frame differs. Frames with a new reference detected requires extra operations for quiescence prediction, compared with the frames without a reference, thereby introducing a longer latency. Essentially, this longer latency due to the prediction operations primarily affects the prediction for gating. An estimation of the computerized processing duration that includes quiescence prediction operations reported an average of $\Delta\bar{t}_4 = 5.10\,\mathrm{ms}$, leading to the total latency

$$\Delta\bar{T}_{ecg} = 15.51\,\mathrm{ms} + 5.10\,\mathrm{ms} = 20.61\,\mathrm{ms}, \tag{6.6}$$

[6] An alternative approach is using the MATLAB Profiler.

for the ECG, and for the SCG

$$\Delta\bar{T}_{scg} = 38.80\,\mu\text{s} + 5.10\,\mu\text{s} = 5.14\,\text{ms}. \tag{6.7}$$

Therefore, the first time constraint is satisfied, namely,

$$\Delta\bar{t}_4 = 5.10\,\text{ms} < \Delta T^*. \tag{6.8}$$

The second time constraint relates to the prediction for gating. Failure in providing an effective prediction results in missing prospective gating for a cardiac cycle. The missing count is reported in Table 6.4. Overall, the total latency associated with both signals were rational for generating effective predictions for gating, namely,

$$\Delta T_g > \max(\Delta\bar{T}_{ecg}, \Delta\bar{T}_{scg}) + 33.50\,\text{ms} + \Delta t_d = 54.11\,\text{ms} + \Delta t_d. \tag{6.9}$$

Therefore, the near real-time implementation of the multimodal framework is feasible.

As a side note, prior to the real-time quiescence prediction, loading the DLL for computerized processing took approximately 11 s and the pre-test for initialization took approximately 0.1 s. It was also observed that the computational efficiency was enhanced if other applications on the computer were terminated while the quiescence prediction program is ongoing.

6.4.2 Artificial Neural Network Classification

The subjects' clinical characteristics and corresponding ANN accuracy are presented in Table 6.3, in order of increasing heart rate, within each cohort. Subjects H1 to H5 are from the cohort of healthy subjects and P1 to P3 are from the cohort of cardiac patients. The classification accuracy is the percentage of correct categories being identified. Among all the subjects, the computerized processing were tested on H3 and H5 in a real-time scenario,

while the rest of the subjects were tested using their pre-recorded data.

Table 6.3: Subject Clinical Characteristics and ANN Accuracy

Healthy Subjects							
Subject	HR (bpm)	HRV (ms)	Age (year)/Gender	Weight (lbs)	Height (in)	Race	Accuracy (%)
H1	53	28	27/F	100	62	White	98.5
H2	68	45	27/M	155	68	Asian	97.3
H3†	72	50	24/M	185	70	White	99.3
H4	75	50	26/M	120	65	Asian	99.1
H5†	76	32	25/M	190	72	White	98.8
Mean	69	41	26/-	150	67	-	98.6
Std	9.4	10.3	1.7/-	39.5	3.6	-	0.8
Cardiac Patients							
P1	63	102	71/F	160	67	White	97.1
P2	73	57	41/M	265	74	Black	97.5
P3	80	60	70/M	170	69	White	98.0
Mean	72	73	61/-	198	70	-	97.5
Std	8.5	25.1	17.0/-	58.0	3.6	-	0.5

† Subjects H3 and H5 were bold to indicate that the computerized processing were tested on the in a real-time scenario, while the rest of the subjects were tested using their pre-recorded data.

The average classification accuracy is 98.6% for the healthy cohort and 97.5% for the patient cohort. Compared with the classification accuracy presented in Table 5.3 (89.9% for healthy subjects and 80.6% for cardiac patients), the accuracy derived from the new feature set has been improved, indicating that the revised feature set is more efficient in distinguishing the ECG and SCG signals.

6.4.3 Quiescence Prediction

The prediction error, in milliseconds, was calculated as the absolute difference between the predicted quiescence and the baseline subject-specific echocardiography. The prediction errors of the ECG-, SCG- and fusion-based methods for each individual are shown in Figure 6.8. The overall prediction error associated with ECG-, SCG- and WF-based methods over all subjects are 59.58 ± 20.01 ms, 34.67 ± 15.63 ms and 27.24 ± 12.16 ms. The fusion-based prediction demonstrated the least prediction error and is associated with less variation in the errors, while the ECG-based method yielded the most error.

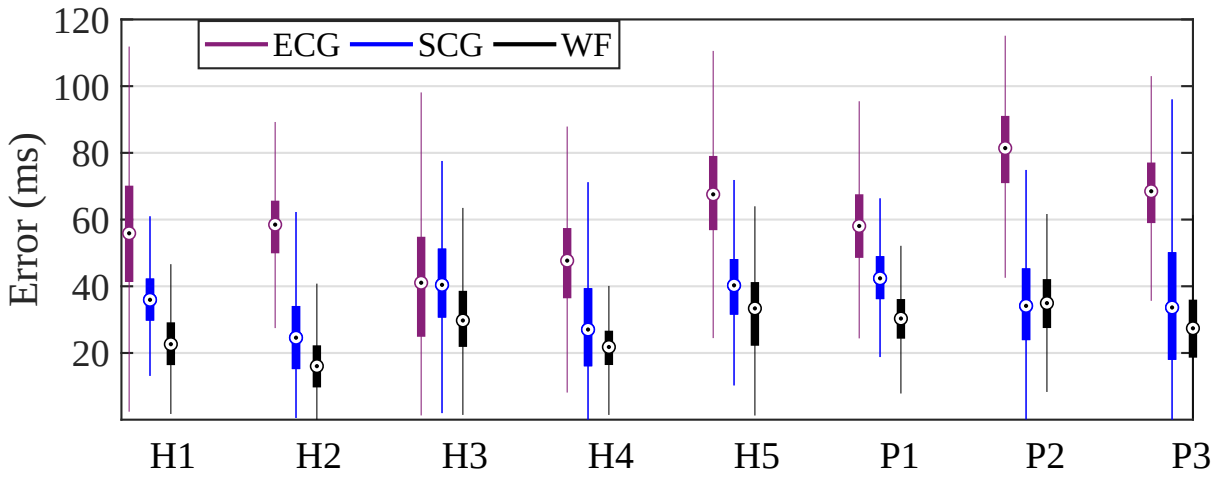

Figure 6.8: Quiescence prediction error derived from difference quiescent prediction methods. The overall prediction error associated with ECG-, SCG- and WF-based method over all subjects are 59.58 ms, 34.67 ms and 27.24 ms. The black dot in each boxplot indicates the median value.

Table 6.4: Average Quiescence Prediction Error

Healthy Subjects				
Subject	MN/TN[†]	$\bar{E}_{ecg}$ (ms)	$\bar{E}_{scg}$ (ms)	$\bar{E}_{wf}$ (ms)
H1	20/286	55.49	35.16	22.21
H2	12/305	57.14	27.52	17.56
H3	25/311	43.66	39.05	29.38
H4	19/275	48.07	28.07	22.47
H5	23/298	66.43	38.37	32.11
Mean	20/295	54.15	33.63	24.75
Std	5/15	19.56	15.05	11.86
Cardiac Patients				
P1	20/286	58.02	41.28	30.04
P2	25/301	79.81	34.31	35.44
P3	27/300	68.03	33.59	28.73
Mean	24/296	68.62	36.40	31.40
Std	4/8	17.32	16.41	11.51

[†] MN: Number of missed cardiac cycles by the SCG-based prediction; TN: Total number of cardiac cycles tested.

Table 6.4 reports the average prediction error for each individual as well as the missing count for the SCG-based prediction. The missing count is the number of cardiac cycles that

did not have predictions by the SCG-based prediction among the total number of cardiac cycles. The missing scenario can be a result of not having enough time before the predicted quiescence occurs, or inability to identify the heart sound associated waveforms in the SCG signal. On average, the SCG-based method failed in predicting quiescence for 6.8% of the cardiac cycles over all healthy subjects and 9.4% over the cardiac patients. In summary, the fusion-based prediction was an effective method for improving the accuracy of quiescence prediction.

6.5 Remarks

This work demonstrated that a near real-time ECG-SCG-based multimodal framework is feasible and effective for cardiac quiescence prediction. The augmentation of the traditional ECG-only-based prediction also seamlessly incorporated a pre-test and pre-categorization to facilitate the real-time prediction prior to the CTA exam. The promising results reinforces a positive prospect of the multimodal gating to be applied to the clinical setting.

One limitation of this work comes from the wireless ECG transceiver which introduces a latency of 15 ms. Replacing the wireless transceiver with a wired transceiver can significantly reduce the total latency, thereby easing the gating from missing the predicted timing.

The next limitation is lacking a thorough way of evaluating the goodness of the ECG signal. While the relative goodness of the SCG can possibly be evaluated by the SCG index reported in Chapter 5.6, it is helpful to develop methods for identifying the quality of the ECG signal. The purpose is to exclude the unreliable prediction derived from the sub-optimal ECG signal. An example of a sub-optimal ECG signal can be found in Figure 6.7 (C), where both the ECG and SCG signals are significantly distorted. In this case, the ECG-based prediction becomes unreliable. However, because the ANN binary classifier inclusively deals with two categories, ECG and SCG, the classification decision selects the relatively less distorted category rather than rejecting both categories. Ideally, this cardiac

cycle may be skipped for quiescence prediction.

Another limitation is the assumption that the adjacent data frames carry related cardiac information. Specifically, a frame of 97 data samples that are partly from the diastolic period of a cardiac cycle are used for predicting the systolic quiescence in the following cardiac cycle. Similarly, diastolic quiescence prediction requires features extracted from the data frame in the systolic period of the same cardiac cycle. Although intuitive, this assumption has not been validated.

Future work can focus on developing an independent device dedicated to the near real-time prediction rather than relying on a laptop. Appendix C outlines a schematic hardware layout as a potential vision of the dedicated device.

Future work can also investigate changing the processing window size and offset, as well as the sample rate to optimize the performance for quiescence prediction. Similarly, to improve the computerized processing aspect, particularly to optimize the execution time of a program, the algorithm, data structure, input, platform (operating system version or memory hierarchy) and programming language [131] can be investigated.

CHAPTER 7
FINAL REMARKS

7.1 Conclusions

This work demonstrated that the SCG-derived motion information can achieve improved quiescence prediction accuracy and that the sub-optimal ECG-only-based prediction can be augmented by an ECG-SCG dual-gating framework for marked improvement. Furthermore, this work reinforces the potential of the real-time dual-gating to be translated to clinical applications through the proof-of-concept prototype effort. In addition, the promising results with the SCG signal indicate that other cardiac sensing modalities, such as the blood pressure and photoplethysmogram, can be exploited and potentially be used to enhance the cardiac imaging process.

On a broader scope, this work lays the groundwork for demonstrating the reliability of the cardiac CTA in achieving enhanced patient health outcomes for examining individuals with suspected CVDs. This work also contributes to accelerating CTA in becoming a clinically accepted mainstream diagnostic tool for assessing coronary segments.

The continuing pursuit of better health care and the growing attention to CVDs motivate this work on enhancing techniques to assess cardiac related health issues. The wide use of the prospective cardiac CTA can significantly reduce the radiation dose which is crucial for the health of many individuals. The methods and algorithms developed and discussed in this work could significantly improve the assessment of CVD, and potentially advance the understanding of cardiovascular disease with the development of a framework to achieve better cardiac imaging.

7.2 Limitations and Future Work

One critical assumption of this work is that the interventricular septal (IVS) motion derived from patient-specific echocardiography serves as the baseline for coronary vessel motion. Ultimately, to validate the fusion-based prediction, the quiescence derived from the fusion-based method needs to correlate with the motion of coronary arteries derived from the CTA. However, because of radiation dose, currently it is not possible to obtain the CTA data for a large number of cardiac cycles. On the other hand, it has been shown that the motion of the IVS is a very good marker of coronary arterial motion [36]. Therefore, echocardiography-derived motion serves as an excellent, and ethically acceptable, surrogate marker of coronary vessel motion. Looking ahead, a superior marker closer to coronary vessel motion such as angiography could be explored in future work.

Another limitation is the small sample size in this work. As the subject population enlarges and subject demographics widens, stronger conclusions on the performance of the multimodal framework can be made.

In addition to these limitations, there is a lack of standardization for some issues in the field of cardiac gating. Solving these issues will significantly accelerate related works, and advance the development of a more intelligent imaging system that eases the radiologic technologists (RTs) from additional operations.

1. The decision of whether to use a retrospective or prospective gating technique is currently exclusively decided by the RTs. The decision is made based on the observation of heart rate and heart rate variability. As a rule of thumb, higher heart rate (e.g. greater than 83 bpm) or variability prompts the use of retrospective gating, and lower heart rate and variability prompts the use of prospective gating. However, this is not reliable since abnormal heart rates may be missed by a manual screening for a short period of time. Therefore, it is necessary to come up with a standard to strategically, or even intelligently without human effort, to decide the suitable gating

technique to use. This may include consideration of the individual's physiological condition such as symptoms, height and weight.

2. Data acquisition in systole or diastole for prospective gating is solely heart rate dependent and varies with different ECG-gating functions. Chapter 2.1.1 introduced several different ECG-gating functions that are used by different cardiac imaging machines. To date, there is no universal ECG-gating function that can be used by all, indicating that ECG-based prediction may be inconsistently used.

3. The annotation of the SCG signal is challenging as compared to ECG due to the existence of large morphological variability of SCG among the subjects and its susceptibility to distortions from body motion, respiration and noise artifacts. An accurate and robust approach to identify features of SCG signals is need to formulate a universal annotation template for the SCG.

Future work can investigate the effect of different acceleration sensor locations, e.g. sternum versus apex, to the waveforms of the heart sound associated components in the SCG signal and to the timing of the SCG reference point within the cardiac cycle for quiescence prediction.

Furthermore, future research may evaluate the application of retrospective and prospective gating for cardiac CTA data acquisition, identify the clinical trend of cardiac gating techniques, and investigate potential parameters that may have led to such a clinical trend in order to promote solutions to the existing challenges in cardiac CTA. The significance of this is to provide a historical review of the application of cardiac CTA in diagnosing CVDs, but also to stress the significance of developing a more reliable prospective gating approach to reduce the radiation dose.

Appendices

APPENDIX A

SENSOR CHARACTERISTICS COMPARISON

Table A.1: Comparison of the accelerometers used in the Enhanced and Custom Systems

	Enhanced	Custom
Sensor Type	352A24/NC (PCB PIEZOTRONICS, Depew, NY, USA)	ADXL327 (Analog Devices, Norwood, MA, USA)
Weight	$0.8\,\mathrm{g}$	$5\,\mathrm{g}$
Sensing Element	Ceramic	MEMS (Polysilicon)
Housing Material	Aluminum	MEMS (Polysilicon)
Bandwidth (tuned)	0.4-12 kHz	0-50 Hz
Spectral Noise†	$4\,\mu\mathrm{g}/\sqrt{\mathrm{Hz}}$ $(10-100$ Hz) $15\,\mu\mathrm{g}/\sqrt{\mathrm{Hz}}$ $(1-10$ Hz) $80\,\mu\mathrm{g}/\sqrt{\mathrm{Hz}}$ $(<1$ Hz)	$250\,\mu\mathrm{g}/\sqrt{\mathrm{Hz}}$
Sensitivity	$100\,\mu\mathrm{V}/\mathrm{g}$	$420\,\mu\mathrm{V}/\mathrm{g}$

† g is the earth gravity constant and $g = 9.8\,\mathrm{m}/\mathrm{s}^2$.

APPENDIX B

REVISED ANN FEATURE SET

This section describes the selection of a revised feature set for the real-time fusion-based prediction. Compared with the features reported in Chapter 5, this revised feature set has less number of features, and the extraction of features are less time-consumed. However, the revised feature set demonstrated improved quiescence prediction accuracy based on the results reported in Chapter 6.4.

The selection of features involves two stages. The first stage is to generate an original feature set, from which a more select feature set is obtained in the second stage. The original set of features to be extracted from a frame of data samples are:

1. AR_{ecg}: AR model coefficients of order 7 from the ECG signal. Previous work has demonstrated the effectiveness of the AR(7) model in quantitatively delineating the ECG waveforms [132]. This work empirically found that the first four coefficients that correspond to the $5^{th} - 7^{th}$ data samples enabled achievement of high ANN classification accuracy. Therefore, the last three normalized coefficients ($AR^5_{ecg}(7) - AR^7_{ecg}(7)$) were used as features.

2. $STFT_{scg}$: Short-time Fourier transform (STFT) of the SCG signal. The mean ($STFT^1_{scg}$) and variance ($STFT^2_{scg}$) of the real part of the frequency spectrum were used as features.

3. DWT_{scg}: DWT coefficients from the SCG signal, decomposed down to level 6 using "Coif5" as the mother wavelet[1]. The mean (DWT^1_{scg}) and variance (DWT^2_{scg}) of the coefficients were used as features. The DWT allows for obtaining the temporal

[1]To ensure that the wavelet coefficients are free from boundary effects, a good rule is to set the decomposition level no greater than $\log_2(L)$ for a signal of length L. In this work, the sample size of the processing frame is 97.

information of the signal in addition to the frequency information from the STFT.

In summary, the original feature set consists a total number of 7 single-value features. Among the 7 features, 3 are from the ECG signal and 4 are from the SCG signal. Table B.1 provides a listing of the features and their corresponding numbers.

Table B.1: Original Features

AR_{ecg}	$STFT_{scg}$	DWT_{scg}	Total
3	2	2	7

The selected features embody the capability in capturing the difference between the two categories. A direct visualization of the 5^{th} AR(7) coefficient, variance of the STFT and mean of the DWT are presented by category in Figure B.1. The ranges of features are different for different categories, indicating the capability in classifying the two categories.

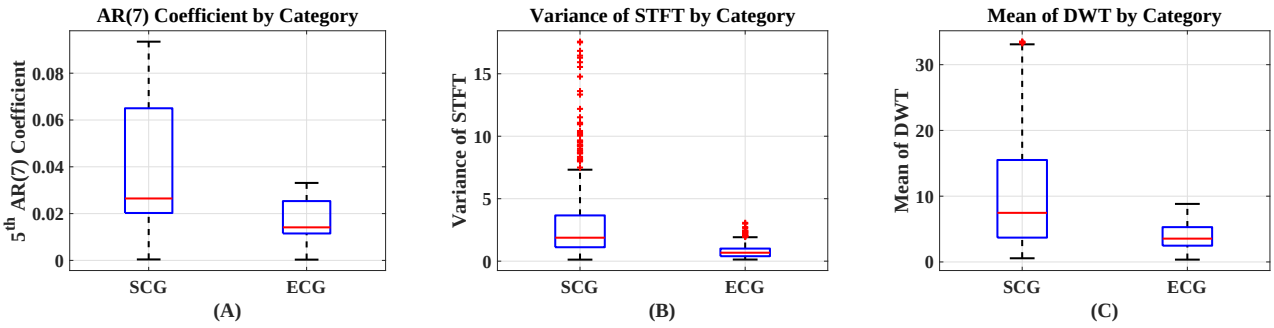

Figure B.1: Features by category. The features presented are (A) $AR^5_{ecg}(7)$, (B) $STFT^2_{scg}$ and (C) DWT^1_{scg}.

Each feature was normalized by subtracting the minimum and then divided by the maximum. In addition, principal component analysis (PCA) was applied where eigenvalues less than 20% of the largest eigenvalue were discarded. The relative importance of the features were than evaluated using the neighborhood component analysis (NCA) [111] with regularization. It was observed from the relative weights in Figure B.2 that three features, $AR^7_{ecg}(7)$, $STFT^1_{scg}$ and DWT^1_{scg}, have very low weights, and thus were discarded for the ANN classification.

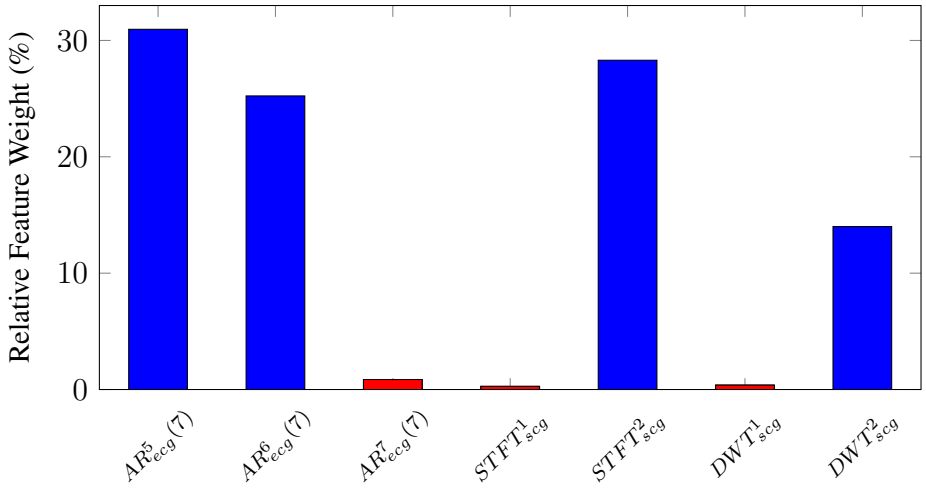

Figure B.2: Relative feature weight evaluated by the NCA. Features in red bars demonstrate less importance in distinguishing the two categories (ECG and SCG), and consequently were discarded.

Therefore, a select feature set extracted from the original feature set was constructed. The select feature set consists of 4 single-value features, 2 of which are from the ECG signal and 2 are from the SCG signal. Table B.2 presents a listing of the select features and their corresponding numbers.

Table B.2: Select Features

AR_{ecg}	$STFT_{scg}$	DWT_{scg}	Total
2	1	1	4

The computational complexity is a concern for the real-time processing. The classic Fourier transform-based spectral analysis is relatively computationally expensive (its computational complexity is $\mathcal{O}(N^2)$ for N samples) and time consuming for near real-time processing. The STFT is an alternative technique to analyze short duration of data with a faster computation. The computational complexity of STFT is $\mathcal{O}(N \log_2 N)$ for N samples.

Compared with the Fourier-based transform, the wavelet transform has the advantage of adaptively alternating the transforming window length in the face of frequency change in a way that the window shortens in time and lengthens in frequency for high frequency signals

to capture the high-frequency component in the transient behavior, vice versa for low-frequency components. Many one dimensional DWT can be accomplished in $\mathcal{O}(N)$. Due to the recursive nature of the AR algorithm, the computational cost of the AR parameter estimation varies, depending on the size of the data samples involved.

With regard to the time consumption, the training of ANN is carried out beforehand using cardiac data from subjects within the same cohort, so the ANN configuration parameters such as the weights of each layer, are pre-defined. In the real-time scenario, prediction with the trained ANN is solely a process of vector multiplication and thresholding. Essentially, the time consumption of extraction features primarily contributes to the total latency of the computerized processing.

To evaluate the time consumption of the AR modelling, STFT, and DWT algorithms, a sequence of 97 data sample underwent each algorithm individually for 1000 times, the average processing time associated with each algorithm is summarized in Figure B.3. The algorithm parameters were chosen in such a way that simulated the near real-time setting. In the spectrogram that uses the STFT over 0-50 Hz frequency range, the segment length to perform windowing was 64 data samples, and the overlapping was 60 data samples. The decomposition level for the DWT was 5, and the mother wavelet was “Coif5”.

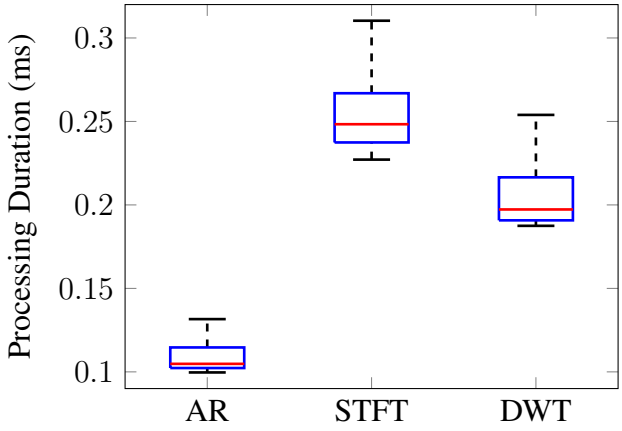

Figure B.3: Average processing duration associated with AR modelling, STFT, and DWT for processing a frame of 97 samples. The red bars in each box indicates the median value.

The average processing durations associated with the primary algorithms for the fusion-

based prediction (AR, STFT and DWT) were all fractions of a millisecond. A more complete report of the computerized duration introduced by each module of the computerized processing is presented in Chapter 6.4.1.

APPENDIX C
HARDWARE SCHEMATIC LAYOUT

As a proof-of-principle, the near real-time implementation was demonstrated with a typical laptop computer. However, to approach a direct interface with imaging equipment, an independent device dedicated to the computerized processing for quiescence prediction is envisioned. The rationales are as follows:

1. Dedicated processing: The independent device is designed for a dedicated purpose, e.g., quiescence prediction, while the general-purpose computer is usually burdened with multiple tasks such as managing running applications and background processes. The additional tasks imposed to the general-purpose computer takes up extra CPU efforts and memory allocation. Therefore, the dedicated device can achieve higher performance for a specific task than a general-purpose computer.

2. Size reduction: The physical size of the dedicated device can be made much smaller, and can be designed to be compatible with the clinical machines such as the working station/computer of a designated CTA scanner.

3. Improvement in prediction accuracy: The selected DSP processor can possibly improve the quiescent prediction accuracy. It is expected that more complicated algorithms may be developed to refine the quiescent prediction, which will likely to require higher floating point precision, faster clock speed and less data overhead.

4. Communication delay reduction: The communication between the hardware and software platforms are currently controlled by the BHAPI whose routines such as data transfer protocols, are encapsulated and cannot be changed easily for some particular requirements of this work. The communication delay can be significantly reduced with a hands-on device.

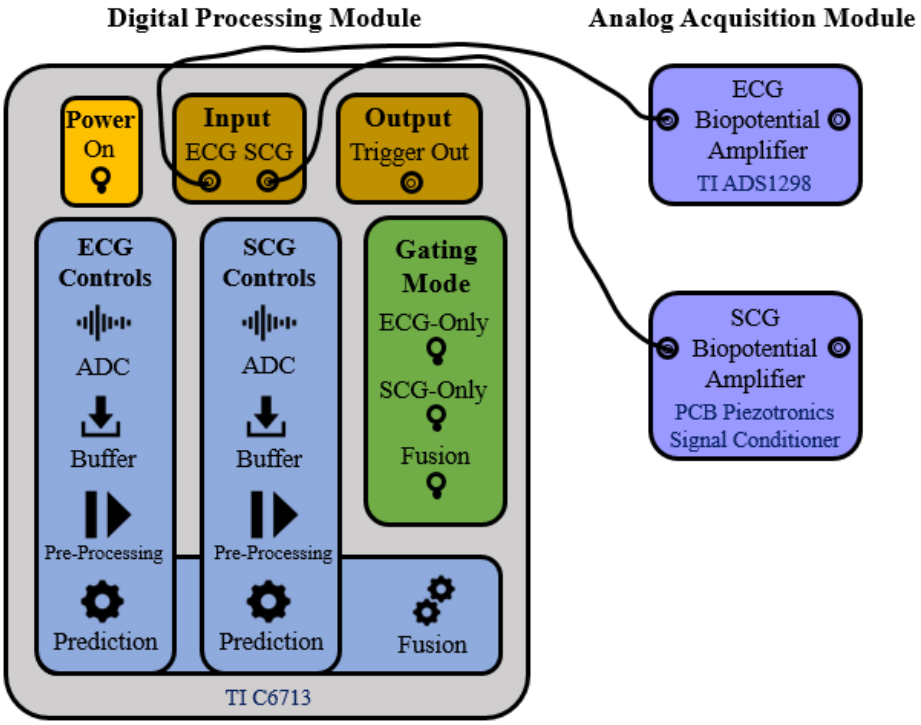

Figure C.1: Schematic layout of an independent device dedicated to the computerized processing for quiescence prediction.

A schematic layout of an independent application-specific device is presented in Figure C.1. The device consists of two modules, one for analog data acquisition, and another for digital processing.

The analog data acquisition module acquires analog cardiac signals and relays amplified analog signals to the digital processing module. A good data acquisition module minimizes the latency in communication and improves prediction accuracy by acquiring signals with high signal-to-noise ratio. The analog processing module for the ECG can be made by using a standard ECG analog front end design [133], or using the off-the-shelf fully integrated TI ADS1298 (TI, Dallas, TX, USA) circuit board [134]. Both of the ECG acquisition options can be developed into wired communication. For the SCG signal, the Piezotronics signal conditioner (PCB Piezotronics Inc., Depew, NY, USA) used in the enhanced data acquisition system can remain be used for the SCG analog module as it effectively amplifies the SCG signal.

The digital processing module can potentially use the floating-point TMS320C6713 (C6713, TI, Dallas, TX, USA) as the DSP processor, in combination with the code composer studio (CCS) as the integrated development environment for developing applications. The selected processor and CCS are designed for dedicated processing, and the DSP chip is adequately small to be re-framed for compatibility. The CCS supports low-level programming language such as C. In addition, the selected DSP processor is a classic model that has been widely applied to various research such as speech and acoustic recognition system [135, 136]. Furthermore, the C6713 is very well suited for numerically intensive algorithms due to the Very-Long Instruction Word (VLIW) architecture. The floating-point feature can improve the prediction precision. Other features of the C6713 include 264 kB of internal memory, eight functional or execution units composed of six arithmetic-logic units (ALUs) and two multiplier units, and a 32-bit address bus to address 4 GB.

This work requires that the DSP processor to be able to achieve analog to digital conversion for the analog input signals and pre-process the buffered samples by filtering out noise and removing the baseline drift. In addition, quiescent predictions requires basic arithmetic operations and DSP operations such as STFT, AR and DWT. Auxiliary components in the digital processing module may include indicators for power status and gating mode status. The output of the digital processing module is a trigger indicating the data acquisition of the cardiac CTA. As a side note, the selected components for constructing the dedicated device are easy to use, flexible, and economical.

REFERENCES

[1] Emelia J Benjamin et al. “Heart disease and stroke statistics-2017 update: a report from the American Heart Association.” In: *Circulation* 135.10 (2017), e146–e603.

[2] Nima Aghili, Edouard Daher, and Carey Kimmelstiel. “Coronary angiography”. In: *Cardiology Procedures*. Springer, 2017, pp. 237–248.

[3] Joseph A Ladapo et al. “Clinical outcomes and cost-effectiveness of coronary computed tomography angiography in the evaluation of patients with chest pain”. In: *Journal of the American College of Cardiology* 54.25 (2009), pp. 2409–2422.

[4] Virginia L Priest et al. “Cost-effectiveness of coronary computed tomography and cardiac stress imaging in the emergency department: a decision analytic model comparing diagnostic strategies for chest pain in patients at low risk of acute coronary syndromes”. In: *JACC: Cardiovascular Imaging* 4.5 (2011), pp. 549–556.

[5] Matthew J Budoff et al. “Assessment of coronary artery disease by cardiac computed tomography: a scientific statement from the American Heart Association Committee on Cardiovascular Imaging and Intervention, Council on Cardiovascular Radiology and Intervention, and Committee on Cardiac Imaging, Council on Clinical Cardiology”. In: *Circulation* 114.16 (2006), pp. 1761–1791.

[6] Songshou Mao et al. “Optimal ECG trigger point in electron-beam CT studies: three methods for minimizing motion artifacts”. In: *Academic radiology* 8.11 (2001), pp. 1107–1115.

[7] Stephan Achenbach et al. “Noninvasive coronary angiography by retrospectively ECG-gated multislice spiral CT”. In: *Circulation* 102.23 (2000), pp. 2823–2828.

[8] Carson A Wick et al. “A system for seismocardiography-based identification of quiescent heart phases: implications for cardiac imaging”. In: *IEEE Transactions on Information Technology in Biomedicine* 16.5 (2012), pp. 869–877.

[9] TA Pearson, GA Mensah, and RW Alexander. “Markers Of Inflammation And Cardiovascular Disease”. In: *Journal of Cardiopulmonary Rehabilitation* 23.3 (2003), pp. 236–237.

[10] *Cardiovascular disease*. visited 2017/06/01. World Health Organization, 2017. eprint: http://www.who.int/mediacentre/factsheets/fs317/en/.

[11] Mark J Ricciardi, Nirat Beohar, and Charles J Davidson. “Cardiac Catheterization and Coronary Angiography”. In: *Essential Cardiology*. Springer, 2005, pp. 197–219.

[12] Morteza Tavakol, Salman Ashraf, and Sorin J Brener. “Risks and complications of coronary angiography: a comprehensive review”. In: *Global journal of health science* 4.1 (2012), p. 65.

[13] Dariush Mozaffarian et al. “Heart disease and stroke statistics2016 update: a report from the American Heart Association”. In: *Circulation* 133.4 (2016), e38–e360.

[14] Benoit Desjardins and Ella A Kazerooni. “ECG-gated cardiac CT”. In: *American Journal of Roentgenology* 182.4 (2004), pp. 993–1010.

[15] *Computed Tomography (CT)*. visited 2018/04/28. U.S. Food & Drug Administration. eprint: https://www.fda.gov/Radiation-EmittingProducts.

[16] Fabian Plank et al. “The diagnostic and prognostic value of coronary CT angiography in asymptomatic high-risk patients: a cohort study”. In: *Open Heart* 1.1 (2014), e000096.

[17] Manesh R. Patel et al. “Low Diagnostic Yield of Elective Coronary Angiography”. In: *New England Journal of Medicine* 362.10 (2010). visited 2017/06/015, pp. 886–895. eprint: http://dx.doi.org/10.1056/NEJMoa0907272.

[18] Zhonghua Sun. “Coronary CT angiography with prospective ECG-triggering: an effective alternative to invasive coronary angiography”. In: *Cardiovascular diagnosis and therapy* 2.1 (2012), pp. 28–37.

[19] Stephan Achenbach et al. “Coronary computed tomography angiography with a consistent dose below 1 mSv using prospectively electrocardiogram-triggered high-pitch spiral acquisition”. In: *European heart journal* 31.3 (2009), pp. 340–346.

[20] Srini Tridandapani, J Brian Fowlkes, and Jonathan M Rubin. “Echocardiography-based selection of quiescent heart phases implications for cardiac imaging”. In: *Journal of ultrasound in medicine* 24.11 (2005), pp. 1519–1526.

[21] Kevin R Johnson et al. “Three-Dimensional, Time-Resolved Motion of the Coronary Arteries”. In: *Journal of Cardiovascular Magnetic Resonance* 6.3 (2004), pp. 663–673.

[22] John M Zanetti and David M Salerno. “Seismocardiography: a technique for recording precordial acceleration”. In: *Computer-Based Medical Systems, 1991. Proceedings of the Fourth Annual IEEE Symposium*. IEEE. 1991, pp. 4–9.

[23] Richard S Crow et al. “Relationship between seismocardiogram and echocardiogram for events in the cardiac cycle”. In: *American journal of noninvasive cardiology* 8.1 (1994), pp. 39–46.

[24] J Neary, DS MacQuarrie, and V Gebhardt. “Relationship Between Seismocardiography and Echocardiography for Measuring Cardiac Cycle Timing Events”. In: *Proceedings of The Physiological Society*. The Physiological Society. 2011.

[25] David Mac Quarrie and Patrick Neary. “Comparison of seismocardiography to echocardiography for measuring cardiac cycle events”. In: *6th Annual University of Regina Graduate Student Research Conference* (2011).

[26] Carson A Wick et al. “Characterization of cardiac quiescence from retrospective cardiac computed tomography using a correlation-based phase-to-phase deviation measure”. In: *Medical physics* 42.2 (2015), pp. 983–993.

[27] Gust H Bardy et al. *Wearable electrocardiography and physiology monitoring ensemble*. US Patent 9,655,537. 2017.

[28] Lars Husmann et al. “Coronary Artery Motion and Cardiac Phases: Dependency on Heart Rate Implications for CT Image Reconstruction”. In: *Radiology* 245.2 (2007), pp. 567–576.

[29] Harald Seifarth et al. “Optimal systolic and diastolic reconstruction windows for coronary CT angiography using dual-source CT”. In: *American Journal of Roentgenology* 189.6 (2007), pp. 1317–1323.

[30] Stephan Achenbach et al. “SCCT expert consensus document on computed tomography imaging before transcatheter aortic valve implantation (TAVI)/transcatheter aortic valve replacement (TAVR)”. In: *Journal of cardiovascular computed tomography* 6.6 (2012), pp. 366–380.

[31] Philip A Araoz et al. “Optimal image reconstruction phase at low and high heart rates in dual-source CT coronary angiography”. In: *The international journal of cardiovascular imaging* 25.8 (2009), pp. 837–845.

[32] Monvadi B Srichai et al. “Dual-source computed tomography angiography image quality in patients with fast heart rates”. In: *Journal of cardiovascular computed tomography* 3.5 (2009), pp. 300–309.

[33] Stephan Achenbach et al. “Contrast-enhanced coronary artery visualization by dual-source computed tomographyinitial experience”. In: *European journal of radiology* 57.3 (2006), pp. 331–335.

[34] Antonios Perperidis et al. “Dynamic Enhancement of B-Mode Cardiac Ultrasound Image Sequences”. In: *Ultrasound in Medicine and Biology* 43.7 (2017), pp. 1533–1548.

[35] CA Wick et al. “Echocardiography as an indication of continuous-time cardiac quiescence”. In: *Physics in Medicine and Biology* 61.14 (2016), p. 5297.

[36] Garry Liu et al. “Ultrasound-guided identification of cardiac imaging windows”. In: *Medical physics* 39.6 (2012), pp. 3009–3018.

[37] Hugo Andrés Mantilla, Felix Ramón Montes, and William F Amaya. “Transesophageal echo diagnosis of perioperative unusual transient left ventricular apical ballooning syndrome”. In: *Annals of cardiac anaesthesia* 19.4 (2016), p. 733.

[38] Jingting Yao et al. “Seismocardiography-based cardiac computed tomography gating using patient-specific template identification and detection”. In: *IEEE Journal of Translational Engineering in Health and Medicine* 5 (2017), pp. 1–14.

[39] David M Salerno and John Zanetti. “Seismocardiography for monitoring changes in left ventricular function during ischemia.” In: *Chest Journal* 100.4 (1991), pp. 991–993.

[40] Richard A Wilson et al. “Diagnostic accuracy of seismocardiography compared with electrocardiography for the anatomic and physiologic diagnosis of coronary artery disease during exercise testing”. In: *The American journal of cardiology* 71.7 (1993), pp. 536–545.

[41] Mikko Paukkunen. “Seismocardiography: Practical implementation and feasibility”. PhD thesis. Aalto University, Oct. 2014.

[42] Mojtaba Jafari Tadi et al. “Accelerometer-based method for extracting respiratory and cardiac gating information for dual gating during nuclear medicine imaging”. In: *Journal of Biomedical Imaging* 2014 (2014), p. 6.

[43] Jafari M Tadi et al. “A novel dual gating approach using joint inertial sensors: implications for cardiac PET imaging”. In: *Physics in Medicine & Biology* 62.20 (2017), p. 8080.

[44] Carson A Wick et al. “Relationship between cardiac quiescent periods derived from seismocardiography and echocardiography”. In: *2015 37th Annual International Conference of the IEEE Engineering in Medicine and Biology Society (EMBC)*. IEEE. 2015, pp. 687–690.

[45] Carson A Wick et al. “Seismocardiography-Based Detection of Cardiac Quiescence”. In: *IEEE Transactions on Biomedical Engineering* 62.8 (2015), pp. 2025–2032.

[46] F Khosrow-Khavar, K Tavakolian, and C Menon. “Moving toward automatic and standalone delineation of seismocardiogram signal”. In: *2015 37th Annual International Conference of the IEEE Engineering in Medicine and Biology Society (EMBC)*. IEEE. 2015, pp. 7163–7166.

[47] Alireza Akhbardeh et al. “Comparative analysis of three different modalities for characterization of the seismocardiogram”. In: *2009 Annual International Conference of the IEEE Engineering in Medicine and Biology Society*. IEEE. 2009, pp. 2899–2903.

[48] Gari D Clifford, F Azuaje, and P McSharry. “ECG statistics, noise, artifacts, and missing data”. In: *Advanced Methods and Tools for ECG Data Analysis* 6 (2006), p. 18.

[49] C Saritha, V Sukanya, and Y Narasimha Murthy. “ECG signal analysis using wavelet transforms”. In: *Bulg. J. Phys* 35.1 (2008), pp. 68–77.

[50] Jie Tang, Jiang Hsieh, and Guang-Hong Chen. “Temporal resolution improvement in cardiac CT using PICCS (TRI-PICCS): Performance studies”. In: *Medical physics* 37.8 (2010), pp. 4377–4388.

[51] Tetsuma Kawaji et al. “Feasibility and diagnostic performance of fractional flow reserve measurement derived from coronary computed tomography angiography in real clinical practice”. In: *The international journal of cardiovascular imaging* 33.2 (2017), pp. 271–281.

[52] Richard Klabunde. *Cardiovascular physiology concepts*. Lippincott Williams & Wilkins, 2011.

[53] Charles L Webber et al. “Nonlinear cardiac dynamics”. In: *Current Issues and Recent Advances in Pacemaker Therapy*. InTech, 2012.

[54] Joel M Felner. “Clinical Methods: The History, Physical, and Laboratory Examinations. 3rd edition.” In: *Chapter 22 The first heart sound* (1990).

[55] Paolo Castiglioni et al. “Cardiac sounds from a wearable device for sternal seismocardiography”. In: *Engineering in Medicine and Biology Society, EMBC, 2011 Annual International Conference of the IEEE*. IEEE. 2011, pp. 4283–4286.

[56] J Granados et al. “Acoustic heart. Interpretation of Phonocardiograms by computer”. In: *Journal of Physics: Conference Series*. Vol. 582. 1. IOP Publishing. 2015, p. 012057.

[57] Mustafa Yamacli, Zumray Dokur, and Tamer Olmez. “Segmentation of S1–S2 sounds in phonocardiogram records using wavelet energies”. In: *Computer and Information Sciences, 2008. ISCIS'08. 23rd International Symposium on*. IEEE. 2008, pp. 1–6.

[58] Li Wang. *Monitoring an interval within the cardiac cycle*. US Patent 9,538,922. 2017.

[59] Mario Merri et al. “Relation between ventricular repolarization duration and cardiac cycle length during 24-hour Holter recordings. Findings in normal patients and patients with long QT syndrome.” In: *Circulation* 85.5 (1992), pp. 1816–1821.

[60] Carl J Wiggers. “Studies on the consecutive phases of the cardiac cycle: I. The duration of the consecutive phases of the cardiac cycle and the criteria for their precise determination”. In: *American Journal of Physiology-Legacy Content* 56.3 (1921), pp. 415–438.

[61] Cherik Bulkes, Gopal B Avinash, and Tinsu Pan. *Method and apparatus of cardiac ct imaging using ECG and mechanical motion signals*. US Patent 7,389,136. 2008.

[62] Gopal B Avinash et al. *Method and system using a non-electrical sensor for gating*. US Patent 7,389,136. 2008.

[63] *Digital Triggers and Gating Systems for MRI: DTU 200/300*. visited 2018/05/10. BIOPAC Systems, Inc. eprint: https://www.biopac.com/product-category/research/mri-magnetic-resonance-imaging/gating-trigger/.

[64] Jonathan M Rubin et al. *Ultrasound gating of cardiac CT scans*. US Patent 7,542,544. 2009.

[65] Kouhyar Tavakolian. “Characterization and analysis of seismocardiogram for estimation of hemodynamic parameters”. PhD thesis. Simon Fraser University, 2010.

[66] Omer T Inan et al. “Ballistocardiography and seismocardiography: A review of recent advances”. In: *IEEE journal of biomedical and health informatics* 19.4 (2015), pp. 1414–1427.

[67] Ahsan H Khandoker, Marimuthu Palaniswami, and Chandan K Karmakar. “Support vector machines for automated recognition of obstructive sleep apnea syndrome from ECG recordings”. In: *IEEE Transactions on Information Technology in Biomedicine* 13.1 (2009), pp. 37–48.

[68] Nitish V Thakor, John G Webster, and Willis J Tompkins. “Estimation of QRS complex power spectra for design of a QRS filter”. In: *IEEE Transactions on biomedical engineering* 11 (1984), pp. 702–706.

[69] Chrisptopher Watford. *Understanding ECG Filtering*. visited 2018/04/03. Mar. 2014. eprint: http://www.ems12lead.com/2014/03/10/understanding-ecg-filtering/.

[70] Puneet Kumar Jain, Anil Kumar Tiwari, and Vijay S Chourasia. “Performance analysis of seismocardiography for heart sound signal recording in noisy scenarios”. In: *Journal of medical engineering & technology* 40.3 (2016), pp. 106–118.

[71] M Di Rienzo et al. “Wearable seismocardiography: Towards a beat-by-beat assessment of cardiac mechanics in ambulant subjects”. In: *Autonomic Neuroscience* 178.1 (2013), pp. 50–59.

[72] Alexandre Laurin, Andrew Blaber, and Kouhyar Tavakolian. “Seismocardiograms return valid heart rate variability indices”. In: *Computing in Cardiology 2013*. IEEE. 2013, pp. 413–416.

[73] Farzad Khosrow-khavar et al. “Automatic Annotation of Seismocardiogram With High-Frequency Precordial Accelerations”. In: *IEEE journal of biomedical and health informatics* 19.4 (2015), pp. 1428–1434.

[74] John Reinhold and Ulf Rudhe. “Relation of the first and second heart sounds to events in the cardiac cycle”. In: *British heart journal* 19.4 (1957), p. 473.

[75] Yaser S Abu-Mostafa, Malik Magdon-Ismail, and Hsuan-Tien Lin. *Learning from data*. Vol. 4. AMLBook Singapore, 2012.

[76] XJ Wang et al. “Dynamic GM (1, 1) model based on cubic spline for electricity consumption prediction in smart grid”. In: *China Communications* 7.4 (2010), pp. 83–88.

[77] S Mandal and GJ Lyons. “On the system identification modelling of offshore dynamic systems”. In: (1994).

[78] Juan Sztajzel et al. “Heart rate variability: a noninvasive electrocardiographic method to measure the autonomic nervous system”. In: *Swiss medical weekly* 134.35-36 (2004), pp. 514–522.

[79] A John Camm et al. “Heart rate variability. Standards of measurement, physiological interpretation, and clinical use”. In: *European heart journal* 17.3 (1996), pp. 354–381.

[80] D Driscoll et al. “Guidelines for evaluation and management of common congenital cardiac problems in infants, children, and adolescents. A statement for healthcare professionals from the Committee on Congenital Cardiac Defects of the Council on Cardiovascular Disease in the Young, American Heart Association.” In: *Circulation* 90.4 (1994), pp. 2180–2188.

[81] Johan von Knorring and Mauri Lepäntalo. “Prediction of perioperative cardiac complications by electrocardiographic monitoring during treadmill excercise testing before peripheral vascular surgery”. In: *Surgery* 99.5 (1986), pp. 610–613.

[82] Yanjun Li, Xiaoying Tang, and Zhi Xu. “An Approach of Heartbeat Segmentation in Seismocardiogram by Matched-Filtering”. In: *Intelligent Human-Machine Systems and Cybernetics (IHMSC), 2015 7th International Conference on*. Vol. 2. IEEE. 2015, pp. 47–51.

[83] Miguel A García-González et al. “A comparison of heartbeat detectors for the seismocardiogram”. In: *Computing in Cardiology Conference (CinC), 2013*. IEEE. 2013, pp. 461–464.

[84] B Yegnanarayana. *Artificial neural networks*. PHI Learning Pvt. Ltd., 2009.

[85] Tom M Mitchell. “Artificial neural networks”. In: *Machine learning* 45 (1997), pp. 81–127.

[86] James A Anderson. *An introduction to neural networks*. MIT press, 1995.

[87] Tony Plate et al. “A comparison between neural networks and other statistical techniques for modeling the relationship between tobacco and alcohol and cancer”. In: *Advances in Neural Information Processing Systems* (1997), pp. 967–973.

[88] Donald B Malkoff. “A Neural Network for Real-Time Signal Processing.” In: *NIPS*. 1989, pp. 248–255.

[89] Rahime Ceylan, Yüksel Özbay, and Bekir Karlik. “A novel approach for classification of ECG arrhythmias: Type-2 fuzzy clustering neural network”. In: *Expert Systems with Applications* 36.3 (2009), pp. 6721–6726.

[90] Keya Pandia, Omer T Inan, and Gregory TA Kovacs. “A frequency domain analysis of respiratory variations in the seismocardiogram signal”. In: *Engineering in Medicine and Biology Society (EMBC), 2013 35th Annual International Conference of the IEEE*. IEEE. 2013, pp. 6881–6884.

[91] Sagar S Nikam. “A comparative study of classification techniques in data mining algorithms”. In: *Orient J Comput Sci Technol* 8.1 (2015), pp. 13–19.

[92] Chhatrapal Singh and Jaspinder Singh. "Biomedical Signal Processing, Artificial Neural Network: A Review". In: *Indian Journal of Science and Technology* 9.47 (2016).

[93] Shadi Mahdiani. "An automated approach: from physiological signals classification to signal processing and analysis". MA thesis. 2017.

[94] George E Billman. "Heart rate variability–a historical perspective". In: *Frontiers in physiology* 2 (2011), p. 86.

[95] Samir Saba et al. "Use of correlation waveform analysis in discrimination between anterograde and retrograde atrial electrograms during ventricular tachycardia". In: *Journal of Cardiovascular Electrophysiology* 12.2 (2001), pp. 145–149.

[96] Keya Pandia et al. "Extracting respiratory information from seismocardiogram signals acquired on the chest using a miniature accelerometer". In: *Physiological Measurement* 33.10 (2012), p. 1643.

[97] Saeid Sanei, Mansoureh Ghodsi, and Hossein Hassani. "An adaptive singular spectrum analysis approach to murmur detection from heart sounds". In: *Medical Engineering & Physics* 33.3 (2011), pp. 362–367.

[98] Zümray Dokur and Tamer Ölmez. "ECG beat classification by a novel hybrid neural network". In: *Computer Methods and Programs in Biomedicine* 66.2 (2001), pp. 167–181.

[99] Michael A Nielsen. *Neural networks and deep learning*. Determination Press, 2015.

[100] Joel Grus. *Data Science from Scratch: First Principles with Python*. O'Reilly Media, Inc., 2015.

[101] RPW Duin et al. "A matlab toolbox for pattern recognition". In: *PRTools Version* 3 (2000), pp. 109–111.

[102] Howard B Demuth et al. *Neural network design*. Martin Hagan, 2014.

[103] John A. Camm et al. "Heart rate variability: standards of measurement, physiological interpretation, and clinical use". In: *Circulation* 93 (1996), pp. 1043–1065.

[104] Jiapu Pan and Willis J Tompkins. "A real-time QRS detection algorithm". In: *IEEE transactions on biomedical engineering* 3 (1985), pp. 230–236.

[105] Gregory F Michaud et al. "Correlation waveform analysis to discriminate monomorphic ventricular tachycardia from sinus rhythm using stored electrograms from im-

plantable defibrillators". In: *Pacing and Clinical Electrophysiology* 22.8 (1999), pp. 1146–1151.

[106] PD Khandait, NG Bawane, and SS Limaye. "Features Extraction of ECG Signal for detection of cardiac arrhythmias". In: *International Journal of Computer Applications* 2.1 (2012), pp. 520–525.

[107] W Xu et al. "Wavelet transform analysis of the seismocardiogram". In: *Proceedings of the IEEE-SP International Symposium on Time-Frequency and Time-Scale Analysis*. IEEE. 1996, pp. 481–484.

[108] F Roche et al. "Predicting sleep apnoea syndrome from heart period: a time-frequency wavelet analysis". In: *European Respiratory Journal* 22.6 (2003), pp. 937–942.

[109] Paolo Castiglioni et al. "Wearable seismocardiography". In: *Engineering in Medicine and Biology Society, 2007. EMBS 2007. 29th Annual International Conference of the IEEE*. IEEE. 2007, pp. 3954–3957.

[110] P Bifulco et al. "Monitoring of respiration, seismocardiogram and heart sounds by a PVDF piezo film sensor". In: *20th IMEKO TC4 International Symposium and 18th International Workshop on ADC Modelling and Testing Research on Electric and Electronic Measurement for the Economic Upturn Benevento*. Vol. 11. 2014, p. 12.

[111] Jacob Goldberger et al. "Neighbourhood components analysis". In: *Advances in neural information processing systems*. 2005, pp. 513–520.

[112] Wei Yang, Kuanquan Wang, and Wangmeng Zuo. "Neighborhood Component Feature Selection for High-Dimensional Data." In: *JCP* 7.1 (2012), pp. 161–168.

[113] Abdul Qadir Qadir Javaid. "Multi-sensor signal processing methods for home monitoring of cardiovascular and respiratory diseases". PhD thesis. Georgia Institute of Technology, 2016.

[114] Hazar Ashouri. "ROBUST ESTIMATION OF SYSTOLIC TIME INTERVALS USING BALLISTOCARDIOGRAM AND SEISMOCARDIOGRAM SIGNALS". PhD thesis. Georgia Institute of Technology, 2017.

[115] Robi Polikar. *Pattern Recognition*. Wiley Encyclopedia of Biomedical Engineering, 2006.

[116] *Choose neural network input-output processing functions - matlab & simulink*. visited 2017/06/01. 2017. eprint: https://www.mathworks.com/help/nnet/ug/choose-neural-network-input-output-processing-functions.html.

[117] Chi Liu et al. “Quiescent period respiratory gating for PET/CT”. In: *Medical physics* 37.9 (2010), pp. 5037–5043.

[118] *BIOPAC Research Catalog*. visited 2018/04/28. BIOPAC Systems. eprint: https://www.biopac.com/wp-content/uploads/research_catalog.pdf.

[119] *BIOPAC Developer Suites: Tools for Scripting, Network Data Transfer, Hardware & Software APIs*. visited 2018/04/28. BIOPAC Systems. eprint: https://www.biopac.com/wp-content/uploads/Developers-Kit-Product-Sheet.pdf.

[120] Thomas Flohr. “Back to the Future: 10 Years of Dual Source CT”. In: *Simens Global* ().

[121] James P Earls et al. “Prospectively gated transverse coronary CT angiography versus retrospectively gated helical technique: improved image quality and reduced radiation dose”. In: *Radiology* 246.3 (2008), pp. 742–753.

[122] Moritz Wyler von Ballmoos et al. “Meta-analysis: diagnostic performance of low-radiation-dose coronary computed tomography angiography”. In: *Annals of internal medicine* 154.6 (2011), pp. 413–420.

[123] Hideki John Reekie. “Realtime Signal Processing–Dataflow, Visual, and Functional Programming”. PhD thesis. University of Technology at Sydney, Aug. 1998.

[124] Shoichi Ehara et al. “Comprehensive evaluation of the apex beat using 64-slice computed tomography: Impact of left ventricular mass and distance to chest wall”. In: *Journal of cardiology* 55.2 (2010), pp. 256–265.

[125] K Ormstad et al. “Difference between in vivo and postmortem distances between anterior chest and heart surface. A combined autopsy and in vivo computerized tomography study.” In: *The American journal of forensic medicine and pathology* 5.1 (1984), pp. 31–35.

[126] *Application Notes: MP100 and MP160/150 System Data Sampling Reference*. visited 2018/04/28. BIOPAC Systems. eprint: https://www.biopac.com/wp-content/uploads/app195.pdf.

[127] Aaron So et al. “Prospectively ECG-triggered rapid kV-switching dual-energy CT for quantitative imaging of myocardial perfusion”. In: *JACC: Cardiovascular Imaging* 5.8 (2012), pp. 829–836.

[128] Justin Mark Raudabaugh. “Effective Dose Estimation in Fast-kV Switch Dual Energy Computed Tomography”. PhD thesis. Duke University, 2016.

[129] Aaron So and Ting-Yim Lee. “Rapid kV switching dual-energy CT imaging”. In: *Dual-Energy CT in Cardiovascular Imaging*. Springer, 2015, pp. 45–60.

[130] Jonathon Leipsic. *Acquisition and Reconstruction Techniques for Coronary CT Angiography*. visited 2018/07/05. Siemens Healthineers. eprint: https://www.heartflow.com/wp-content/uploads/2017/02/CCM-100-115-ASiemensCardiacCCTAProtocol.pdf.

[131] Ernst L Leiss. *Parallel and vector computing: a practical introduction*. McGraw-Hill, Inc., 1995.

[132] Qibin Zhao and Liqing Zhang. “ECG feature extraction and classification using wavelet transform and support vector machines”. In: *Neural Networks and Brain, 2005. ICNN&B'05. International Conference on*. Vol. 2. IEEE. 2005, pp. 1089–1092.

[133] *ECG and PIC Demo*. visited 2018/06/5. 100RandomTasks. eprint: http://www.100randomtasks.com/ecg-and-pic-demo.

[134] *ADS129x Low-Power, 8-Channel, 24-Bit Analog Front-End for Biopotential Measurements*. visited 2018/06/5. TI. eprint: http://www.ti.com/lit/ds/symlink/ads1294.pdf.

[135] Rulph Chassaing. *Digital Signal Processing and Applications with the C6713 and C6416 DSK*. Vol. 16. John Wiley & Sons, 2004.

[136] Amira Boulmaiz et al. “Design and implementation of a robust acoustic recognition system for waterbird species using TMS320C6713 DSK”. In: *International Journal of Ambient Computing and Intelligence (IJACI)* 8.1 (2017), pp. 98–118.